THE UNIVERSITY *of* EDINBURGH

Probing the Phase Diagram of the Ferromagnetic Superconductor UGe_2 Using High Pressure Ultrasonic Techniques

Michal Wawrzyniec Kepa

A thesis submitted in fulfilment of the requirements
for the degree of Doctor of Philosophy
to the
University of Edinburgh
August 2015

Abstract

The main goal of the project was to develop new experimental techniques to further investigate the phase diagram of the ferromagnetic superconductor UGe_2 at high pressures. Of particular interest is the metamagnetic transition (FM1-FM2) which is thought to play the key role in the unconventional superconductivity in UGe_2. The project attempted to detect experimentally the critical ferromagnetic fluctuations associated with the FM1-FM2 transition.

The development of the experimental equipment constitutes a substantial part of the project and includes: (1) a 2-axis Rotation Stage for High Pressures, (2) an Ultrasonic Sapphire Anvil Cell and (3) a High Pressure Pulse Echo Setup. (1) allows transport measurement on single crystal samples with simultaneous two-axis rotation at temperatures down to 2 K, magnetic fields up to 9 T and pressures up to 5 GPa to be made. (2) employs Resonant Ultrasound Spectroscopy on a sample in the anvil type cell with an optical access at cryogenic temperatures. (3) uses the Pulse Echo Technique inside a cylinder type cell allowing for ultrasonic measurements on samples with a well-defined orientation. The design, technical challenges and tests results are presented and discussed.

The existing techniques, used in the project, included Inelastic Neutron Scattering. A single crystal of UGe_2 was studied at 12 kbar with a large volume two-layered piston-cylinder cell. No critical fluctuations were detected at T_x associated with the FM1-FM2 transition. Instead, a small inelastic signal below this transition temperature was observed at the threshold of the instrument sensitivity. The fluctuations at T_C associated with the paramagnetic-to-ferromagnetic transition (PM-FM) were detected and the energy scale of these fluctuations was found to have decreased, as compared to the ambient pressure case, in proportion to the resistivity – a result supporting recent theory.

The elastic constant c_{11} of a single crystal of UGe_2 was measured as a function of temperature using (3) at ambient pressure as well as pressures up to 11 kbar. The elastic constant exhibits clear features associated with the two transitions, PM-FM and FM1-FM2. The temperature dependence of the elastic constant at ambient pressure was modelled with two main contributions (Schottky–like and Wiess–like) to the magnetic heat capacity coming from the two energy scales, T_x and T_C, as well as two corresponding Grüneisen parameters, Ω_x and Ω_C. The values of Grüneisen parameters obtained from the data fitting were in good agreement with the values determined from the slope of the phase transition lines on the phase diagram. The temperature dependence of the elastic constant at high pressures was modelled according to the two-component system with coupled moments. The behaviour of the fitting parameters (including the Ω_x and Ω_T) was consistent with the phase diagram of UGe_2 and captured important features of c_{11} temperature evolution.

The way forward would be to continue the measurements of c_{11} at higher pressures but also to repeat the measurements at different ultrasonic frequencies in order to obtain the temperature dependence of the ultrasonic attenuation which will provide more insight on the FM1-FM2 transition.

Declaration

Except where otherwise stated, the research undertaken in this thesis was the unaided work of the author. Where the work was done in collaboration with others, a significant contribution was made by the author.

Michal Wawrzyniec Kepa
August 2015

Acknowledgements

I would like to thank my supervisors Andrew Huxley and Konstantin Kamenev for their support and guidance during the course of the project. I would like to express my gratitude to Dmitry Sokolov and Martin Boehm for their help with the inelastic neutron scattering experiments on UGe_2. I am also grateful for help and support from the workshop members, especially Ronnie Proc and Andrew Downie – without them the instrumentation development part of the project would not be possible. I would like to thank Chris Ridley for providing the piston cylinder cell for the ultrasonic measurements and his useful comments on high pressure cells and technical aspects of the instrumentation design.

I am also extremely grateful for support and source of motivation from Julian Schmehr, William Whitley, Maciej Koprowski, Rachel Husband, Chris O'Neill, Gino Abdul-Jabbar, Angel Arevalo-Lopez and Duncan McCann.

I would like to thank my parents, Adam and Agnieszka and my sister, Alicja. My gratitude should also go to my friends Michal, Marcin and Marcin for their continual encouragement. Finally, I am grateful to Zuzanna for her kind, loving and patient support.

Then I looked on all the works that my hands had wrought, and on the labour that I had laboured to do: and, behold, all was vanity and vexation of spirit, and there was no profit under the sun.

— Ecclesiastes 2:11

Contents

List of Figures

List of Tables

Chapter 1

Introduction

1.1 Superconductivity – Historical Background

Superconductivity spans more than a century of active research but still remains at the heart of condensed matter physics. Since its discovery, superconductivity evolved into distinct research fields but it is still not a fully understood phenomenon. This work focuses on the heavy fermion material uranium digermanide, UGe_2, which is the first known ferromagnetic superconductor [1].

Superconductivity was discovered by Heike Onnes and Gilles Holst in mercury in 1911 [2]. It is demonstrated prototypically by complete loss of electrical resistance in a material but also by the Meissner effect where a material shows perfect diamagnetism. At the beginning of the 20^{th} century there were three predictions of the behaviour of electrical resistance of metals at low temperature. Firstly, Lord Kelvin suggested that the electrical resistance of any material should diverge at sufficiently low temperatures [3, 4]. Secondly, Paul Drude proposed that electrical resistance saturates at some finite value at zero temperature [3, 4]. Finally, the third supposition was that the resistance should monotonically decrease with temperature to zero [3, 4]. In order to verify any of these statements, pure samples and advances in gas liquefaction were necessary. This was exactly realised in the laboratory of Heike Onnes where a high quality multilayer dewar cryostat was used (this is also where the first liquefaction of helium took place) and where the distillation of liquid mercury was excelled [5]. It was soon realised that application of even moderate external magnetic fields can destroy superconductivity in simple elements which belong to the first group

of superconductors − now known as type-I superconductors.

In the mid of the 1930s, Lev Shubnikov discovered superconductivity in metallic alloys [5]. These materials belong to type-II superconductors in which much higher magnetic fields are required to destroy superconductivity. By the end of the 1960s, the critical transition temperature was pushed up and in 1962 the first commercial superconducting wire was developed. That time witnessed another landmark in the field − the prediction of the Josephson effect, followed by the development of the Josephson junction which is essential to the superconducting quantum interference device (SQUID). In the 1970s, the field of superconductivity was well developed and seemed to be near completion − a comment by Bernd Matthias described the situation [5]:

> "In many discussions, I have tried to point out that the present theoretical attempts to raise the superconducting transition temperature are the opium in the real world of superconductivity where the highest T_C is, at present and best, 21 K. Unless we accept this face and submit to a dose of reality, honest and not so honest speculations will persist until all that is left in this field will be these scientific opium addicts dreaming and reading one another's absurdities in a blue haze."

However, in 1986, Georg Bednorz and Karl Alexander Müller discovered superconductivity in a Ba-La-Cu-O system with a 50% higher superconducting transition temperature of 35 K [6]. This discovery opened a field of high-temperature superconductivity and also boosted the search for unconventional superconductors. The record transition temperature is 138 K and was achieved in the compound $HgBa_2Ca_2Cu_3O_{8+d}$ at ambient pressure and 164 K under a pressure of 30 GPa [7].

As for the theory of superconductivity, it was lagging behind the experimental developments and discoveries. It was simply due to the fact that many body quantum mechanics was developed years after the first fundamental discoveries were made. The early, and failed, attempts to explain superconductivity were incisively commented by Albert Einstein in 1922 [8]:

> "With our far-reaching ignorance of the quantum mechanics of composite systems we are very far from being able to compose a theory out of these vague ideas."

The first important theoretical breakthrough was due to Fritz and Heinz London, who in the 1930s formulated two equations describing how superconductors interact with electromagnetic fields and predicted a characteristic distance over which an external magnetic field penetrates a superconducting material, now known as the London penetration depth.

However, the most important insight was the recognition due to the London theory that superconductivity must originate from quantum effects as John Bardeen noted [9]:

> "It was Fritz London who first recognized that superconductivity and superfluidity result from manifestations of quantum phenomena on the scale of large objects."

In the 1950s, Lev Landau and Vitaly Ginzburg proposed their theory of superconductivity [10] which was based on the Landau theory of phase transitions. The Ginzburg-Landau theory is essentially a mean-field theory describing a thermodynamic state. It expresses the free energy of a superconductor in terms of the complex order parameter ψ. The value of $|\psi|^2$ can be identified as the fraction of electrons in the superconducting state. As for the London theory, it also predicted the penetration depth, but additionally it yielded the coherence length which is the distance from the surface of the superconductor over which the order parameter returns almost to its full bulk value. Seven years after the Ginzburg-Landau theory, a full microscopic theory was presented by John Bardeen, Leon Cooper and John Schrieffer [11]. The BCS theory explained the pairing mechanism between electrons and also many experimentally observed properties such as the isotope effect or the rise in heat capacity near the superconducting critical temperature.

The BCS theory is applicable to the conventional superconductors but does not explain unconventional superconductivity. Unconventional superconductivity was actually found in a heavy fermion material in 1979 – before the discovery by Georg Bednorz and Karl Alexander Müller. That discovery was due to Frank Steglich who observed superconductivity in $CeCu_2Si_2$ below 0.6K [12]. Findings by Steglich can also can be considered as the roots of the work presented here since it later led to the discovery of UGe_2 in 2000. A more complete and detailed summary of the heavy fermions and UGe_2 is presented in the next sections.

1.2 Heavy fermion materials and Unconventional Superconductivity

The heavy fermions are among the most intriguing superconducting materials. The discovery of the prototypical heavy fermion superconductor was due to Frank Steglich who observed superconductivity in $CeCu_2Si_2$ below 0.6K [13]. They contain rare earths or actinides resulting in their complex crystallographic structures and also in physical properties being dominated by $4f$ or $5f$ electron orbitals. The term heavy fermion originates from the itinerant electrons effective mass being orders of magnitude greater than the free electron mass. There are various reasons why the heavy fermions are interesting.

Firstly, they belong to a group of unconventional superconductors and their behaviour cannot be explained within the BCS theory. The BCS theory describes only the spin singlet pairing (total spin s=0) and rests on the electron-phonon coupling. Conventional superconductivity can be defined through the symmetry of the gap as [7]

$$\Delta_{\hat{R}\mathbf{k}} = \Delta_{\mathbf{k}} \tag{1.1}$$

where $\hat{R}$ is any symmetry operation in the point group [7]. Furthermore, for the Fermi surfaces of all non-magnetic metals have inversion symmetry [7], hence

$$\varepsilon_{\mathbf{k}} = \varepsilon_{-\mathbf{k}} \tag{1.2}$$

Conventional superconductors also respect this symmetry [7], therefore

$$\Delta_{\mathbf{k}} = \Delta_{-\mathbf{k}} \tag{1.3}$$

Such a description is insufficient in the context of heavy fermions. For example, UPt_3 exhibits multiple superconducting phases and is considered to be a spin triplet superconductor (total spin s=1) [14]. For spin triplet superconductors, one has $\mathbf{d}(\mathbf{k}) = -\mathbf{d}(-\mathbf{k})$, therefore they are considered to be unconventional.

Secondly, the competition between the magnetic order and the Kondo effect in the heavy fermions results in their complex physics but also makes them very sensitive to tuning either by pressure or chemical doping.

Thirdly, quantum criticality was perspicuously demonstrated in heavy fermion metals [15]. A quantum critical point is defined as the zero temperature limit of a

second order phase transition. The quantum critical state exhibits collective low-energy excitations resulting in a highly correlated and strongly interacting system. The general description of quantum critical points and quantum phase transition follows the Landau phase transition theory. Two phases are distinguished from one another by an order parameter which describes the symmetry breaking upon the transition. The second order phase transitions are characterised by the correlation length which is a measure of length over which the fluctuation of the order parameter are correlated. The main difference between the classical description and the quantum one is that in the case of the quantum phase transition the fluctuations represent zero point motion (which happens in real time) whereas in a thermal transition the fluctuations come from a statistical sampling of different states given by the Bolzmann distribution (which itself can be considered as propagation in imaginary time). The correlation time scales with the correlation length yielding a dynamic exponent [16]. Critical exponents are part of a wider description of a phase transition and they constitute different scaling laws but also universality meaning that they do not depend on the details of a physical system but only on the dimensionality of that system and the range of interaction.

On a macroscopic scale in heavy fermions, the carrier mass enhancement is caused by the interaction between conduction and localised electrons, known as the Kondo interaction. The term was originally used to describe scattering of conduction electrons with a single localised magnetic impurity [16]. At high temperatures (at and below room temperature), strongly correlated f electrons are localised and the on-site Coulomb repulsion is much stronger than their kinetic energy. The localised spins of these electrons then make up the so-called Kondo lattice. Apart from the Kondo effect, there is also the Ruderman-Kittel-Kasuya-Yoshida (RKKY) interaction between the localised spins which could be a direct interaction of spins or indirect through the polarisation of conduction electrons [16].

The Kondo temperature [17] is defined as:

$$k_B T_K \propto \exp\left(-\frac{1}{n(E_f)|J|}\right), \tag{1.4}$$

where k_B is Boltzmann constant, $n(E_f)$ is the density of states at the Fermi level and J is the effective exchange parameter. Whereas, the RKKY temperature

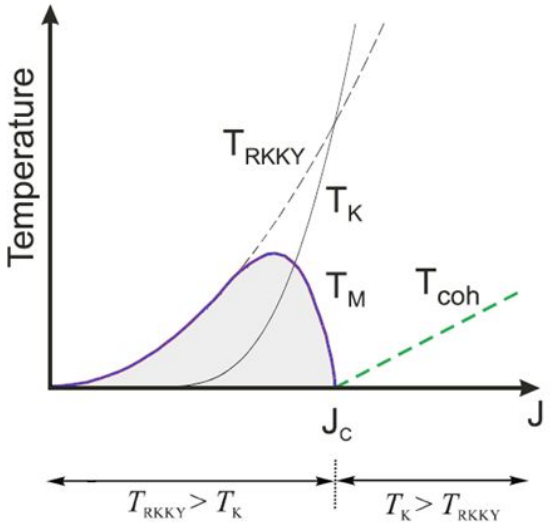

Figure 1.1: Doniach phase diagram. The T_{RKKY}, T_K, T_M are T_{coh} the characteristic temperatures for RKKY interaction, Kondo interaction, magnetic ordering and coherence temperatures respectively. Adopted after [18].

[18] is defined as:

$$k_B T_{RKKY} \propto n(E_f) J^2. \tag{1.5}$$

Within a simple one−dimensional model, the overall effects of these interactions can be summarised on the Doniach phase diagram, Fig. 1.1 [19]. The Kondo effect screens localised spins whereas the RKKY interaction favours long range magnetic order. On the Doniach diagram, the long-range order is observed below the magnetic ordering temperature T_M. In compounds with low J, $T_{RKKY} > T_K$ the system orders magnetically. As J increases, the Kondo effect strengthens and the system becomes less and less magnetically ordered. At the critical value of J the system undergoes a quantum phase transition. Above that value of J, the RKKY interaction dominates and $T_K > T_{RKKY}$ resulting in a nonmagnetic ground state. Finally, the Doniach diagram includes the coherence temperature T_{coh} below which the system displays the Fermi Liquid behaviour demonstrated by a leading T^2 in the electrical resistivity and T-linear term in the electronic heat capacity.

A schematic phase diagram containing a quantum critical point is presented in Fig. 1.2 [20]. The properties of the system are changed via tuning parameter r which can be pressure, chemical doping or magnetic field. As explained above,

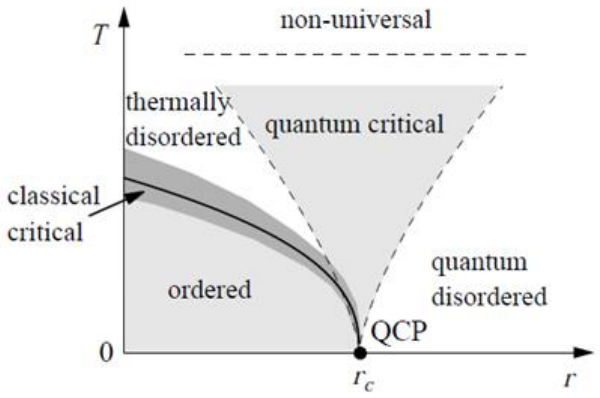

Figure 1.2: Schematic diagrams containing a quantum critical point QCP. The description of the diagram is presented within the text. Adopted after [19].

the quantum critical point positioned at $r = r_c$ is the end point of the classical transition from thermally disordered state (such as paramagnetism) into ordered states (such as ferromagnetism or anitferromagnetism). Above r_c, there is a quantum critical region where the system displays non-Fermi liquid behaviour such as non-quadratic resistivity at low temperatures.

Finally, the quantum critical point is often surrounded by a more stable phase such as superconductivity. This is due to the divergence of the electron effective mass leading to highly degenerate state formation which is very likely to turn into alternative stable states [16].

1.3 A Review of UGe_2 and Open Questions

This section is a review of uranium digermanide and concludes with some open questions regarding its high pressure phase diagram.

1.3.1 A Review of UGe_2

The first work describing properties of uranium digermanide was published in 1960 [21]. It suggested the orthorhombic distorted $ThSi_2$ crystal structure, metallic behaviour and reported the Curie temperature of $T_C = 52\,\mathrm{K}$. The work

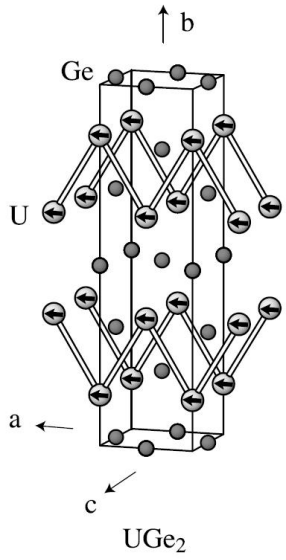

Figure 1.3: Unit cell of UGe_2. The cell belongs to *Cmmm* space group. Adopted after [23].

concluded that the ferromagnetism in UGe_2 might originate in the interaction between the local spin and the conduction electrons as suggested by the comparison between the magnetic moment curves and the electrical resistivity curves. The samples used in the studies were prepared by arc melting.

The more detailed works on structure appeared later [22, 23]. The presented data confirmed the Curie temperature of 52 K and also that UGe_2 has the orthorhombic unit cell (a single crystal X-ray measurement). However, it showed that the unit cell belongs to the *Cmmm* space group and not *Cmmn* as previously reported [22]. The neutron powder data showed also that the uranium magnetic moments are parallel to a-axis of the crystal [22]. The unit cell of UGe_2 is presented in Fig. 1.3 and was adopted from [24].

Further work revealed anomalies observed in the thermal expansion coefficient, thermoelectric power and in the Hall coefficient. It was shown that UGe_2 exhibits strong anisotropy in its magnetic and electrical properties [25, 26]. Early studies of the Fermi surface topology revealed the main Fermi surfaces are almost cylindrical along b-axis with the corresponding cyclotron masses of 15–20m_0. The bandstructure calculation, adopting $5f$ electron model, yielded the quasi-2D sheet nature of the Fermi surface with the majority spin character [27]. In fact, it is now known that the $5f$ electrons, itinerant but strongly correlated in nature, are responsible for most of the magnetism in UGe_2 and its electronic

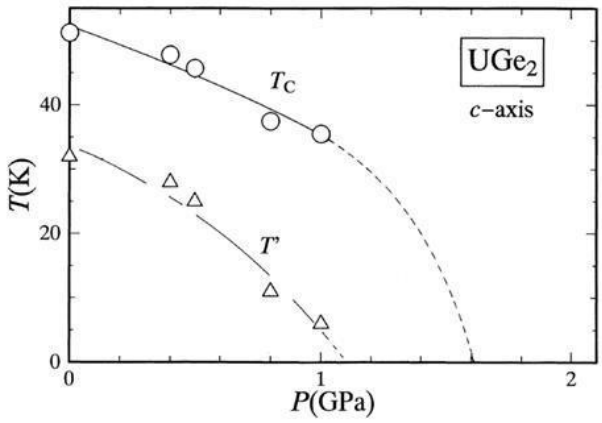

Figure 1.4: Early phase diagram of UGe_2. The diagram indicates two characteristic temperatures, T_C the Curie temperature and T' later identified as associated with a metamagnetic transition. Adopted from [31].

properties [28, 29]. The remaining contribution (up to 10%) to the magnetic moment might be not due to $5f$ but other conduction electrons as suggested by the MuSR data [30]. The $5f$ electron contribution is of anisotropic Ising type whereas, the other conduction electron part is of Heisenberg type [28–30].

The first work under pressure on UGe_2 was published 1993 and reported the electrical resistivity measured under high pressure up to 8 GPa [31]. A later publication elucidated the effect of pressure application on the magnetism in UGe_2 [32]. It showed that the Curie temperature is fully suppressed at high pressure. In addition, the work revealed that the temperature T', associated with the previously observed anomaly [24, 25], is also suppressed by pressure yielding the phase diagram shown in Fig. 1.4 [32].

A more complete and up to date p-T phase diagram is shown on Fig. 1.5 after [33]. As noted, as pressure increases the Curie temperature decreases. The ferromagnetic-paramagnetic (FM-PM) transition at low pressure is second order in nature, then at the tricritical end point (TCP), $p_{TCP} = 14.1$ kbar, it changes to first order [33]. Within the ferromagnetic region, there are two distinct ferromagnetic phases, the high temperature high pressure FM1 phase and the low temperature low pressure FM2 phase. The phases differ in terms of their magnetic moment, $M_0 = 0.9\ \mu_B$ in the FM1 phase and $M_0 = 1.4\ \mu_B$ in FM2 respectively (both values quoted per uranium atom). The FM1-FM2 transition is first order in nature. It is associated with metamagnetism and is only seen at higher pressures.

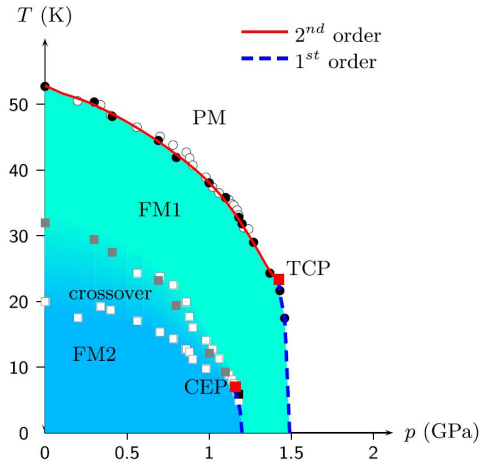

Figure 1.5: p-T phase diagram of UGe_2. Open symbols represent data obtained from thermal expansion and full symbols data from resistivity. CEP and TCP are the critical end point and tricritical end point respectively. Adopted after [32].

Below the critical end point (CEP) of $p_{CEP} = 12.5$ kbar, instead of the transition temperature T_x, there is a broad cross over with no transition line indicating no symmetry breaking. The FM1-FM2 transition is also demonstrated by a large increase in the electronic specific heat but only a small increase in the ratio of the orbital to spin moment [34]. A complete microscopic theory of the FM1-FM2, which could be the key to understanding unconventional superconductivity in UGe_2, still remains an open task. More detailed description of the transition and possible scenarios are discussed in the next section.

The phase diagram exhibits the so called wing-structure if an external magnetic field is applied, Fig. 1.6. The first order planes (PM-FM1) on the p-T-H phase diagram emerge from the tricritical point at $p_{TCP} = 14.1$ kbar and $T_{TCP} = 24$ K. The transition was observed in the Hall and electrical resistivity up to $p = 34.1$ kbar and for magnetic field up to $H = 16$ T [35]. From the data extrapolation, the position of the quantum critical end point (QCEP) was identified to be $p_{QCEP} = 35$-36 kbar and $H_{QCEP} = 17$-19 T [35]. So far, the wing structure associated with the critical end point on the FM1-FM2 transition was not discovered.

Superconductivity in UGe_2 was discovered in 2000 [1]. The superconducting phase lies entirely within the ferromagnetic phase. There are two main features of the phase diagram that show the ferromagnetism and superconductivity to be cooperative phenomena in UGe_2 as shown in Fig. 1.7 [36]. Firstly,

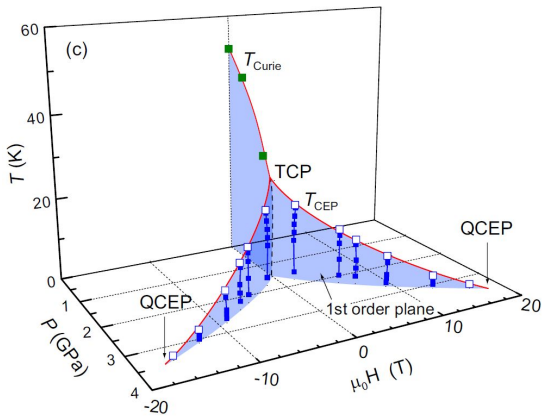

Figure 1.6: p-T-H phase diagram of UGe_2. Data points obtained from Hall resistivity and electrical resistivity measurements. $QCEP$ and TCP are quantum critical end point and tricritical end point respectively. Adopted after [34].

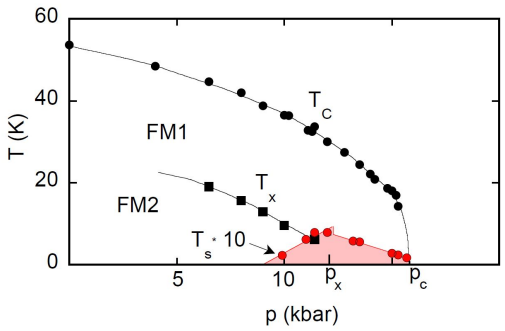

Figure 1.7: Phase diagram of UGe_2 displaying superconducting region. The T_S is the onset temperature of superconductivity obtained from resistivity measurements. Adopted after [36].

both superconductivity and ferromagnetism vanish abruptly at pressure of $p_c = 16$ kbar. Secondly, the superconducting transition temperature T_S is maximised, well inside the ferromagnetic phase, at p_x which is associated with the FM1-FM2 transition. Bulk superconductivity exists both in FM1 and FM2 phases as was confirmed with NQR measurements [37]. A lack of coherence peak in NMR measurements provides further support for non-conventional superconductivity. The coexistence of ferromagnetism and superconductivity requires triplet spin pairing or more to be more precise an odd symmetry real space pairing [27]. Taking all that evidence, UGe_2 is most likely a spin triplet (odd pairing) superconductor with a magnetically mediated superconducting mechanism. However, the pairing is not yet explained.

1.3.2 Previous Elastic Studies of UGe_2

A single crystal of UGe_2 was studied using a pulse echo technique and the temperature dependence of three elastic constants c_{11}, c_{55} and c_{66} was measured [38]. The temperature dependence of c_{11} is summarised in Fig. 1.8 and clearly displays a clear peak associated with the Curie temperature T_C and broad anomaly associated with T^*. All elastic constants showed a peak at T_C, however for c_{55} and c_{66} no clear anomaly at T^* was observed [38].

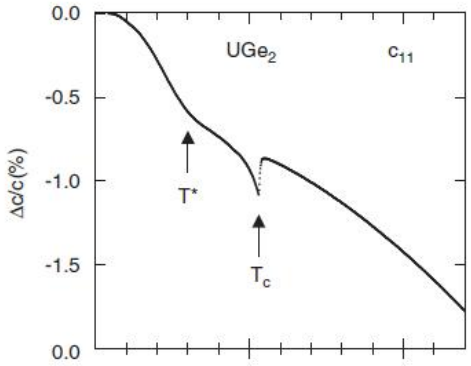

Figure 1.8: Temperature dependence of c_{11}. Adopted after [38].

This short work suggested that T^* is not of phononic origin but related to the magnetic properties [38]. The observed elastic anomaly around T^* was generally conclude to be due to a secondary effect from the anomaly of the magnetization through magneto-elastic interactions and that the T^* anomaly is not related to some second-order phase transition [38].

1.3.3 FM1-FM2 Metamagnetism, Open Questions and Possible Scenarios

As noted above, the first order FM1-FM2 transition associated with metamagnetism may play the key role in the superconducting mechanism of UGe_2. The term metamagnetism was originally used to describe a first order transition where a state of low magnetisation and low susceptibility is changed to a state of relatively high magnetisation and low susceptibility [39]. An instance of a field induced transition is a transition from a paramagnetic state into ferromagnetic state [40].

The field induced transitions belong to two different groups. In highly anisotropic materials, the transition is associated with the spin reversal − an example of such a material is $FeCl_2$ [39]. In weakly anisotropic or isotropic, the transition is typically due to rotation of spins such as in MnF_2 [39]. Schematic phase diagrams of both materials are presented in Fig. 1.9 (a) and (b).

Another class of metamagnetic transitions are pressure induced transitions. Such a transition was observed for example in CoS_2 as presented in Fig 1.9 (c) [41]. In this case, the transition from paramagnetic to ferromagnetic state is second order below 0.4 GPa and at higher pressures it changes to first order and was observed in magnetisation. In the regime of the first-order transition, above 0.4 GPa, the metamagnetic transition takes place [41]. The transitions were observed in magnetisation.

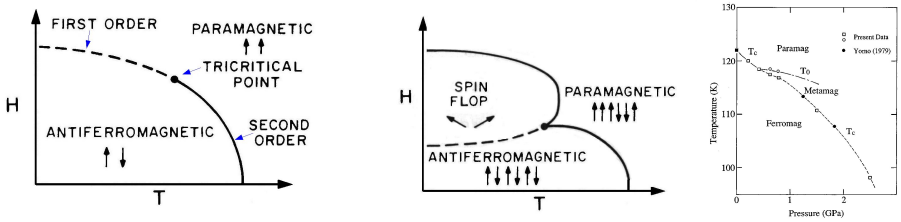

(a) (b) (c)

Figure 1.9: Examples of metamagnetic transitions. The figure includes: (a) schematic phase diagram of $FeCl_2$, (b) schematic phase diagram of MnF_2 (spin flop refers to spin rotation (c) schematic phase diagram of CoS_2 The ferromagnetic transition is second order below p=0.4 GPa and first order above. (a) and (b) adopted after [39] and (c) after [41].

In that context, the metamagnetism in UGe_2 is rather special due to two reasons. Firstly, despite the suppression of T_C with pressure, T_x is still much smaller than T_C, i.e. the metatransition takes place well inside the ferromagnetic phase; and, secondly, it does not exhibit any spin reversal or reorientation − only the magnitude of the moment changes upon the FM1-FM2 transition. Finally, as already mentioned, the FM1-FM2 might play the crucial role for the superconducting pairing mechanism.

The possible accounts on the FM1-FM2 include:

1. **Density of states and Fermi Surface Deformation**
   The proposed explanation is based on the idea that, in contrast to the fixed Fermi surface in a paramagnetic state, the magnetisation in ferromagnetic state is a tuning parameter capable of changing the geometry of the anisotropic Fermi surface of different spin species [42]. The jump in magnetisation, between the FM1-FM2 phases, is explained in terms of two peaks in the density of states (DOS) arising from the low-dimensional bandstructure. The peaks give rise to a zero temperature magnetisation which has two transitions [42]. Another explanation, related to the Fermi topology, presents a series of deformations of the Fermi surface responsible for a weak ferromagnetic phase (FM0), a half-metallic phase (FM1) and also a ferromagnetic phase with polarized $5f$-electrons (FM2) [43]. The Fermi surface changes from large in FM0 to small in FM2. This explanation however, does not predict the first order nature of the FM1-FM2 transition.

2. **CDW and SDW**
   The proposed scenario is based on a charged density wave (CDW) coupled to spin density wave (SDW). It provides an explanation of the main feature of the phase diagram of UGe_2 namely the ferromagnetic superconducting state [44]. The idea was originally suggested due to the observation of the CDW in α-U which shares a zigzagging chains of uranium atoms within its structure with UGe_2. If the FM2 phase was identified as a CDW state and the FM1 phase with no CDW then it would require that FM2 was a thermodynamic state separated by a phase boundary at T_x from FM1 rather than this being simply a cross-over. The CDW and SDW in UGe_2 would be caused by the imperfect nesting of the Fermi surface of majority spin at T_x as obtained by the bandstructure calculation. There is, however, no experimental observation of the CDW or SDW (or coupled) so far (this includes both neutron and x-ray scattering).

3. **Magnetic Critical Fluctuations**
   The proposition is based on the critical ferromagnetic fluctuations due to the FM1-FM2 phase transition. The scenario suggests that superconductivity would be mediated not by phonons but by the critical fluctuations of

magnetisation associated with the FM1-FM2 transition. The theoretical aspects were discussed way before the discovery of ferromagnetic superconductors [45]. The resulting superconducting phase due to the longitudinal spin fluctuations, according to that theory, would be analogous to A1 phase in superliquid ^{3}He. An experimental example of such fluctuation was another uranium based ferromagnetic superconductor UCoGe [46]. It was shown, with the NMR measurements and also neutron scattering, that longitudinal spin fluctuations tuned by external magnetic field remain active in superconducting state. It should be noted though that UCoGe exhibits anisotropic magnetic correlation lengths in contrast to correlation lengths in UGe_2 (at ambient pressure) [46].

This work attempts to experimentally verify the last proposal by ultrasonic measurements and inelastic neutron scattering.

1.4 Thesis Outline

The thesis outline is the following:

- **Chapter 2** will give a formal introduction to theory of elasticity and will discuss the propagation of ultrasound in paramagnetic and ferromagnetic phases and also upon the transition between the two. The sources of ultrasonic velocity and ultrasonic attenuation changes will be presented.
- **Chapter 3** will discuss the production of ultrasound and will give a review of the ultrasonic experimental techniques including the pulse echo method and the resonant technique. The chapter will also briefly review the experimental setups and designs of diamond anvil cells and piston cells. The chapter will conclude with some previous studies using the ultrasonic techniques under high pressures.
- **Chapter 4** will discuss the design and technical aspects of the instrumentation development of the 2-axis Rotation Stage for High Pressures as well as the Ultrasonic Sapphire Anvil cell. The chapter will present the test data

obtained with the developed instruments and will give a outlook for future work.

- **Chapter 5** will give a brief introduction to neutron scattering with a triple-axis spectrometer. The neutron scattering data taken on a single crystal of UGe_2 under pressure will be presented and discussed.
- **Chapter 6** will discuss the high pressure experiments on a single crystal of UGe_2 using the pulse echo technique. The importance of sample preparation and the development of the data collection process will be presented. Finally, the set of result at ambient pressure, high pressures and high fields will be presented and discussed.
- **Chapter 7** will present the thesis conclusions and the future outlooks.

Chapter 2

Theoretical background

The following chapter will review the theory of elasticity and sound propagation in magnetic materials. The ultrasound propagation in paramagnetic and ferromagnetic phases as well as the sources of ultrasonic attenuation and velocities changes will be discussed.

2.1 Theory of Elasticity

Elasticity can be described by a tendency of a solid material to return to its original shape after it was deformed. The simplest description of elastic deformation in 1D is given by Hooke's law

$$F = -kx \tag{2.1}$$

where F is an external force, k is an elastic constant. If a volume element is deformed, one has to use the generalised Hooke's law given by [47]

$$T_{ij} = \sum_{kl} c_{ijkl} v_{kl} \tag{2.2}$$

where T_{ij} is the stress tensor, c_{ijkl} is the elastic stiffness tensor and v_{kl} is the strain tensor. The above expression is valid only for small deformation, i.e. small strains. The elements of the strain tensor can be directly related to deformation. When a volume element at position vector $\mathbf{R}$ is deformed to $\mathbf{R}' = \mathbf{R} + \mathbf{u}(\mathbf{R}, t)$, then the strain tensor components are given as the spatial derivative of the displacement

vector $\mathbf{u}(\mathbf{R}, \mathbf{t})$ [47]

$$v_{ij} = \frac{\partial u_i}{\partial R_j} \tag{2.3}$$

and

$$dR'_i = dR_i + \sum_j v_{ij} dR_j \tag{2.4}$$

It can be noted that if the vector $\mathbf{u}$ is only time dependent then the volume element is only translated in space but not deformed. Finally, the strain tensor can be written in a symmetric way

$$\varepsilon_{ij} = \frac{1}{2}(v_{ij} + v_{ji}) \tag{2.5}$$

As for the stress tensor T_{ij}, it is defined through a force on a volume element [47] in a continuum medium

$$\int F_i dV = \int \sum_k \frac{\partial T_{ik}}{\partial R_k} dV = \int \sum_k T_{ik} df_k \tag{2.6}$$

where $\mathbf{F}$ is the force acting on a volume element dV. df_k represents a component of the surface element vector d$\mathbf{f}$. Due to the angular momentum conservation, the stress tensor is symmetric, T_{ij}=T_{ji} [47].

When a sound wave is present in a solid, the strain components are not constant and vary in time and the wave equation of motion is given by

$$\rho \frac{\partial^2 u_i}{\partial t^2} = \sum_k \frac{\partial T_{ik}}{\partial R_k} \tag{2.7}$$

Combining the above equation with the generalised Hooke's law (2.2) yields

$$-\rho\omega^2 e_i = \sum_{jkl} c_{ijkl} q_j q_k e_l \tag{2.8}$$

where ω is the eigenfrequency for the vector $\mathbf{q}$. The solutions to the equation can be written in the form of a plane wave

$$u_i = U e_i \exp[i(\mathbf{q} \cdot \mathbf{r} - \omega t)] \tag{2.9}$$

where U is the amplitude and $\mathbf{e}$ is the polarization vector.

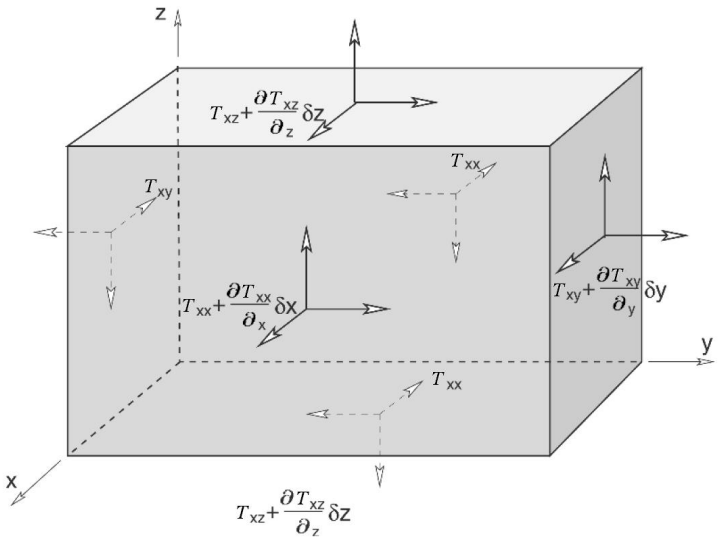

Figure 2.1: Schematic diagram of the components of the stress tensor of a rectangular parallelepiped. Stresses acting on the volume element $dxdydz$ are forces per unit area. On the surface, $dxdy$, there is a normal stress T_{zz} and two shear stresses T_{xz} and T_{yz}. Adopted after [47].

From the generalised Hooke's law, the elastic stiffness tensor can be inverted to the compliance tensor s_{ijkl} and the strain elements can be written in terms of $\mathbf{u}$. Here, it is useful to adopt the Voigt notation which simplifies the expression by reducing the order of tensors – the symmetry of the stress tensor implies that the tensor compoments are independent of the indices ordering [47]. The Voigt notation reads: $(11 \rightarrow 1)$; $(22 \rightarrow 2)$; $(33 \rightarrow 3)$; $(23, 32 \rightarrow 4)$; $(13, 31 \rightarrow 5)$; $(12, 21 \rightarrow 6)$. Therefore, the Hooke's law can be rewritten as

$$T_n = \sum_m c_{nm}\varepsilon_m \tag{2.10}$$

and

$$\varepsilon_n = \sum_m s_{nm}T_m \tag{2.11}$$

To illustrate the Voigt notation, one can consider, for example, c_{12} mode in orthorhombic symmetry, so $T_6 = c_{21}\varepsilon_6 = c_{12}\varepsilon_6$. Also, it follows that $\varepsilon_6 = \varepsilon_{xy} = \frac{1}{2}\left(\frac{\partial u_x}{\partial R_y} + \frac{\partial u_y}{\partial R_x}\right)$ and $u_x = Ue_x\exp[i(q_y y - \omega t)]$, i.e. a standing wave with the y-axis direction of propagation and the x-axis of direction polarisation. Finally, the full

stiffness tensor for an orthorhombic structure [48] which is adopted by the crystal of UGe_2 is given by

$$\begin{pmatrix} c_{11} & c_{12} & c_{13} & 0 & 0 & 0 \\ c_{12} & c_{22} & c_{23} & 0 & 0 & 0 \\ c_{13} & c_{23} & c_{33} & 0 & 0 & 0 \\ 0 & 0 & 0 & c_{44} & 0 & 0 \\ 0 & 0 & 0 & 0 & c_{55} & 0 \\ 0 & 0 & 0 & 0 & 0 & c_{66} \end{pmatrix}$$

In a fully isotropic engineering material, there are two types of sound waves, namely longitudinal and transverse [49]. The sound velocities corresponding to these two different modes can be expressed as $v_L = \left(\frac{K+\frac{4}{3}G}{\rho}\right)^{1/2}$ and $v_T = \left(\frac{G}{\rho}\right)^{1/2}$, where K and G are bulk and shear moduli respectively and ρ is the density of the material [49]. In a crystal, the sound velocities (corresponding to pure modes) can be obtained from the equations (2.7) and (2.8). The sound velocities for an orthorhombic system are summarised in Table 2.1. Table 2.1 does not contain sound velocities associated with the off-diagonal terms in the stiffness tensor corresponding to quasi-transvers and quasi-longitudinal modes. Unlike pure modes, which represent either a density wave (longitudinal) or a shear wave (transverse), they result when the direction of propagation is not along a high axis symmetry [47, 49]. A full summary of the sound velocities is given in the Appendix A.

Mode	**Propagation**	**Polaristion**	**Elastic Constant**	**Sound Velocity**
L	[100]	[100]	c_{11}	$v_{L_1} = \sqrt{c_{11}/\rho}$
T	[100]	[010]	c_{66}	$v_{T_1} = \sqrt{c_{66}/\rho}$
T	[100]	[001]	c_{55}	$v_{T_2} = \sqrt{c_{55}/\rho}$
T	[010]	[100]	c_{66}	$v_{T_3} = \sqrt{c_{66}/\rho}$
L	[010]	[010]	c_{22}	$v_{L_2} = \sqrt{c_{22}/\rho}$
T	[010]	[001]	c_{44}	$v_{T_4} = \sqrt{c_{44}/\rho}$
T	[001]	[100]	c_{55}	$v_{T_5} = \sqrt{c_{55}/\rho}$
T	[001]	[010]	c_{44}	$v_{T_6} = \sqrt{c_{44}/\rho}$
L	[001]	[001]	c_{33}	$v_{L_3} = \sqrt{c_{33}/\rho}$

Table 2.1: Pure sound modes (L=longitudinal and T=transverse), sound velocities and elastic constants for orthorhombic system. ρ is the density of the material. Pure sound modes correspond to diagonal terms in the stiffness tensor.

As far as the sound wave energy is concerned, the sound wave energy density is given by

$$E_{elastic} = \frac{1}{2} C_{ijkl} \varepsilon_{ij} \varepsilon_{kl} \tag{2.12}$$

which is quadratic in strain. It is also possible to express the energy of the wave in terms of the maximum kinetic energy (using the standing wave solution), i.e. $E_{k_{elastic}} = \frac{1}{2}\rho\omega U^2$, where U and ω are given by the wave equation (2.9). The considerations presented so far, assume that the amplitude of the sound wave is constant. In real materials, this is not the case and the energy of a sound wave will be dissipated. Taking this into account, the standing wave equation (2.9) has to be modified and expressed as

$$u_i = U e_i \exp\Big[i\mathbf{q}\cdot\mathbf{r} - i\omega t - \frac{1}{2}\alpha\hat{\mathbf{q}}\cdot\mathbf{r}\Big] \tag{2.13}$$

where α is the ultrasonic attenuation coefficient and it measures how strongly the wave is dissipated with distance in a given direction covered by the wave. The sources of attenuation will be discussed in the next section. It can be clearly seen that the problem of sound propagation so far was treated classically. However, in crystals, the sound wave excitations are quantised and are called phonons.

There are two types of phonons. The acoustic phonons exhibit linear dispersion energies at low q, i.e. $\omega = v_s q$, where v_s is the speed of sound in the given direction. In 3D crystal, three acoustic modes are always present, one longitudinal and two transverse. The optical phonons are present if the unit cell contains more than one type of atom and, as before, they can be also a mixture of both longitudinal and transverse for a general direction.

In the Debye Theory, the linear dispersion relation is valid up to a cut-off Debye frequency ω_D. The Debye frequency can be related to the Debye temperature by $\hbar\omega_D = k_B\Theta_D$ (which is used more often since it gives the characteristic energy scale of the system). The Debye temperature divides the temperature scale into the classical and semiclassical regimes with different thermodynamic properties such as heat capacity:

$$C_V = 3nNk_B \qquad \text{for } T \gg \Theta_D \tag{2.14}$$

$$C_V = \frac{12}{5}\pi^2 k_B \Big(\frac{T}{\Theta_D}\Big)^3 \qquad \text{for } T \ll \Theta_D \tag{2.15}$$

where the above expressions describe a system with n atoms in unit cells, N number of points in Brillouin zone and reciprocal density of states $\frac{V}{8\pi^3}$, with V being the volume of the crystal. Expression (2.14) is referred to as the Dulong-Petit law and (2.15) as the Debye law.

2.2 Sources of Ultrasonic Attenuation and Ultrasonic Velocity Changes

As a sound wave propagates through a material, its energy can be dissipated and its velocity changed due to several reasons. This section presents the mechanisms responsible for such changes.

2.2.1 Anharmonic effects

The Harmonic approximation assumes that the displacement of atoms from their equilibrium position is small and that the energy of the system is calculated by keeping only the leading term in the lattice potential energy. The first assumption is valid in most solid. However, the second one cannot explain several important phenomena observed experimentally such as thermal expansion. Within the harmonic approximation, the elastic constants are temperature independent resulting in no thermal expansion of a crystal. In general, the potential energy includes

$$U = U_{eq} + U_{harm} + U_{anharm} \tag{2.16}$$

where U_{eq} is the equilibrium potential term (i.e. a constant), U_{harm} is the harmonic term of the form of the equation (2.12), quadratic in strain. U_{anharm} is the anharmonic of the order higher than two in strain. The lowest term (third order) in the anharmonic energy can be written as

$$U^{(3)}_{anharm} = \frac{1}{3} C_{ijklmn} \varepsilon_{ij} \varepsilon_{kl} \varepsilon_{mn} \tag{2.17}$$

where C_{ijklmn} is the sixth order elastic stiffness tensor (which can have 729 components in general) and $\varepsilon_{ij,kl,mn}$ are the appropriate strain components. Physically, this term is responsible for coupling between different modes of oscillations. As for the sound waves, it causes an interference between the

mechanical excitations and the thermal excitations already present in a system [50].

As for the elastic constants, their temperature dependence can be obtained from the free energy analysis. In general the elastic constant obtained by minimising the free energy with respect to strain is given by

$$c_{ij}(T) = c_{ij}^{o} - \frac{1}{2}\Gamma_{ij}U(T) + \frac{1}{4}\gamma_{ij}\Big(U(T) - TC_V(T)\Big) \tag{2.18}$$

where $U(T)$ is internal energy and Γ is the derivative of the Grüneisen parameter and where the Grüneisen parameter is given by [47]

$$\gamma_{kl} = \frac{\partial ln\langle\omega^2\rangle}{\partial\varepsilon_{kl}} \tag{2.19}$$

Finally, C is the specific heat capacity and can be written as [47]

$$C_V = \frac{dU}{dT} = \frac{d\sum_q E(\omega_q, T)}{dT} \tag{2.20}$$

where E is the energy of an oscillator with q being the occupation phonon number. Equation (2.18) can be considered in two temperature limits [47]

$$c_{ij}(T) - c_{ij}^{o} \propto -T \qquad \text{for } T > \Theta_D \tag{2.21}$$

$$c_{ij}(T) - c_{ij}^{o} \propto -T^4 \qquad \text{for } T < \Theta_D \tag{2.22}$$

In practice, it can be difficult to estimate the ranges of the above limits and the phenomenological expression is used instead which is given by [51]

$$c_{ij}(T) = c_{ij}^{o} - \frac{a}{e^{b/T} - 1} \tag{2.23}$$

with two free parameters a and b.

2.2.2 Crystal Defects

Crystal defects, such as dislocations, are obvious (but hard to quantify) sources of the ultrasonic attenuation. They are produced in a crystal growth when a crystal is strained above its elastic limit. Dislocations can be modelled as line segments whose behaviour can be described analogously to a vibrating string under the influence of alternating stress fields [52]. In a more detailed model [53], a crystal is assumed to contain dislocation loops coming from the dislocation network with both edge-type and screw-type. The loops of shorter length display damping behaviour of resonant type, which is a result of a phase difference between the stress and strain. For higher stresses, the short loops may break away from the pinning point and create loops of larger length [54]. Following that, longer loops may then collapse, break down and be repinned back again [54]. However, for small stresses, it is assumed that the unpinning does not take place – such an assumption is taken to be true for high frequency oscillations [54]. The temperature dependence of the dislocation damping is complicated. It might be given through the specific damping constant and it was shown [53] to have a linear temperature dependence. However, some additional effects such as the Bordoni peaks can take place [54].

The Bordoni peaks are observed in the ultrasonic attenuation coefficient (in both single crystal and polycrystalline samples) at temperatures of roughly one-third of the Debye temperature [55, 56]. One of the features of the Bordoni peaks is that their positions do not depend on prestrain suggesting an intrinsic dislocation mechanism (which is also independent of the dislocation length) [54]. This is in contrast with the mechanism discussed above (dependent of the length of dislocations). The Bordoni peaks result from the relaxation processes involving dislocations. Crystal impurities reduce the height of the peak and change its position towards lower temperatures. It should be noted that temperature at which the peak is positioned depends on the frequency of the wave. This temperature increases with increasing frequency [54].

2.2.3 Magnetic Domains

Internal strain can affect the motion of the magnetic domain walls [57]. Such coupling leads to magnetomechanical losses and is a source of ultrasonic

attenuation. The magnetic walls can move or vibrate due to a presence of an ultrasonic stress wave. A vibrating wall causes a changing magnetic field creating induced currents resulting in energy losses of the ultrasonic wave. In a model with 180° spin wall [54], the magnetisation is assumed to be harmonic in time which allows a calculation of a current density and the power per unit area for a given thickness of a wall. Within the model, it is assumed a plane ultrasonic wave with frequency f will cause a wall to oscillate with the same frequency. The amplitude and the phase of these vibrations depend only on the frequency f and the strain [54].

2.3 Ultrasound Propagation in Magnetic Materials

In a magnetic material, the ultrasonic waves can couple to magnetic ions and to collective magnetic excitations leading to a phonon-spinwave interaction. The coupling can take place between the ultrasonic wave and the localised magnetic moments but also between the wave and the itinerant electrons.

2.3.1 Coupling to localised moments

Coupling between the ultrasonic wave and the localised moments can be caused by two different effects. The first one is the single-ion coupling whereby the strain changes the ion environment by changing the crystal electric field [58]. The second one is the two-ion coupling whereby the strain modulates the distance between the ions [58].

In general, using the symmetry strains of the irreducible representation Γ combined with the multipolar operator, the magneto-elastic one-ion Hamiltonian is given by [59]

$$H_{ME} = \sum_i g_{\Gamma,i} \varepsilon_\Gamma O_{\Gamma,i} \tag{2.24}$$

where $g_{\Gamma,n}$ are the magneto-elastic coupling constant and $O_{\Gamma,i}$ is the multipolar operator.

In order to illustrate the magneto-elastic Hamiltonian for the one-ion case, one can consider the orthorhombic symmetry [60], where

$$\begin{aligned} H_{ME}^{\text{ortho}} &= g_{10}^{1}\varepsilon_{xx}O_2^0 + g_{11}^{1}\varepsilon_{xx}O_2^2 \\ &+ g_{20}^{1}\varepsilon_{yy}O_2^0 + g_{21}^{1}\varepsilon_{yy}O_2^2 \\ &+ g_{30}^{1}\varepsilon_{zz}O_2^0 + g_{31}^{1}\varepsilon_{zz}O_2^2 \\ &+ g^2\varepsilon_{xy}O_{xy} + g^3\varepsilon_{xz}O_{xz} + g^4\varepsilon_{yz}O_{yz} \end{aligned} \tag{2.25}$$

where g_{ij}^{k} and g^k are the magneto-elastic coefficients, ε_{ij} are the strain components with $i, j = x, y, z$ corresponding to the orthorhombic symmetry and the multipolar operators can be expressed through a linear combination of the Stevens operators consisting of the angular momentum components, for example $O_2^0 = 2J_z^2 - J_x^2 - J_y^2$ (the full list can be found in [59, 60]). The magneto-elastic Hamiltonian (2.25) holds for small strains so all the terms are linear in strain. This is true in the absence of structural transitions and magnetic ordering (i.e. paramagnetic phase) [60]. Hence, even in the paramagnetic state the magneto-elastic coupling can take place causing perturbation to the system energy spectrum [60]. For a ferromagnetic phase, the quadrupole-quadrupole interactions have to be taken into account and the Hamiltonian will be expressed in the form $H_{ME} = \sum_{ij} K_{ij}O_{\Gamma,i}O_{\Gamma,j}$ [59–61].

Finally, that the above considerations do not take into account the more complicated structures where one needs to take into account internal and external strains [58].

The magneto-elastic coupling for the two-ion case comes from a modulation of the exchange interaction which is given by [58]

$$H_{Exe} = \sum_{ij}[J(\boldsymbol{\delta} + \mathbf{u}_i - \mathbf{u}_j) - J(\boldsymbol{\delta})]\mathbf{S}_i \cdot \mathbf{S}_j \tag{2.26}$$

where the $\boldsymbol{\delta} = \mathbf{R}_i - \mathbf{R}_j$ is the distance between the magnetic ions. Substituting from the equation (2.9) and expanding in terms of $\mathbf{u}_i$ (the displacment of the ion $\mathbf{R}_i$) yields

$$H_{Exe} = \sum_{k}\left(\frac{dJ}{dr}\frac{\boldsymbol{\delta}}{\delta}\cdot\mathbf{e}_k\right)(\mathbf{q}\cdot\boldsymbol{\delta})(\mathbf{S}_k\cdot\mathbf{S}_{k+\delta})\exp\left(i(\mathbf{q}\cdot\mathbf{R}_k - \omega t)\right) \tag{2.27}$$

The above equation shows that, for the propagation along the symmetry axis,

only the longitudinal waves couple to the magnetic ions in the lattice since $\boldsymbol{\delta} \parallel \mathbf{q}$ [58]. This effect is responsible for the critical behaviour of ultrasonic attenuation near the magnetic phase transition [58]. The coupling constant dJ/dr could be estimated through the magnetic Grüneisen parameter and the pressure dependence of the Currie temperature

$$\Gamma_{magnetic} = \frac{\partial \ln J}{\partial \ln V} = -c_B \frac{\partial \ln T_C}{\partial p} \tag{2.28}$$

where c_B is the bulk modulus.

2.3.2 Coupling to Itinerant Electrons

The ultrasonic waves can also couple to itinerant electrons provided sufficiently low temperatures [54, 62]. Here, one can consider two limits coming from the comparison between the electron mean free path l and the ultrasound wavelength $\lambda = 2\pi/q$.

For the hydrodynamic limit ($lq \ll 1$), electrons can be treated, from the point of view of the lattice, as a viscous fluid that is dragged along with the slow moving sound wave – electrons scatter from one another and their equilibrium velocity is centred around a local lattice point which can move under the influence of the ultrasonic wave [63]. This mechanism is sometimes called the collision drag effect [64–66]. The effect takes place at temperatures for which the dislocations are frozen and do not attenuate the ultrasonic wave; below 20 K approximately as shown on Fig 2.2.

Within the viscous model, the attenuation of the transverse wave can be written as [67]

$$\alpha_t = \frac{2\pi^2 \nu^2 \eta}{\rho v_t^3} \tag{2.29}$$

and of the longitudinal wave

$$\alpha_l = \frac{8\pi^2 \nu^2 \eta}{3\rho v_l^3} \tag{2.30}$$

where ν is the frequency, η is the viscosity, ρ is the density and v_t and v_l are the transverse and longitudinal velocities respectively. The expression for the

viscosity can be obtained from the kinetic theory and can be written as

$$\eta = \frac{lNm\bar{v}}{3} \tag{2.31}$$

where N is the number density of particles, m is the mass of a particle, l is the mean free path and $\bar{v}$ is their average velocity. For electrons, $\bar{v} = \bar{v}_F$ can be derived from the Fermi-Dirac distribution yielding

$$\alpha_t = \frac{Nmv_f}{5\rho v_t}\nu^2 l \tag{2.32}$$

and

$$\alpha_l = \frac{4Nmv_f}{15\rho v_l}\nu^2 l \tag{2.33}$$

v_f is the Fermi velocity.

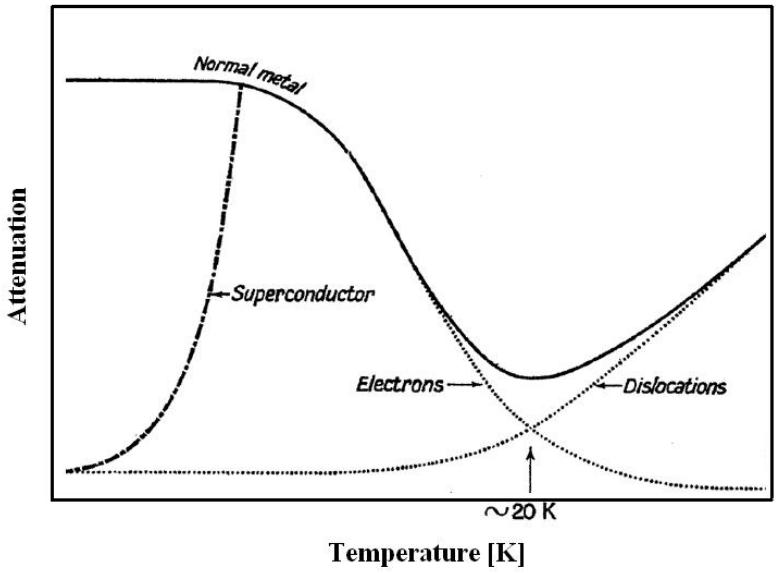

Figure 2.2: General behaviour of the ultrasonic attenuation as a function temperature for a metal. As temperature decreases, the dislocation become less thermally excited and stop attenuating the ultrasonic wave. At low temperatures, the attenuation is dominated by the electrons due to the viscosity of the electronic fluid. In a superconducting metal, the ultrasonic attenuation is strongly and sharply decreased indicating the phase transition. Adopted after [62].

For the quantum limit ($lq \gg 1$), the idea of the electron viscous fluid cannot be applied and it was found that the attenuation is anomalously large [68]. The effect

was identified as the electron-phonon interaction whereby a phonon decays into an electron-hole pair [68]. The energy conservations requires that $\varepsilon_{\mathbf{k}+\mathbf{q}} - \varepsilon_{\mathbf{q}} = \hbar\omega_{\mathbf{q}}$, where $\varepsilon_{\mathbf{q}}$ is energy of an electron and $\hbar\omega_{\mathbf{q}}$ is energy of a phonon. Since, $\mathbf{q}$ is small, the electron energy difference can be expanded and expressed as

$$\mathbf{v}_{\mathbf{k}} \cdot \mathbf{q} = \omega_{\mathbf{q}} = v_s q \tag{2.34}$$

where v_s is the sound velocity and $\mathbf{v}_{\mathbf{k}} = \frac{1}{\hbar}\nabla\varepsilon_{\mathbf{k}}$, i.e. electron wave packet velocity centred at $\mathbf{k}$ [63].

2.3.3 Coupling to Spin-waves

The ultrasonic wave can couple to a spin-wave. In a system with no interactions between the lattice and spins, the dispersion relations for phonons and magnons can be treated independently. However, when coupling is present any disturbance that propagates in the system is a combination of spin and stress waves [54]. To keep the discussion clear, one can consider a simple BCC lattice. The description of the system with the magneto-elastic coupling is given in terms of the equation of motion for magnetization [69, 70] and the dispersion can be written as

$$(\omega + \omega')\left(\omega^2\rho - \frac{1}{2}k^2C\right) \pm \left(\gamma\frac{k^2b_2^2}{M_s}\right) = 0 \tag{2.35}$$

where ω' is the spin resonance frequency given by

$$\omega' = \omega_0 + 2\frac{Ak^2\gamma}{M_s} \tag{2.36}$$

where M_s is the saturation magnetisation and constants $A = 2JS^2/a$ and $\omega_0 = \gamma H_0$. J is the exchange integral for the b.c.c lattice, S is the spin in units of $\hbar$ and a is the lattice constant [54]. b_2 is the magneto-elastic coupling constant, C is the elastic constant and γ is the gyromagnetic ratio for the electron [54].

The dispersion relation (2.35) with different branches is shown in Fig. 2.3. The dashed lines indicate the dispersions with no coupling: $\mathbf{w_p}$ for phonons and $\mathbf{w_s}$ for the spins. The solid lines $\mathbf{w_{ME}}$ indicate the dispersion for coupled waves; one branch starts at ω_0 and initially shows more spin-like behaviour and then more phonon-like dependence for higher values of k. The second branch starts at

the origin and is initially phonon-like but as k increases it becomes more spin-like.

Finally, it was shown [70] that the attenuation per wavelength is expressed as the following ratio

$$\frac{k_2}{k_1} \approx \frac{\omega_s \tau}{\alpha} \left(\frac{b_2}{M_s} \right)^2 \tag{2.37}$$

where τ is the spin relaxation time, $\omega_s = \gamma H_s$ and $k = k_1 - ik_2$ and assuming that $k_2 \ll k_1$.

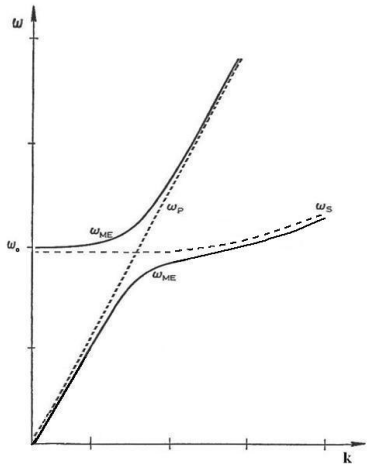

Figure 2.3: Magneto-elastic dispersion curves. $\mathbf{w_p}$ and $\mathbf{w_s}$ indicate curves for no interaction between a spin-wave and phonons. $\mathbf{w_{ME}}$ are the branches when spin-phonon coupling is present.

2.4 Ultrasound Propagation at a Magnetic Phase Transition

Magnetic phase transitions can affect both ultrasonic velocity and ultrasonic attenuation. The critical behaviour of acoustic quantities at a phase transition is expected due to the spin-phonon coupling described above. One can simply consider an energy transfer from the ultrasound wave to the spin system whose relaxation times (or correlation lengths) diverge at the critical temperature. The energy transfer is related to the attenuation, hence the critical behaviour can be observed in the ultrasonic attenuation coefficient or ultrasonic velocity.

In general, the exchange interaction is the dominant interaction responsible for magnetic phase transition [71] and the magneto-elastic coupling plays only a

secondary role. This is manifested for example in Gadolinium. The ultrasonic attenuation in Gadolinium for different crystallographic directions is in shown in Fig. 2.4. The results show that only longitudinal wave couple to the spin system which is expected from the expression (2.26).

It can be shown that the ultrasonic attenuation coefficient for an isotropic ferromagnet is given by [71]

$$\alpha \propto \omega^2 \chi^{1/2} \tau_c \tag{2.38}$$

where χ is the spin susceptibility, τ_c is the characteristic relaxation time and ω^2 comes from the linear dependence of a phonon vector $\mathbf{q}$ in the space-time Fourier-Laplace transform of a four-spin correlation function [71].

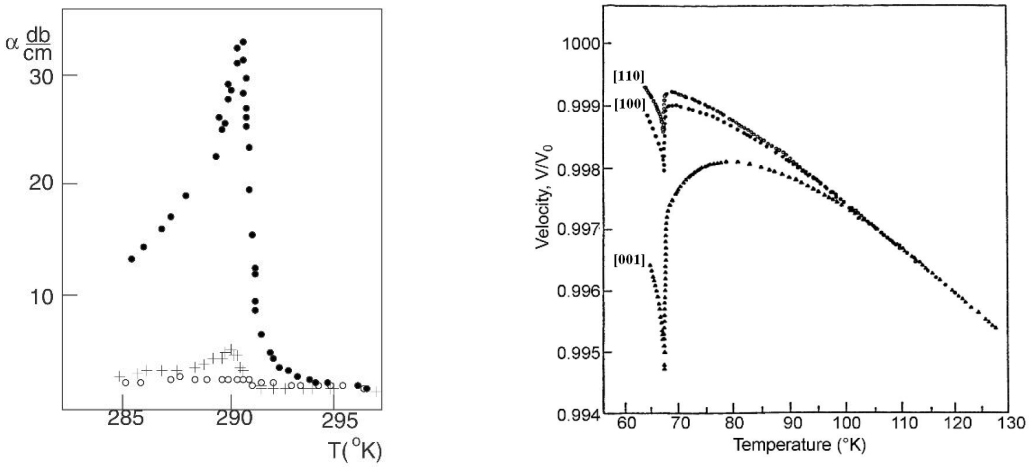

(a) (b)

Figure 2.4: (a) Ultrasonic attenuation for Gadolinium. Full circles show longitudinal waves along the c-axis, crosses along a-axis whereas open circles indicate shear wave along the c-axis. After [71] (b) Ultrasonic velocity in MnF_2 for longitudinal wave for different crystallographic directions. After [72].

As for the sound velocity, its critical behaviour can be derived from considerations of the magnetic free energy [71] and can be expressed as

$$\frac{\Delta v}{v_0} \propto -\omega^n (T - T_c)^{\zeta} \tag{2.39}$$

This result was confirmed experimentally for example in MnF_2 [72] or $RbMnF_3$ [73].

2.5 Ultrasound propagation in f-electron systems

The coupling between ultrasonic waves and localised moments as well as conduction electrons was already introduced above. Here, the coupling will be reviewed more specifically in the context of f-electron systems.

Coupling with local f-electrons.
The Hamiltonian describing the direct coupling between macroscopic strain of symmetry Γ to multipolar operators is given by [74].

$$H = -\sum_i g_{\Gamma,i}\varepsilon_\Gamma O_{\Gamma,i} - \sum_{ij} G'_{ij} O_{\Gamma,i} O_{\Gamma,j} \tag{2.40}$$

where $g_{\Gamma,i}$ is the magneto-elastic coupling constant and G'_{ij} appears if there is a quadrupole-quadrupole interaction mediated by the conduction electrons. The appropriate elastic constants can be expressed as [74].

$$c_\Gamma = c^0_\Gamma - \frac{g^2_\Gamma N' \chi_\Gamma}{1 - g'\chi_\Gamma} \tag{2.41}$$

where c^0_Γ is the background elastic constant and $g' = \sum_{ij} G'_{ij}$ and χ_Γ is the single ion strain susceptibility given by

$$\chi_\Gamma = \frac{\partial^2 F}{\partial \varepsilon^2_\Gamma} \tag{2.42}$$

χ_Γ is the response of the f-electron system to the applied strain and F is the free energy density [74].

Coupling with conduction electrons.
The coupling between ultrasonic waves and conduction electrons can be expressed as

$$E_k = E^0_k + d_{k\Gamma}\varepsilon_\Gamma \tag{2.43}$$

where E_k denotes single particle electron state and $d_{k\Gamma}$ is the deformation potential coupling constant [74]. The appropriate elastic constants can be expressed as

$$c_\Gamma = \frac{\partial^2 F_{el}}{\partial \varepsilon^2_\Gamma} \tag{2.44}$$

F_{el} is the free energy for conduction electrons. One can show that for a degenerate two band model the elastic constant can be written as

$$c_\Gamma = c_\Gamma^0 - 2d^2N(1 - e^{-(E_f - E_0)/k_BT}) \tag{2.45}$$

N is the density of states. This is sometimes called "band Jahn-Teller effect" formula [74].

The above effects can be observed experimentally if the magneto-elastic or deformation potential coupling constants are large. For example, in the case of the Kondo lattices the strength of the deformation potential coupling can be estimated with the electronic Grüneisen parameter

$$d_{\Gamma_1} = \Omega < E > \tag{2.46}$$

$< E >$ is the typical energy band width of the order of T_K. T_K is a characteristic fluctuation temperature. In a simplified view, the Curie–like high temperature susceptibility saturates below a fluctuation temperature T_K in an enhanced Pauli–type susceptibility characteristic for a non-magnetic Fermi liquid ground state [75]. T_K gives the relevant energy scale for the system. Magnetoelastic effects become pronounced if the energy k_BT_K is smaller than the crystal field splitting [74].

In general for heavy fermions materials, three different temperature regimes can be distinguished [75]:

1. The high temperature background regime dominated by the anharmonic effects (described in 2.2.1)
2. The crystal field regime where the magneto-elastic coupling is operative in the region of the crystal field splittings (described by coupling with local f-electrons)
3. And the low temperature regime ($T < T_K$) where the Grüneisen parameter coupling is important.

UPt_3 is an example of a heavy fermion material whose elastic constant and attenuation coefficient was investigated as a function of temperature. For

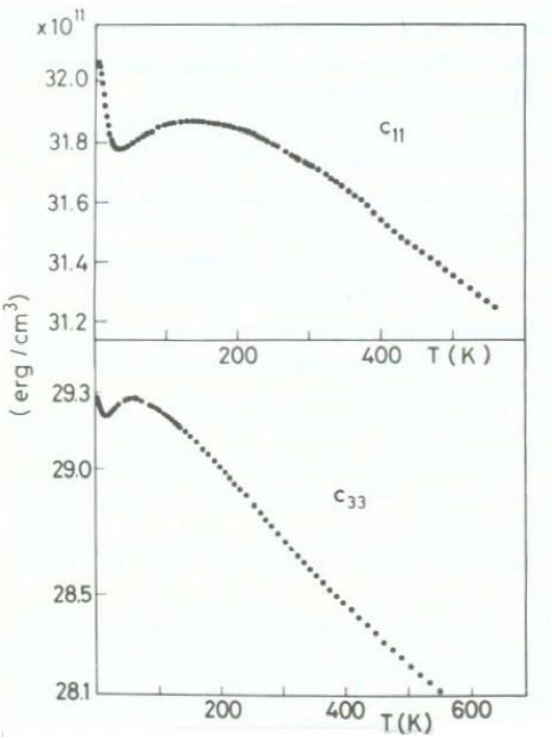

Figure 2.5: Elastic constants and linear thermal expansion of UPt_3. Adopted from [74].

temperature below 50 K, the elastic constants c_{11} and c_{33} display anomalous behaviour due to deformation potential effects [74] and can be explained using a two band model. The corresponding Grüneisen parameter was of the order of $\approx$ 60 and the elastic constants could be fitted with a single band model of $< E > =$ 20 K. Finally, the value of the longitudinal ultrasonic coefficient using the Eq 2.32 was estimated to be $\alpha_l \approx 1\,\mathrm{cm}^{-1}$ at T =0.5 K, ν =500 MHz and $v_F/v_l = 1.7$ which was with reasonable agreement with the measured value of $\alpha_l \approx 0.3\,\mathrm{cm}^{-1}$ [74]. Above 150–180 K, the temperature dependence of the elastic constants can be explained by the anharmonic effects and can be fitted using Eq. 2.24.

Chapter 3

Review of Experimental Techniques

This chapter provides a brief review of the experimental techniques used in the project. The principles of construction and operation of the pressure cells, opposed anvil and piston cylinder types, are discussed. Two different ultrasonic techniques as well as the production of ultrasound are presented.

3.1 Motivation for Use of Different Techniques

High pressures and fields at cryogenic temperatures are essential to perform the experiments to study the phase diagram of UGe_2 but so are the fine tuning capabilities of the pressure cells – these include stable hydrostatic sample environment as well as fine pressure calibration and adequate pressure step sizes. In this project, the high pressure cells were combined with two ultrasonic techniques, namely the pulse echo technique and the resonant ultrasound spectroscopy. The former one was used in the piston type cell, whereas the latter was used in the sapphire anvil cell. Apart from the ultrasonic measurements, a high volume piston pressure cell was used to collect the inelastic neutron scattering data.

All these techniques are indispensable to probing the phase diagram and understanding different properties of UGe_2.

3.2 Ultrasonic Measurements

This section reviews the ultrasonic techniques and the production of ultrasound.

3.2.1 Piezoelectricity and Production of Ultrasound

The most widespread method of generating ultrasonic waves is by using piezoelectric transducers. A varying external electric field causes a piezocrystal to deform allowing production of high frequency vibrations provided sufficient conditions such as thickness of the piezocrystal. The piezoelectric effect can be described using the Voigt notation (introduced in the previous chapter) by expressing the stress as [76]

$$T_i = c_{ik}\varepsilon_k - e_{ij}E_i \tag{3.1}$$

where c_{ik} is the elastic stiffness tensor, ε_k is the strain tensor, e_{ij} are the piezoelectric stress coefficients and E_i represents the components of the external electric field. The inverse relation yields strain as a function of external field [76]

$$\varepsilon_i = s_{ik}T_k + d_{ij}E_i \tag{3.2}$$

where s_{ik} is the compliance tensor and d_{ij} is equal to e_{ij}^{-1}, i.e. inverse of the piezoelectric coefficients. One needs to be careful with the above notation. The piezoelectric matrix in contracted notation is given by e_{ij} with $i = 1, 2, 3$ (three directions) and $j = 1, 2, 3, 4, 5, 6$ (six components of the stress tensor) [76].

Examples of the piezoelectric materials include quartz, berlinite, Rochelle salt or lead titanate. In this work, lithium niobate ($LiNbO_3$) and lead zirconate titanate (PZT) crystals were used. The piezoelectric stress coefficients of lithium niobate are given by [76]

$$e_{ij}^{\mathrm{LiNbO_3}} = \begin{pmatrix} 0 & 0 & 0 & 0 & e_{15} & -e_{22} \\ -e_{22} & e_{22} & 0 & e_{15} & 0 & 0 \\ e_{31} & e_{31} & e_{33} & 0 & 0 & 0 \end{pmatrix}$$

and for lead zirconate titanate by [77]

$$e_{ij}^{\mathrm{PZT}} = \begin{pmatrix} 0 & 0 & 0 & 0 & e_{15} & 0 \\ 0 & 0 & 0 & e_{15} & 0 & 0 \\ e_{31} & e_{31} & e_{33} & 0 & 0 & 0 \end{pmatrix}$$

The units of e_{ij} are $\frac{\mathrm{C}}{\mathrm{m}^2}$ and the units of d_{ij} are $\frac{\mathrm{C}}{\mathrm{N}}$. The geometry of the piezocrystal is crucial to the vibrational behaviour of the crystal. The type of sound wave produced by the piezocrystal depends on the way the crystal is cut and also the position of the leads, i.e. the direction in which the external electric field is applied. The resonant frequency will also depend on the shape of the piezocrystal. In general, the thickness of the piezocrystal fixes the resonant frequency since the fundamental frequency corresponds to the half-wavelength of the standing wave in the crystal. For example, to achieve a frequency of 5 MHz in a piezocrystal of specified geometry with a speed of sound of 5000 $\frac{\mathrm{m}}{\mathrm{s}}$, the thickness of the crystal must be 500 μm.

3.2.2 Pulse Echo Technique

In a simple setting, a piezoelectric transducer is attached, by mechanical clamping or by chemical bonding, to a sample and acts as emitter and receiver of ultrasonic waves (pulses). The initial pulse transmitted to the sample, travels through it and then gets reflected backwards to the transducer from the back end of the sample. The reflected wave is then changed into an electrical signal. This technique can be used for a direct measurement of the absolute speed of sound. By measuring the speed of sound and knowing the density of a material, one can then deduce the elastic constants.

Connection between the transducer and the sample is very important in order to avoid strong attenuation and distortion of the signal [54, 76]. If chemical bonding is used, it has to be ensured that a minimal amount of the couplant is used and that it is evenly distributed between the transducer and the sample. Furthermore, the pulse echo technique requires two other conditions, namely flatness and parallelism, in order to eliminate any unwanted reflections or interference between initial pulse and the subsequent echoes. An ultrasonic wave with the frequency of 50 MHz and ultrasonic speed of 5000 $\frac{\mathrm{m}}{\mathrm{s}}$ has a corresponding

wavelength of $100\,\mu m$. Therefore, an average surface roughness of $10\,\mu m$ (or less) is more than adequate for such a wave. In this work, chemical bonding was used, since mechanical clamping could not be implemented within the pressure cells (more details are presented in Chapter 6).

The width and height of the initial pulse are restricted by the size of the sample. In order to resolve the echoes coming from the sample, the width of the pulse τ must be smaller than the transit time t_T [63], i.e. the total time that it takes for the initial pulse to travel through the sample twice (the pulse is reflected by the back of the sample, hence the factor of two). So, $\tau < t_T$, and

$$t_T = \frac{2l}{v} \tag{3.3}$$

where l is the length of the sample and v is speed of sound in a given direction and with given polarisation. For experiments at ambient pressure, the choice of the pulse widths is greater compared to the experiments at high pressures. This is simply due to restricted sample space in the high pressure cells. For a sample of a length of 1 mm and with an ultrasonic speed of $5000\,\frac{\mathrm{m}}{\mathrm{s}}$, the transit time t_T is $0.4\,\mu s$, so the pulse width must be smaller (the subsequent echoes would be resolved easily even if the pulse width is a half of the transit time). However, a sharp initial pulse is more desirable since it allows for greater precision in identifying the peak position of the subsequent echoes and hence greater precision in determining the speed of sound (assuming precise measurements of the sample length). An example of the pulse echo data is presented in Fig 3.1.

The measured echo spectrum can be used to calculate the ultrasonic attenuation. The amplitude of the ultrasound pulse can be written as

$$A = A_0 e^{-\alpha t} \tag{3.4}$$

where α is the ultrasonic attenuation measured in units of Nepers/second ($\frac{\mathrm{Np}}{\mathrm{s}}$). Considering two pulses n_1 and n_2 at time t given by [54]

$$A_1 = A_0 e^{-\alpha n_1 t} \quad \text{and} \quad A_2 = A_0 e^{-\alpha n_2 t} \tag{3.5}$$

Rearranging the above equation yields the attenuation coefficient expressed in

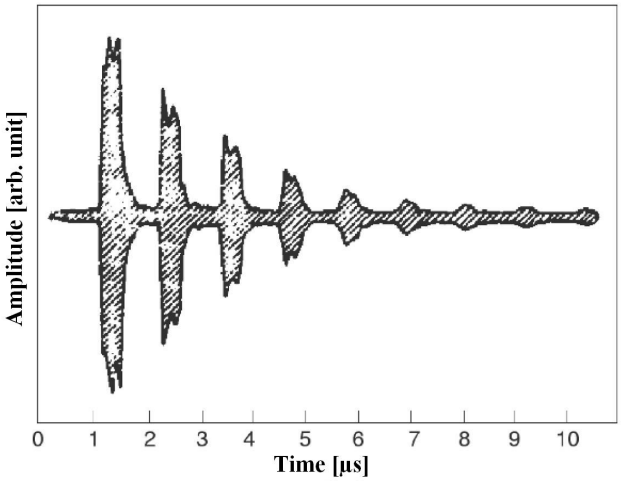

Figure 3.1: Example of the pulse echo data taken on URu_2Si_2. Adopted from [76].

terms of the amplitudes of the two echoes

$$\alpha = \frac{\ln(A_1/A_2)}{(n_2 - n_1)t} \tag{3.6}$$

measured in $\frac{\mathrm{Np}}{\mathrm{s}}$. The unit is often changed into decibels (dB), where 1 $\frac{\mathrm{Np}}{\mathrm{s}}$ = 8.6859 $\frac{\mathrm{dB}}{\mathrm{s}}$. There are several difficulties one has to address when measuring the ultrasonic attenuation. These include losses of the ultrasonic signal due to inadequate coupling, impedance mismatch or misalignment of a sample. Another problem is diffraction effects. They take place because the ultrasonic signal is not confined to a well-defined region of a sample directly below the transducer as it would be for a collimated beam. Instead, the signal spreads generating a diffraction field and some energy is lost from that region. If the spread is strong, additional reflections from the side of the sample might take place causing unwanted interference effects. Diffraction effects are more pronounced for low frequencies and small transducers.

In order to collect data, an oscilloscope and a wave generator are used. Both instruments should be sufficiently fast in order to resolve the echoes. This means that the instruments should operate at high enough frequencies. A pulse width $\tau = 10\,\mathrm{ns}$ corresponds to a frequency bandwidth $1/\tau = 100\,\mathrm{MHz}$. With the bandwidth of that order, an impedance match has to be ensured between all parts in the circuitry. Coaxial cables have to be used in order to minimise noise. Depending on the type of experiment, a pulse can be produced by chopping a

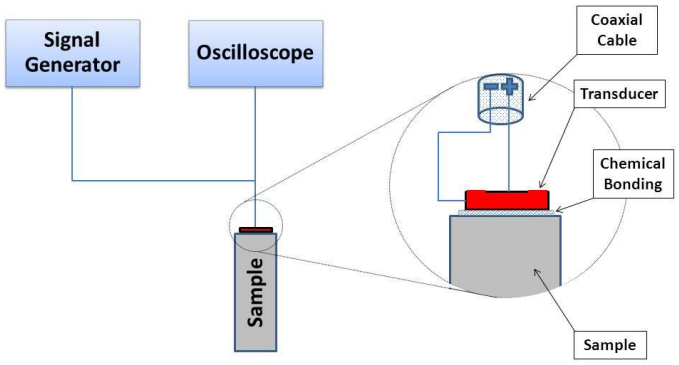

(a)

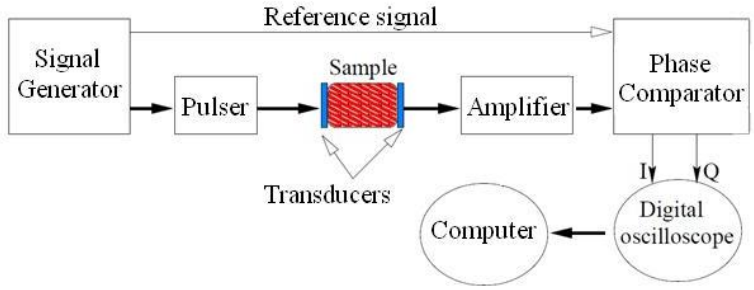

(b)

Figure 3.2: **(a)** Schematic diagram of a simple pulse echo setup with a single transducer. The same transducer generates the signal and detects the echoes coming from the sample. **(b)** Schematic diagram of a pulse echo setup with two transducer – the typical setup employs the heterodyne spectrometer which mixes signals of two different frequencies in order to produce a new one. Adopted after [63].

continuous sinusoidal signal or simply by the single pulse mode. The former method can be used when the sample size is not an issue and thus the pulse widths can be greater; the latter is appropriate for experiments where samples sizes are small and hence the choice of the pulse widths is restricted. It should be noted, that the single pulse mode is more suitable for thin film piezocrystals since a time delay within a finite thickness piezocrystal can distort the shape of the echoes.

Finally, a simple schematic diagram of a pulse echo setup with a single transducer is presented in Fig. 3.2 (a) and the setup with two transducers in Fig. 3.2 (b). In a typical setup [76], frequency generator (tougher with a pulser)

is set to produce a frequency between 10−500 MHz is chosen depending on the experiment. A reference signal is also send to the phase comparator in order to compare the phase of the input and output signals. The in phase signal is labelled as I and out of phase signal as Q in Fig. 3.2 (b). The pulses are amplified with a power amplifier. In some experiments [63], the heterodyne spectrometer can be used meaning that the new frequencies are created by mixing two frequencies and the final detection is done at a fixed frequency. A detailed description of electronics can be found in [54], [63] or [76].

3.2.3 Resonant methods

Resonant methods, which are designed to detect the resonant frequencies of a sample, can also be used to measure the absolute speed of sound and the elastic constants. The main difference, compared to the pulse echo technique, is that the transducer is driven continuously at different specified frequencies or over a range of frequencies. The frequency spectrum can be measured as a function of temperature or external magnetic field. The method usually utilises two transducers (one emitter/drive and one receiver/pickup), but a single transducer setup can be also used.

The most powerful resonant method is the resonant ultrasound spectroscopy (RUS) sometimes called shape resonance technique [76, 78, 79]. The method allows for the determination of all elastic constants in a single measurement for a well-defined defined sample geometry, usually a parallelepiped, sphere or cylinder. The drive transducer is swept through a range of frequencies and the pickup one is used to detect the response from the sample. Unlike the pulse echo technique, RUS method does not require careful bonding between the sample and the transducers since the sample at resonance acts as a signal amplifier [79]. In fact, a point contact is required in order to achieve free boundary conditions which are necessary for the excitations of all the modes in the sample, Fig. 3.3. Furthermore, the point type contact reduces loading on the sample, which in turn ensures that the resonant peaks in the measured spectrum will be sharper.

The analysis of the RUS results requires computer simulations of the frequency spectrum through solving an eigenvalue problem. To solve the problem one needs to write the Lagrangian with elastic kinetic and elastic potential energies in a tensor form. Minimising the Lagrangian yields the eigenvalue problem in the

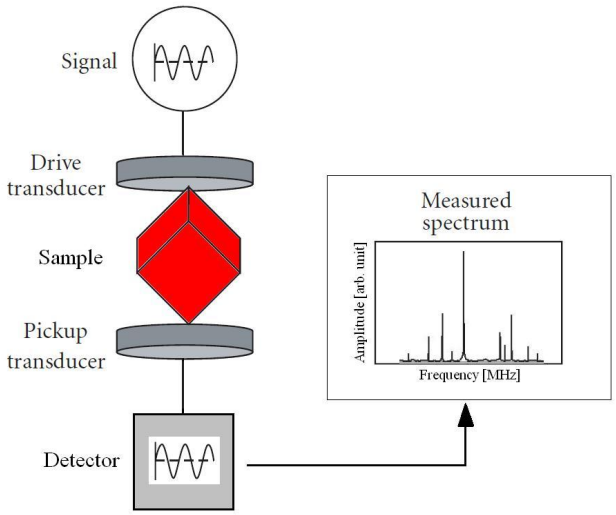

Figure 3.3: Schematic diagram of the resonant ultrasound spectroscopy (RUS) setup. The drive transducer is excited continuously over a range of frequencies. The pickup transducer detects the sample's response. The sample is clamped by its corners between the transducers ensuring free boundary conditions. Adopted after [78].

form of [76]

$$\Gamma \mathbf{a} = \rho\omega^2 E \mathbf{a} \tag{3.7}$$

where Γ corresponds to the potential energy tensor and E to the kinetic energy tensor and $\mathbf{a}$ are the eigenvectors with the corresponding $\rho\omega^2$ eigenvalues. Vectors $\mathbf{a}$ are expressed through the displacement vector

$$u_i = \sum_{\lambda} a_{\lambda i} \Phi_{\lambda} \tag{3.8}$$

The choice of the basis set depends on the geometry of the sample. Solutions of the equation give the set of normal modes and the corresponding natural frequencies and can be directly compared to the experimentally measured spectrum. Different numerical methods can be used to solve the aforementioned problem [78, 79].

3.3 High Pressure Cells

This section gives a brief review of the high pressure techniques and focuses on two types of pressure cells: opposed anvil and piston cylinder. Both types were used in the project.

3.3.1 Opposed Anvil Type

The opposed anvil cells consist of two anvils, usually diamonds or sapphires, cut from gem stones with polished culets to form small flat faces. The anvils are brought together using appropriate platens which constitute the body of the cell. A metal gasket supports the sample mechanically and also provides space for a pressure medium. The opposed anvil cell setup can be used to conduct a very broad spectrum of measurements such as x-rays diffraction, optical spectroscopy, microscopy and transport measurements [80]. The main advantage of the opposed anvil cells is the huge range of available static pressure of up to 400 GPa with the conventional design and even higher with the nanocrystalline diamonds [81]. The main disadvantage of the technique is small sample space. This is especially troublesome when assembling the cell in experiments where the orientation of a single crystal is important such as transport measurements in high magnetic fields. The commercially available diamond anvil cells contain sample volumes of the order of 0.1 mm^3 [82], whereas the sapphire cells have sample space of the order of 1 mm^3 but are limited in pressure to around 15 GPa [83]. The opposed anvil cells are used in both low and high temperature experiments. A schematic diagram of an opposed diamond anvil cell is presented in Fig 3.4.

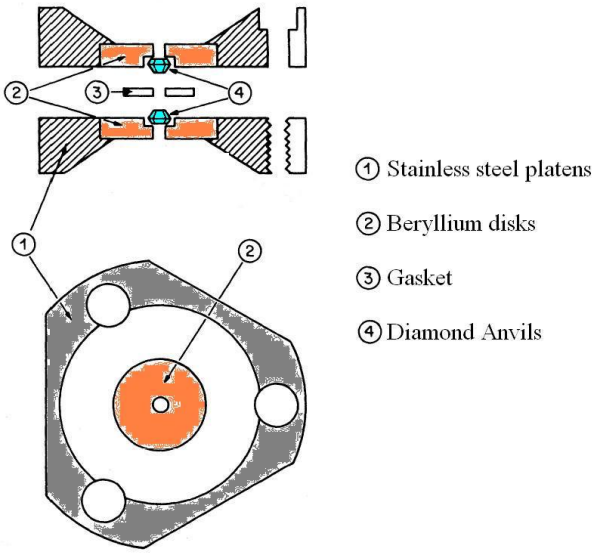

Figure 3.4: Schematic diagram of a diamond anvil cell. Adopted after [80].

The most commonly used method of pressure calibration is the ruby fluorescence spectroscopy. The method requires placing a chip of ruby in the pressure region. The fluorescence is induced by a laser source. The spectrum has two sharp and strong lines (R1 and R2 at 692.7 nm and 694.2 nm respectively) which shift as a function of pressure [80].

3.3.2 Piston Cylinder Type

The piston cylinder cells are designed to use a piston to pressurise samples through pressure transmitting medium. The body of the cell, usually of a shape of a long cylinder, provides the sample space but also guides and supports the piston, Fig 3.5. Pressure is increased by applying load using a press. The piston is then locked in place by locking nuts. The main technical challenge is to prevent leaks and contain the pressure medium inside the cell. This is achieved through the systems of seals which might include rubber or polytetrafluoroethylene (PTFE) o-rings and deformable copper washers. As for the sample space, the piston cylinder cell, compared to the opposed anvil one, offers much bigger volumes of the order of 100 mm^3 or more. However, they are more limited in the maximum obtainable pressure of 3-4 GPa [84]. The piston cylinder cells can be used for example for transport measurements at low and high temperatures as well as in neutron scattering experiments.

One way of measuring pressure in the piston cylinder cells is to monitor resistance of a calibrated manganin coil [85] which is mounted inside the cell next to a sample. In order to allow pressure calibration of the manganin sensor as well as transport measurements, the cell needs to be equipped with a plug to allow electrical connection to the sample and the manganin coil. The plug acts as a feedthrough for the wires but also provides sealing. As mentioned, the main advantage of the piston cylinder cells is greater sample space which allows for more options for complex measurements setups. Samples can but oriented, cut, polished and connected to electrical leads and then can be loaded in the cell.

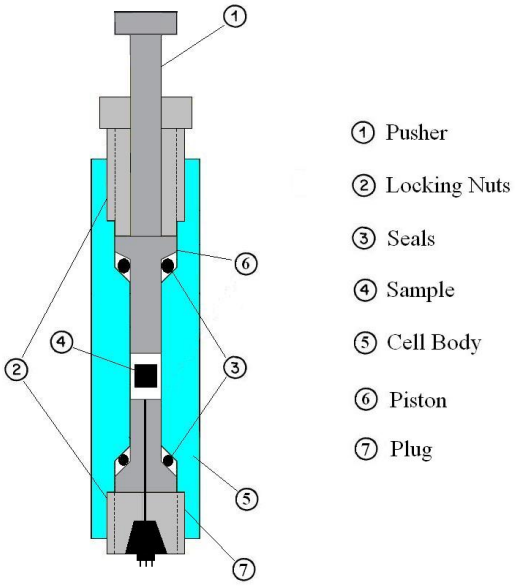

Figure 3.5: Schematic diagram of a piston cylinder cell equipped with a plug for transport measurements and manganin pressure calibration.

3.4 Review of Previous Ultrasonic Measurements at High Pressures

Ultrasonic measurements at high pressures were implemented using the Paris-Edinburgh press up to 6 GPa [86], the diamond anvil cel up to 10 GPa [87], the piston cylinder cell up to 2 GPa [88, 89] and also multi-anvil cell up to 7 GPa [90]. These experiments were performed mainly to study polycrystalline but also single crystal samples at high pressures and high temperatures relevant to geological investigations of the Earths mantle [91]. All of them also used the pulse echo technique and shared the same design principle whereby the piezoelectric transducer was installed outside the pressure region. In the case of bigger cells (the Paris-Edinburgh, the piston cylinder or the multi-anvil), the transducer could be attached directly to the anvil. In case of a diamond anvil cell, the transducer had to be attached to a buffer rod (a crystal of sapphire or yttrium aluminum), which itself was pressed into the back of the diamond anvil. The ultrasonic signal, therefore, had to be transmitted through the anvil and the buffer before reaching the sample. Examples of the above setups are shown in Figs 3.6, 3.7 and 3.8.

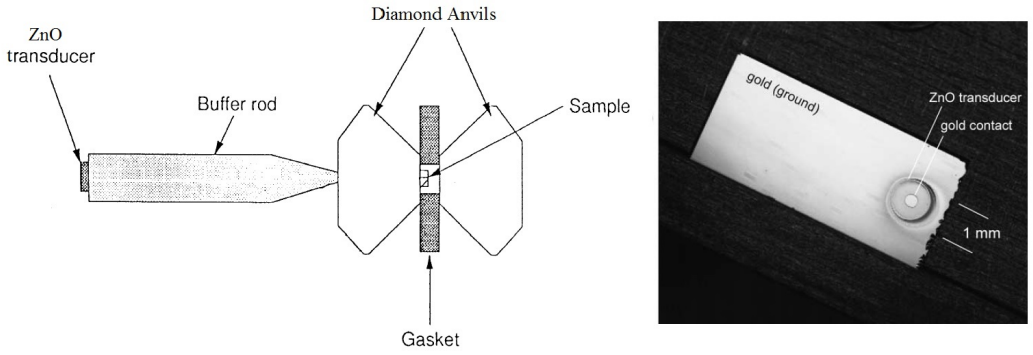

Figure 3.6: Schematic diagram of a diamond anvil cell setup for pulse echo measurements in GHz regime (left). The thin-film ZnO transducer (right) with gold contacts is chemically deposited directly onto the buffer rod. The ultrasonic signal is transmitted through the rod and the anvil before it reaches the sample. Adapted after [87] and [92].

As noted, the application of high pressures reduces sample space and this in turn dictates the frequency (or wavelength) of the ultrasonic signal. In a diamond anvil cell, the commercially available transducers cannot be applied. Instead, a thin-film transducer is chemically sputtered directly into the buffer rod. The 1.5 μm ZnO thin-film transducers can be driven at frequencies in the GHz regime [87, 92]. The rod itself is a single crystal with a specified orientation, what ensures that no unwanted interference between the ultrasonic signals takes place. The rod can be custom cut and can be used to select the polarisation of the ultrasonic wave. The resulting spectrum will contain the ultrasonic peaks due to the reflections from every interface in the setup: the buffer-anvil, the anvil-sample and the back end of the sample. It is therefore very important to know the exact dimension of each element of the setup and the sample in order to identify the peaks in the spectrum. For the Paris-Edinburgh cell, the piston cell or the multi-anvil cell, the choice of available frequencies is wider due to larger sample space allowing application of commercially available transducers such as quartz or lithium niobate crystals, but, as mentioned before, the dimensions of all elements must be measured accurately.

Finally, it should be noted that in the above setups the sample has to be in good mechanical contact with the anvil itself. This is in contrast with the typical high pressure experiment where the sample is kept away from the pressure transmitting parts in order to ensure fully hydrostatic conditions. The effect of

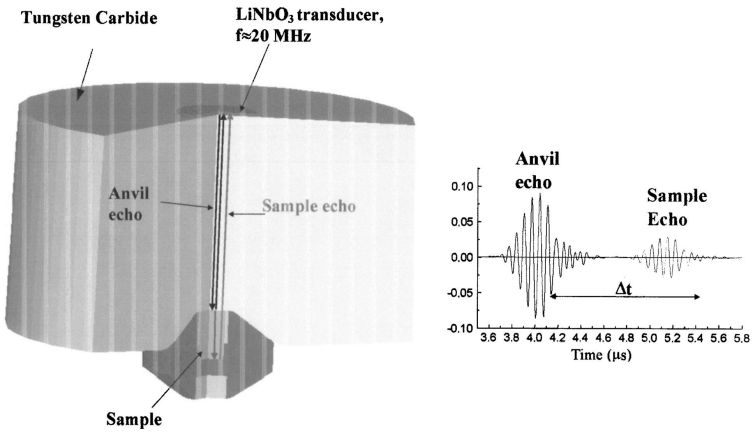

Figure 3.7: Schematic diagram of the anvil of the Paris-Edinburgh setup together with a test spectrum. The lithium niobate with a resonance frequency of 20 MHz is attached to the tungsten carbide anvil. Adopted after [86].

non-uniform pressure distributions is small in the Paris-Edinburgh press – for the cell similar to the one used in the ultrasonic studies [86], the pressure variation on the culet between the centre and the edge of the anvil is 5% when loaded to 7 GPa [83]. However, this issue might be more problematic when studying single crystal samples when taken to the limit of the pressure cell. There is also a risk that bridging of the sample will cause uniaxial stresses – especially critical when a sample of sufficient length has to be provided in order to fit the wavelength of the ultrasonic signal. To fully study hydrostacity of the pressure region, a finite element analysis (FEA) simulation for a specific cell used in an experiment, is required, taking into account the types of materials used, geometry of the anvil and the gasket.

3.5 Development of the In-house Setup

The instrumentation development, including two pressure cells for ultrasonic measurements, will be described in details in the next chapter. Here, it is worth emphasising the differences between the aforementioned techniques and the development of the in-house setup.

The techniques described above all used the same design principle whereby the source of the ultrasonic wave was placed outside the pressure cell. This will

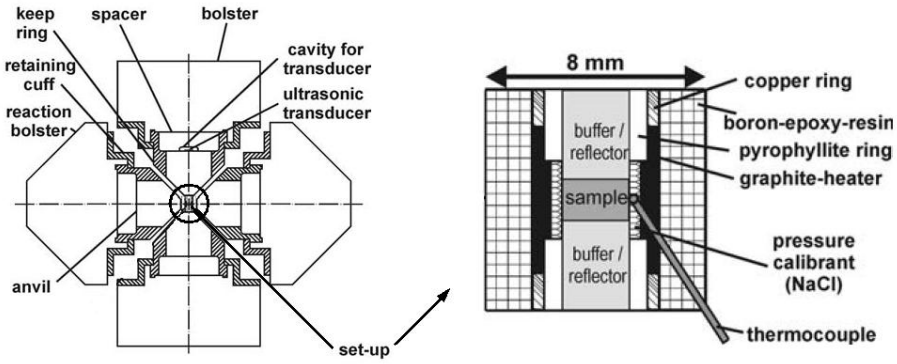

Figure 3.8: Schematic diagram of a multi-anvil cell pulse for echo measurements equipped with a thermocouple. Adopted after [90].

imply that measuring subtle effects in a single crystals sample, such as magnetic anisotropy, is very difficult. For example, exciting one particular mode of the sample would be very troublesome since ultrasound needs to be transmitted thought different parts and is subject to attenuation losses and interference effects. Such effects will contribute to the overall errors and make absolute measurements very problematic.

The first technique used in the project relies on the same principle. The transducer will be mounted outside the cell, directly on of the anvils. The novelty of the design comes from the fact that the resonant technique will be used in an opposed anvil cell. This will greatly extend the available pressure range which was previously very restricted.

The second technique used in the project presented here relies on a different principle. The pulse echo measurements will be done using a piston cylinder cell. However, the transducer will be mounted on a sample directly and both elements will be placed inside the pressure cell. Such a design eliminates the problems described above, but also allows for a response detection from very small samples.

Chapter 4

Instrumentation Development

As explained in the previous chapters, probing the phase diagram of UGe_2 requires application of several experimental techniques. Consequently, large part of the project was focused on instrumentation development. This chapter will present different instruments designed and developed during the project. The technical challenges together with the prototype testing will be discussed.

The following pieces of equipment were designed, developed and tested:

1. **2-axis Rotation Stage for High Pressures**
2. **Miniature Merrill-Bassett Diamond Anvil Cell**
3. **Variable Temperature Insert for Closed Cycle Cryostat**
4. **Ultrasonic Sapphire Anvil Cell**

4.1 2-axis Rotation Stage for High Pressures

This section describes the development of the 2-axis Rotation Stage for High Pressures.

4.1.1 Development of the 2-axis Rotator

The overall design of the 2-axis Rotation Stage for High Pressures is presented in Fig. 4.1. The principle idea was to accommodate the pressure cell as the integral part of the state itself.

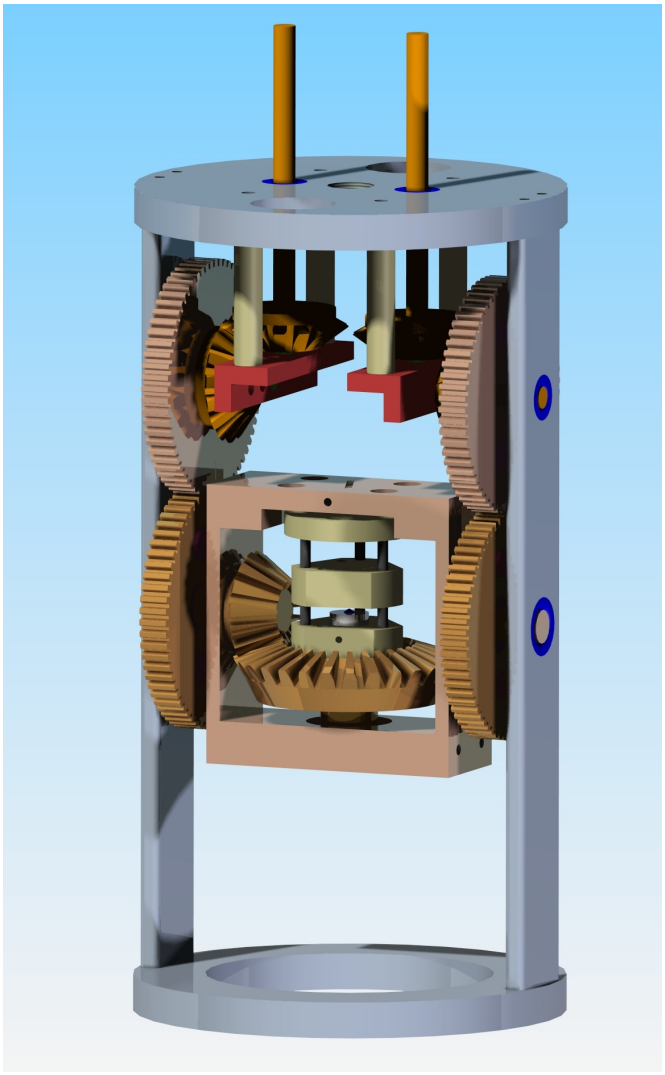

Figure 4.1: Rendered image of the 2-axis rotator together with the miniature diamond anvil cell. Description in the text.

The 2-axis rotator was developed to allow transport measurements on single crystal samples at pressures up to 5 GPa, temperatures down to 2 K and magnetic fields up to 9 T. The rotator was designed, so it could be used in the top loading *9 Tesla Solenoid Cryogen Free Superconducting Vector Magnet System* (CRYOGENIC LTD), which also required a development of a custom designed Variable Temperature Insert (VTI) and a special miniature diamond anvil cell (mDAC).

The goal was to achieve high precision *in situ* rotation (within 0.2 degree) of pressurised samples at cryogenic temperatures. The main technical challenges included: limited sample space, sufficient vacuum sealing, thermal leaks, requirement for a non-magnetic material used to machine different parts and necessity to avoid lubrication which would cease the gears at low temperatures.

Cryogenic probes with *in situ* sample rotation stages [93–97] or with micro-positioning stages [98] were previously developed. Some rotation and positioning stages are also commercially available [99–101]. However, none of the above offered the 2-axis rotation of samples at conditions described above.

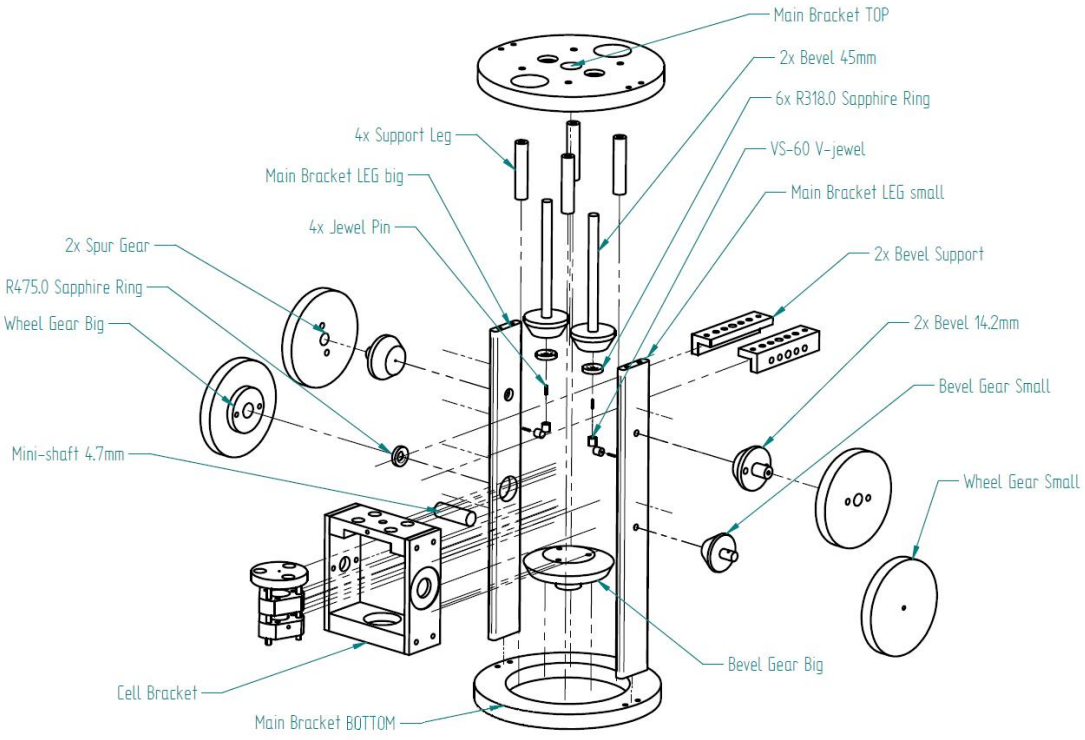

Figure 4.2: Exploded assembly of the 2-axis rotator. Description in the text.

The principle design idea was to make the miniature diamond anvil cell part of the rotating stage itself. Therefore, the guiding pins of the cell are engaged in the holes in the main bevel gear, Fig. 4.2. The engaged cell is placed inside the cell bracket allowing rotation with respect to the symmetry axis of the cell (rotation axis 2), Fig. 4.4. Rotation is provided by a driving shaft through a set of gears. The cell bracket is itself engaged to the main rotator bracket and can be rotated by another drive shaft through the second set of gears. Rotation of the cell bracket constitutes the second rotation axis (rotation axis 1), Fig. 4.4. The rotation axis 2 is not fixed and it can be rotated with the cell bracket, whereas the rotation axis 1 is fixed with respect to the main bracket. It should be noted that both rotation axes are coupled – this was intentional in order to simplify the mechanism and save the sample/pressure cell space. The coupling implies that the rotation through the axis 1 will cause the rotation through the axis 2. However, rotation of the axis 2 does not cause rotation of the axis 1, as explained the axis 1 is fixed. For example, a rotation of 30° about the axis 1, will cause a rotation of 15° about the axis 2, since there is a ratio of 2:1 between the bevel gears. The axis 2 will be tilted by 30°, but there will be additional rotation of 15° about the axis due to the axes coupling. The coupling of the axes can be easily resolved, the 15° can be compensated by rotating the axis 2 on its own by -15°, which will not change the 30° tilt of the axis.

The design of the 2-axis rotator allows for a full 360° about both axes. In practise though, this is unachievable due to a limited length of the wires used for transport measurements. On the other hand, the size of the main bracket is sufficient enough to easily accommodate few centimetres of wires. Care must be taken when arranging the wires in order to avoid their breaking or entanglement. The 2-axis rotator can be used with or without the pressure cell. A sample can be directly mounted to the bevel gear which serves as a sample rotation stage.

The rotating parts were mounted and engaged using the sapphire jewel bearings (SWISS JEWEL COMPANY) including sapphire rings, cups and pivots, Fig. 4.2. This reduces friction between the moving elements and eliminates the need to use lubrication. All parts of the 2-axis rotator were machined from copper-beryllium except the 3D-printed gears and the small stainless steel screws. The gears were printed in plastic at the School of Engineering, the University of Edinburgh. Originally the gears used for the rotator were made from phosphor

bronze (HPC GEARS). However, they had to be replaced due to inadequate quality which was causing imprecise and erratic rotation, Fig 4.3.

Finally, the rendered images of the 2-axis rotator were done not merely to present the final stage of the design process, but also to be employed by a computer program that controls the rotation (see section 4.1.4).

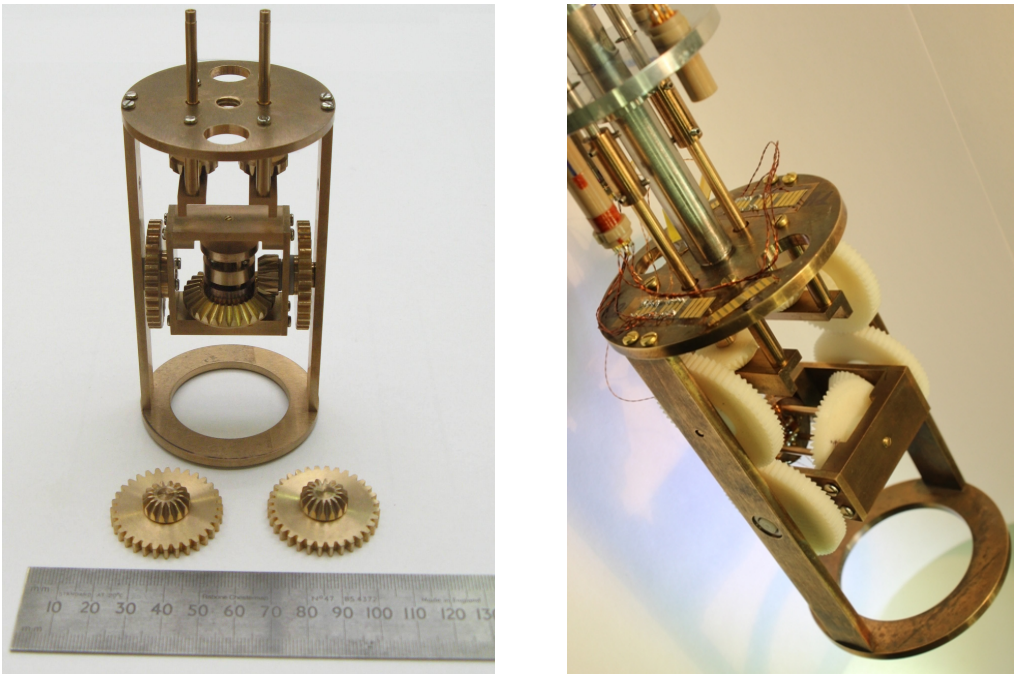

(a) (b)

Figure 4.3: **(a)** The prototype version of the 2-axis rotator with the set of phosphor bronze gears. **(b)** The 2-axis rotator with the 3D-printed gears mounted on the Variable Temperature Insert.

4.1.2 Development of the Miniature Merrill-Bassett Diamond Anvil Cell

As explained above, the mDAC is the integral part of the rotation state. Therefore, the cell had to be scaled down compared with the standard x-ray Merrill-Bassett cells [80], Fig. 4.6. The cell consists of two parts connected together by three cell pins, Fig 4.5. Each part, top and bottom incorporates support for the diamonds. The bottom part of the cell has a grove for the diamond support disk which allows aligning and centring of the diamond. The

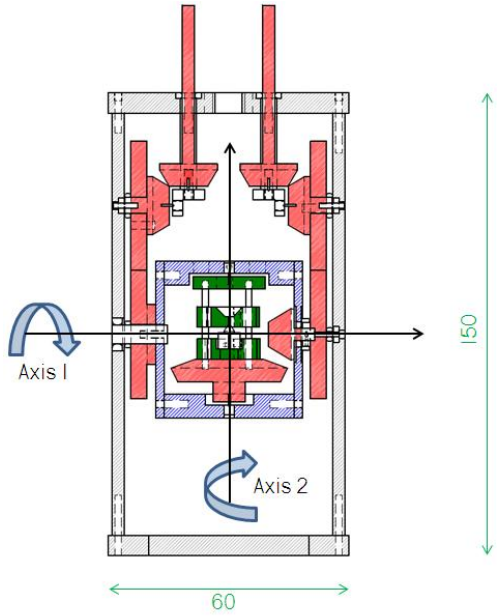

Figure 4.4: Cross-sectional view of the 2-axis rotator with the rotation axes indicated. All dimensions are in mm.

other diamond is glued directly to the top part of the cell. The diamonds are brought together using custom made screws, Fig 4.5 (a).

Two different types of the top part of the cell were made: one with a window with the 90° opening angle, Fig 4.6 (b), and one with an SMA connector, Fig 4.5 (a). The part with the SMS connector was developed to be employed with a fibre optic system with the other probe for the same cryostat.

The mDAC allows for application of any diamonds with flat back sides. As for the gasket, several options are available that include stainless steel, copper, copper-beryllium or tungsten. The diamonds used is this development had culet sizes of 800 μm.

4.1.3 Development of the Variable Temperature Insert (VTI)

The driving mechanism, consisting of two stepper motors (MCLENNAN SERVO SUPPLIES), is placed outside the cryostat on the top part of the VTI, as shown in Fig. 4.8 and 4.9 (b). Torque is provided to the 2-axis rotator through two long stainless steel (Grade 316) drive shafts, each 3 mm in diameter. The shafts are connected directly to two bevel gears which belong to the main bracket assembly

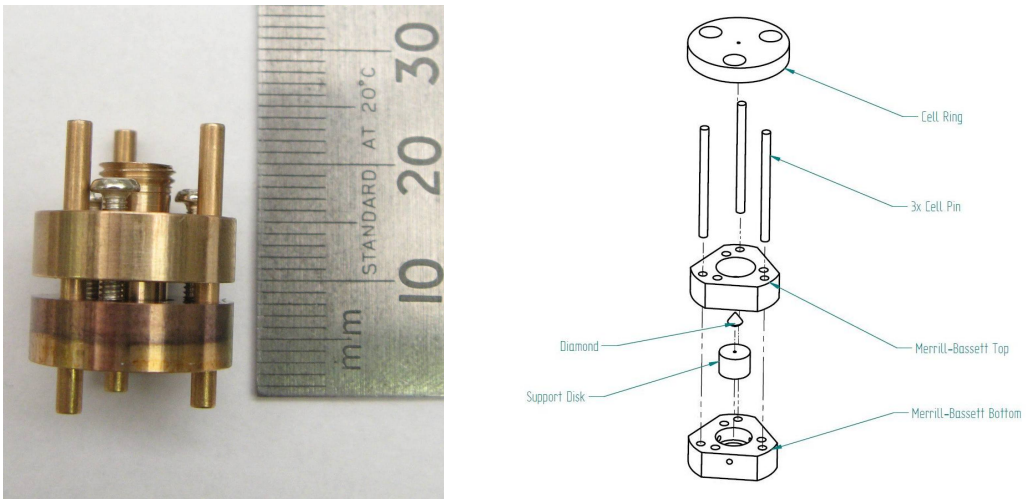

(a) (b)

Figure 4.5: **(a)** The miniature Merrill-Bassett diamond anvil cell developed for the 2-axis rotator. **(b)** Exploded view of the cell. The cell pins are used to engage the cell into the rotation state.

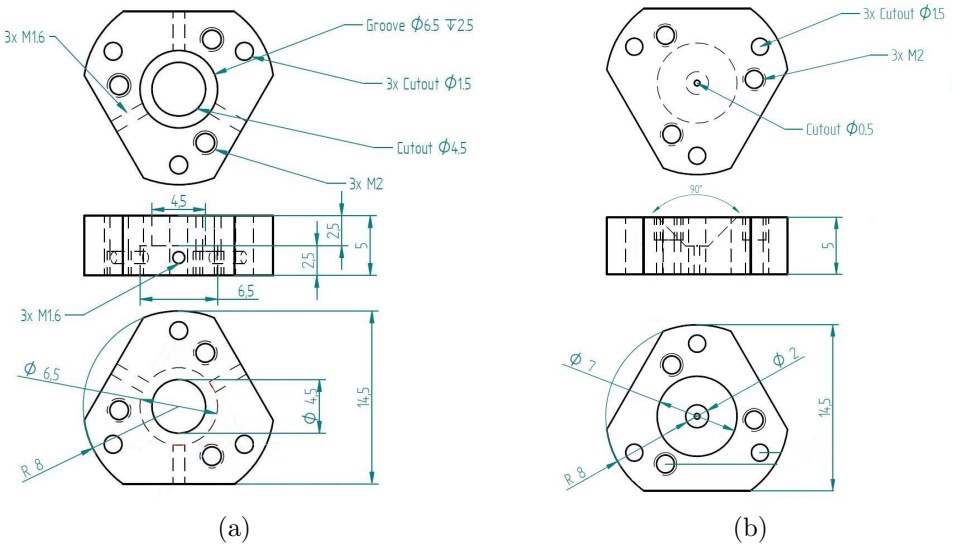

(a) (b)

Figure 4.6: **(a)** The bottom part of the mDAC. The part has a groove for the support disk allowing diamond alignment with three grab screws. **(b)** The top part of the mDAC. The part has an opening angle of 90° for an easy access for ruby fluorescence or other optical measurements.

(Figs. 4.1-4). The connection is achieved via a connecting sleeve with grab screws (Fig. 4.3 (b) and 4.7). The drive shafts are placed inside the main tube which supports the 2-axis rotator as well as the stepper motors and constitutes the body of the VTI. The tube is made from stainless steel (Grade 316) and

has a diameter of 28.57 mm and wall thickness of 0.92 mm. The dimensions of the tube were chosen to reduce thermal leaks. Each drive shaft is fixed to the tube via an adjustable feedthrough cap containing three o-rings which provide rotational vacuum sealing down to 10^{-6} mbar as well as one sapphire ring that reduces friction and provides mechanical support.

In order for the VTI to be loaded into the cryostat, a custom vacuum airlock was developed. The airlock can be attached to the top of the cryostat, Fig. 4.9 (b). It provides vacuum sealing and mechanical support when the VTI is being loaded. The vacuum sealing is provided through two rubber o-rings and a PTFE washer with adjustable tightening mechanism that allows changing the give between the airlock and the VTI. The tightening mechanism controls the tightness of sliding of the VTI through the airlock. The airlock can be continually pumped on during loading of the VTI and can provide vacuum sealing down to 10^{-6} mbar. It should be noted that both motors can be removed before unloading the probe in order to reduce the mass of the VTI and make the unloading easier.

The head of the VTI contains two Fischer connectors. The 24-pin connector is used to accommodate 12 twisted pairs and can be used for any transport measurements. The 6-pin connector, also utilising the twisted pairs, is used to connect a thermometer with the Lakeshore Cryogenic Temperature Controller (four connections are used for the thermometer specifically and the two remaining can be used with an optional heater). The twisted pair are hand-made from an insulated 100 μm thick copper wire. All thirty connections are distributed between the four plugs mounted on the supporting plate just above the 2-axis rotator, Fig. 4.3 (b) and 4.7. Each plug is connected to its own break-out pad with individual copper contacts which are used to solder the wires attached to a sample or the pressure cell. The pads layout was chosen for an easy operation by a user.

4.1.4 Angle Measurement and Operating System

The 2-axis rotator is controlled through a program developed in LabVIEW in collaboration with William Whitley. A computer is connected to the stepper motors through a control box which includes the power supply for the motors.

The program utilises the rendered image of the 2-axis rotator which was developed in the Solid Edge. The image helps user to understand and follow

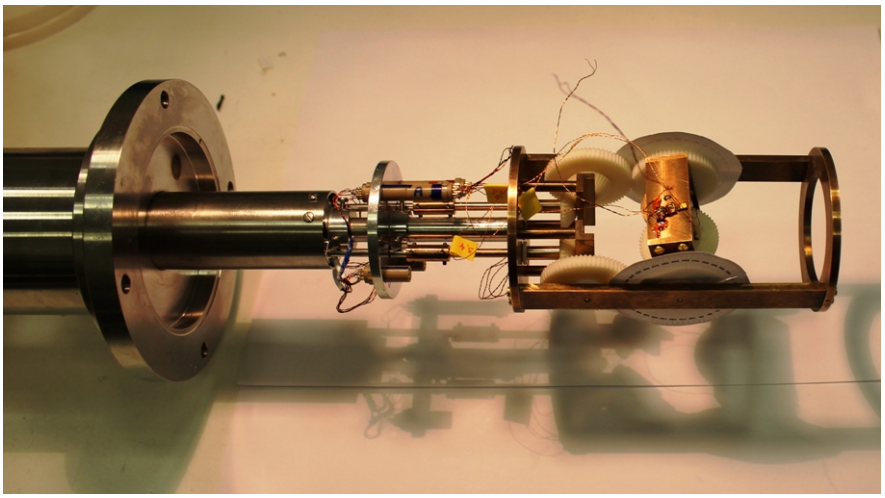

Figure 4.7: The 2-axis rotator mounted on the Variable Temperature Insert. The small bevel gears are directly attached to the driving shafts using connecting sleeves with three grab screws. 15 twisted pairs are distributed among four plugs mounted on aluminium support plate.

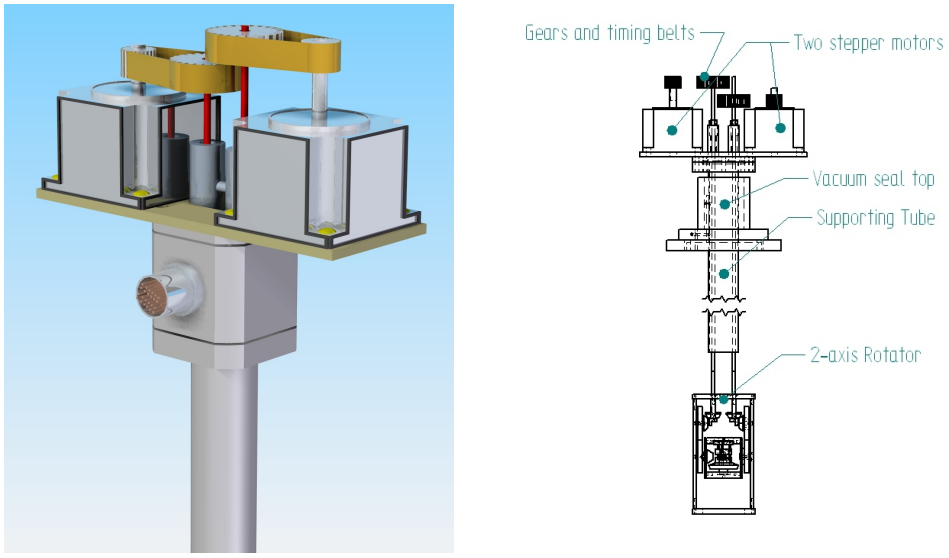

(a) (b)

Figure 4.8: **(a)** Rendered image of the top of the Variable Temperature Insert (VTI). **(b)** A cross-sectional view of the VTI with the 2-axis rotator.

the orientation in terms of the current position of the mDAC, Fig. 4.9 (a). An input from the user causes the image to follow the actual rotation inside the cryostat.

The two axes have their own angle calibration. For the axis 1, one step in the program corresponds to a rotation of 0.6°. For the axis 2, one step in the program

corresponds to a rotation of 0.4°. The angle calibration was done carefully at room temperature outside the cryostat with the aid of a micro-protractor.

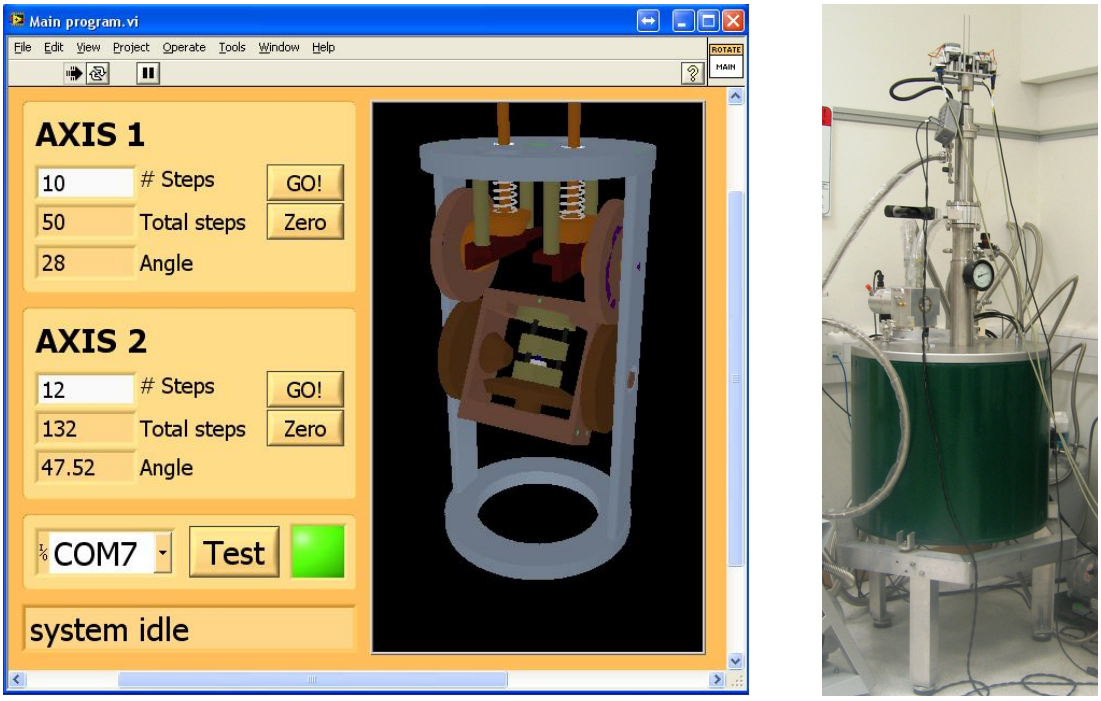

(a) (b)

Figure 4.9: **(a)** Print-screen of the 2-axis rotator software. **(b)** The VTI with the 2-axis rotator loaded into the cryostat.

The backlash was determined to be 16 steps (5.7°) in terms of axis 2 and 7 steps (3.9°) in terms of axis 1 at room temperature.

The 2-axis Rotation Stage was tested at low temperatures (2 K) without the pressure cell. The precision of the rotation was determined to be within 0.5 degree.

4.1.5 Further Work and Future Outlooks

The high pressure measurements were not taken due to delays in the 2-axis development caused by the cold-welding of the stainless steel drive shaft with the vacuum feedthrough which turned out to be too tight. Furthermore, the quality of the phosphor bronze gears was inadequate causing a backlash to exceed 10° and also a lack of uniformity in shape. This was causing an increase of friction between the gears and an extra torque load on the stepper motors causing overheating. It was therefore necessary to switch to 3D printed gears.

The future work includes:

1. **Rotation and measurements at high pressures.**

   A single crystal of UGe_2 is already selected and spot-welded with four 10 μm gold wires. A copper-beryllium gasket with hole of 300 μm was insulated with a mixture of GE varnish and aluminium oxide power to prevent shorting of the gold wires. The crystal needs to be oriented and loaded into the cell.

2. **Installation of the Hall sensors and new angle calibration.**

   In order to receive a feedback from the 2-axis rotator when it is loaded into the cryostat, the Hall sensors need to be mounted on different parts of the rotator. One needs to be attached to the cell bracket which will send the feedback from the rotation axis 1. The other one can be attached to the pressure cell itself of the main bevel gear, so it can send the signal from the rotation axis 2.

3. **Automatic backlash compensation.**

   The backlash was measured only at room temperature and it was assumed that it will not change at low temperatures. This is unlikely to be the case and the backlash has to be measured using the Hall sensors. The backlash is likely to be temperature dependent due to several materials used to construct the rotator, each with their own different thermal expansion. Once the low temperature backlash is known, the program can be changed to take it into account and compensate for it automatically.

4. **Rotation and ultrasound.**

   The 2-axis rotator can be used in any transport measurements, but it is also possible to use it for ultrasonic studies. Of course, the direction of sound propagation will be fixed with respect to a sample, but rotation in field is possible. Ultrasonic measurements at ambient pressure can be made with the transducers used in the project and described in Chapter 3. However, for high pressure ultrasonic measurements using the mDAC, a thin-film transducer set-up (described in section 3.4) would be required.

4.2 Development of the Ultrasonic Sapphire Anvil Cell

The Ultrasonic Sapphire Anvil Cell was developed for high pressure ultrasound measurements using the resonant technique at cryogenics temperatures.

4.2.1 Design overview

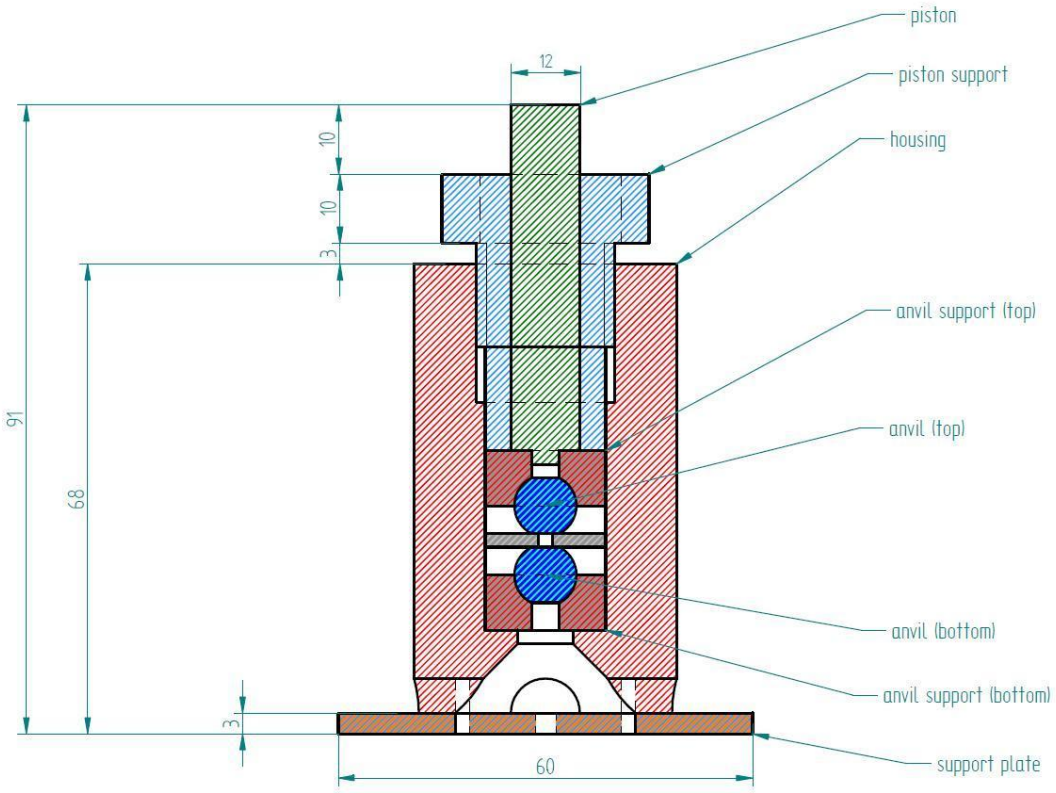

Figure 4.10: Simplified cross-sectional view of the Ultrasonic Sapphire Anvil Cell. Both spherical (shown here) and cylindrical sapphire anvils can be used. The cell can be used in the *9 Tesla Solenoid Cryogen Free Superconducting Vector Magnet System*. All dimensions in mm.

The Ultrasonic Sapphire Anvil Cell, Fig. 4.10, is designed according to the standard principles of an opposed anvil type cell. The cell was designed so it could use spherical as well as cylindrical sapphire anvils. The spherical anvils allowed for a custom orientation of the sapphire crystal, whereas the cylindrical anvils were oriented with their symmetry axis along the crystallographic c-axis of

the sapphire crystal. This choice was offered, so experiments in which a particular polarisation of the ultrasonic wave is required and it would not be disturbed by the anvil.

Both anvils are held in place by copper-beryllium supports with spherical or cylindrical shape, accordingly. No centring mechanism for the anvils is required due to a good fit between the main body of the cell and the anvil supports, Fig. 4.10 and 4.11. Similarly, parallelism between culets is provided by precision machining of the anvil supports. The cell body was made from copper-beryllium.

Pressure can be increased by applying load to the stainless steel piston using a hydraulic press. The piston has a small protrusion, Fig 4.10, so it could be engaged with the anvil support. The piston is guided by the piston support/locking nut which is also used to lock the anvils at high pressures, Fig. 4.10 and 4.12 (a). The cell can be mounted onto the support plate which is used to fix the cell to the low temperature probe of the *9 Tesla Solenoid Cryogen Free Superconducting Vector Magnet System*, Fig. 4.12 (b).

The probe used to load the cell into the cryostat has two fibre optic cables allowing for ruby fluorescence measurements. However, in order to obtain a good quality signal a development of an optical system was necessary, Fig. 4.11. The optical system consists of a collimator and a focusing lens. The collimator has a housing with an SMA adaptor which can be attached to the probe's fibre optic cable ended with SMA connector. The lens is placed between the anvil and the collimator and its position can be regulated by aluminium support ring so the laser beam can be focused on the culet of the top anvil where a ruby chip is placed. Both, the lens and the collimator are placed in the aluminium thin wall housing. The housing can be inserted in the space for the piston once the pressure is applied and piston removed, Fig. 4.11. The optical system allows for the pressure measurement as a function of temperature.

One of the most important aspects of the design was the culet and gasket optimisation. As explained in Chapter 3, in order to resolve an ultrasonic signal, the studied sample must be of a sufficient length (for pulse echo technique) or sufficient volume (for resonant technique). Therefore, the culet diameter and gasket thickness have to be of sufficient dimensions. This is where the design differs from the typical anvil type cell in which thin gaskets are used. The typical

culets tested were between 2-4 mm in diameter. The sphere anvils had a diameter of 8 mm and the cylindrical anvils were 10 mm long and 12 mm in diameter. The thickness of the gaskets was ranging between 1.5-4 mm. The goal was to achieve 2 GPa with the highest possible volume space. A concise summary of pressure cell tests is presented in the next section.

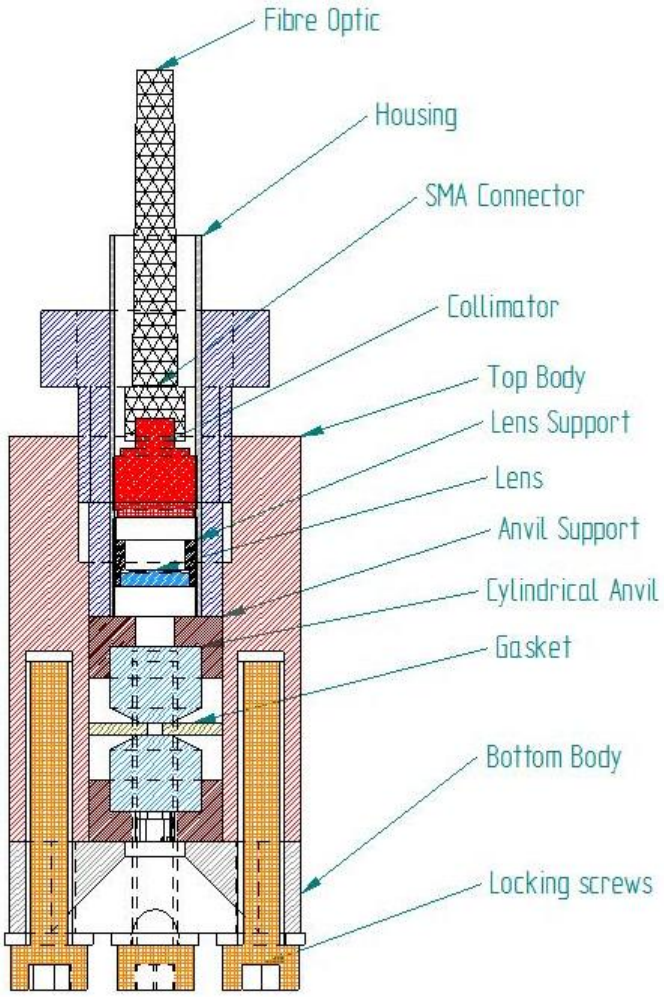

Figure 4.11: Detailed cross-sectional view of the sapphire anvil cell with the optical system for the ruby fluorescence calibration.

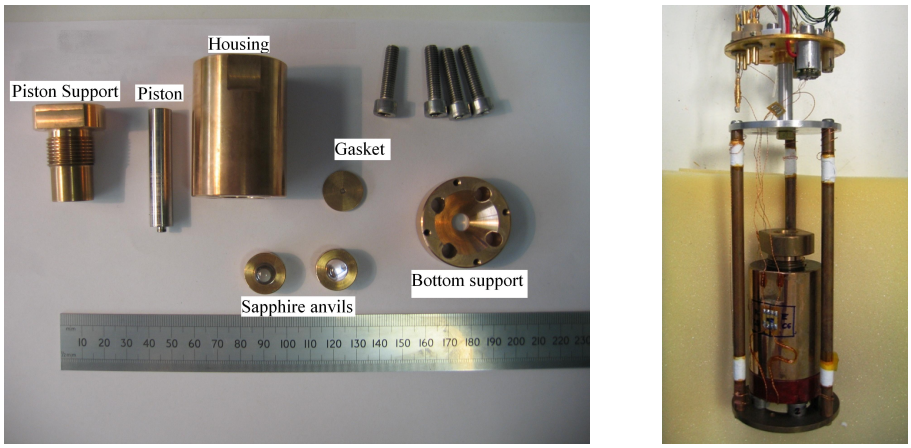

(a) (b)

Figure 4.12: **(a)** Disassembled sapphire pressure cell. **(b)** The cell mounted on the probe with the wiring for the two transducers.

4.2.2 High Pressure Tests

The tests were conducted with no sample and only powdered NaCl was loaded into the sapphire anvil cell. NaCl was chosen to be the pressure medium for the sapphire anvil cell due to its easy application and pressures not exceeding 2 GPa. All anvils were prepared and polished by the author using the stone wheel polishers and diamond paste.

Test 1:

The first set of tests was done using sapphire cylinders which were c-axis oriented by the manufacturer (AGATE PRODUCTS LTD). The cylinders were polished to have culets with the diameter of 4 mm and had the taper angle of 16°. The anvils were annealed at 1450 °C for 72 hours in order to reduce internal stresses.

As for the gaskets, they were disks machined from copper-beryllium with overall diameter of 10 mm. The gaskets had sample hole of 1 mm in diameter and were pre-indented before the pressure tests from 1.8 mm to ≈900 μm using tungsten carbide anvils with the same culet size.

The maximum pressures obtained with the above setup, before the anvil failure, was 0.7 GPa. The anvil failures were usually shear cracks but also included chipping of the culet edge. An example of a shear crack in a cylindrical anvil taken to 0.7 GPa is shown in Fig. 4.14. Interestingly, the pressure cell was holding

pressure even when the shear cracks took place. The gasket had the thickness of ≈600 μm and the gasket hole expanded to ≈1200 μm when taken to sample pressures of 0.5-0.7 GPa. Therefore, it is possible to use the above setup for a cylindrical sample with a diameter of 1000 μm and a thickness of 500 μm.

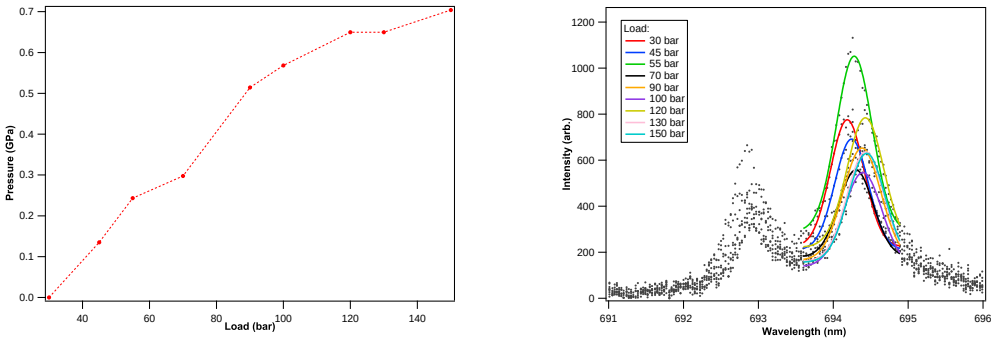

(a) (b)

Figure 4.13: **(a)** Example of a loading curve for a cylindrical anvil with a culet size of 4 mm. A hydraulic press was used to increase load on the piston. **(b)** Ruby fluorescence spectra corresponding to the loading curve.

As explained in Chapter 3, the sample shape is important when using the ultrasound resonant technique and the cylindrical shape of the sample would be advantageous. The size of the sample would require frequencies of the order of a few MHz easily achievable with the transducers used in the project (described in sections 3.2 and 4.2). On the other hand, the maximum pressure obtained was not sufficient to reach the interesting regions of the phase diagram of UGe_2. Therefore, it was decided to change the parameters of the gaskets and the anvils.

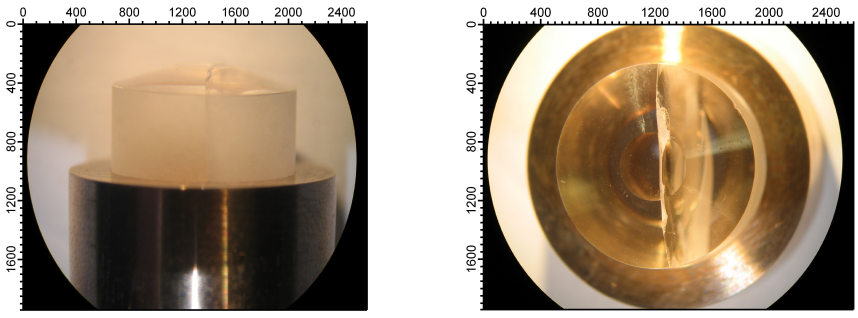

(a) (b)

Figure 4.14: **(a)** The sapphire anvil with 4 mm culet and 16° taper angle with a shear crack when taken to 0.7 GPa. 400 units on the scale correspond to 3.55 mm. **(b)** The top view of the cracked anvil.

Test 2:

The second set of tests was performed using sapphire spheres. The spheres were c-axis oriented by the back-reflection Laue x-ray method. An example of a Laue scan is shown in Fig. 4.16 (c). After the anvil orientation, the spheres were glued to the copper-beryllium anvil supports using araldite epoxy, Fig 4.16 (a). Then, they were polished to have culets with a diameter of 3.2 mm (0.8 mm smaller compared to Tests 1) and a taper angle of 30° (almost twice bigger compared again to Tests 1). The orientation of each anvil was checked after polishing. This time, the anvils were not annealed.

The gaskets, as described previously, were disks machined from copper-beryllium with overall diameter of 10 mm. Again, the sample hole had a diameter of 1 mm. The gaskets were pre-indented before the pressure tests to ≈650 μm from 1.8 mm using tungsten carbide anvils.

The maximum pressure achieved with the above setup was 2 GPa without anvil failure. The failures, such as those presented in Fig. 4.16 (a) and (b), usually took place when unloading the cell on the pressure release. The gasket had thickness of ≈450 μm and the gasket hole contracted to ≈ 850 μm when taken to pressure of 2 GPa. Pressure achieved with the above setup were sufficient to access the important regions of the phase diagram of UGe_2. As expected, the sample space was reduced to ≈800×400 μm (diameter × height), assuming again a cylindrical shape of a sample. This reduction implies that frequencies of ultrasound of the order of 10 MHz need to be used.

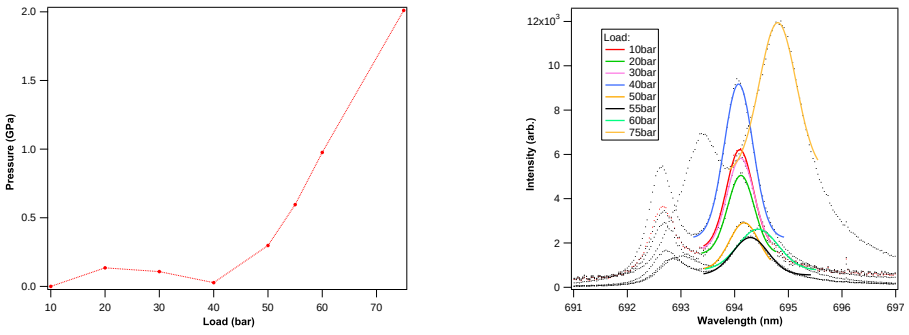

(a) (b)

Figure 4.15: **(a)** Example of a loading curve for a spherical anvil with a culet size of 3.2 mm. A hydraulic press was used to increase load on the piston. **(b)** Ruby fluorescence spectra corresponding to the loading curve.

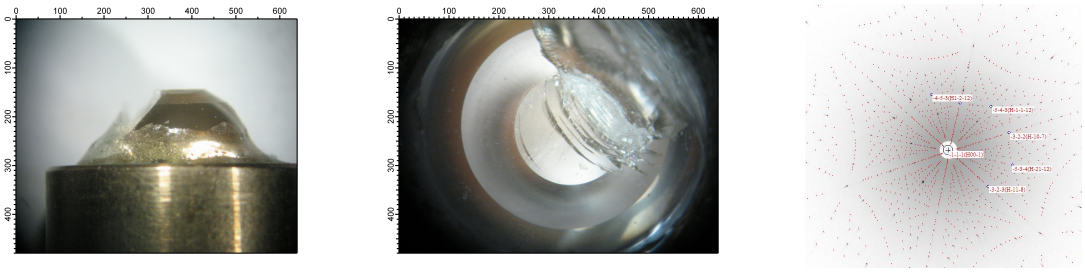

(a) (b) (c)

Figure 4.16: **(a)** The sapphire anvil with 3.2 mm culet and 30° taper angle after being taken to 0.7 GPa. The anvil failure took place on pressure release. 100 units on the scale correspond to 1.45 mm. **(b)** The top view of the cracked anvil. **(c)** Laue scan of the c-axis oriented anvil. The axis alignment was within 0.5°.

4.2.3 The Resonant Technique in the Sapphire Anvil Cell

The Sapphire Anvil Cell described above was used together with the resonant ultrasound method. Two PZT transducers were used, one as an emitter and one as a receiver. Both transducers were glued to the anvil with cyanoacrylate using a clamp vice, Fig. 4.18. The transducers, top and bottom coated with chrome-gold electrodes, had to be connected with the wavegenerator and the oscilloscope. The connection was provided by grounding the transducers with 10 μm gold wires, Fig. 4.17, which were then connected with thicker copper wires and to the coax cables of the cryostat probe.

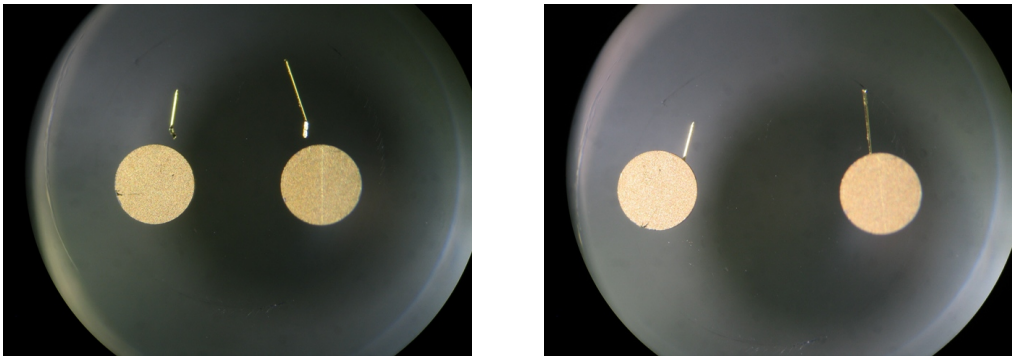

(a) (b)

Figure 4.17: **(a)** PZT transducers placed on the back of the sapphire anvil. Two 10 μm gold wires are used to ground the transducers. The transducers are top and bottom chrome-gold coated constituting the two electrodes. **(b)** The gold wires need to be flattened and then inserted under the transducer for electrical connection.

A sample used for test measurements was a single crystal of UGe_2 of a

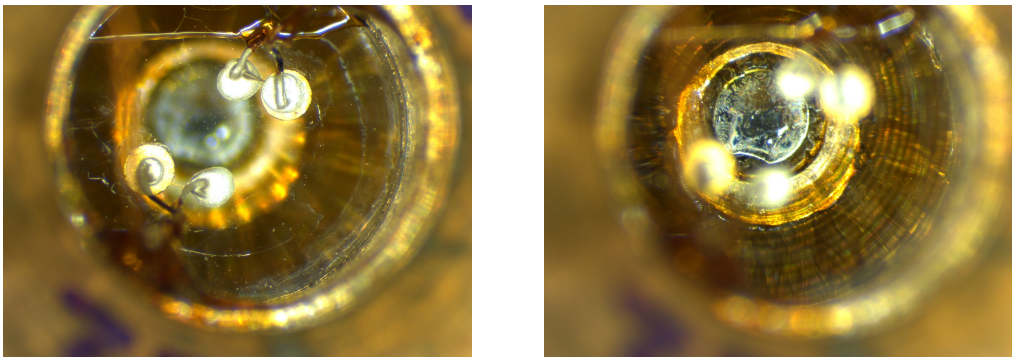

(a) (b)

Figure 4.18: **(a)** Two transducers glued and wired to the back of the anvil. One transducer acts as an emitter, the other as a receiver. The anvil provides pressure but also is used to transmit the ultrasound. **(b)** Cylindrical sample of UGe_2 loaded into the cell.

cylindrical shape with the diameter of 900 μm and length of 500 μm, oriented with a-axis parallel to the symmetry axis. The sample was loaded into the pressure cell but no pressure was applied during the test. The anvil was a cylindrical sapphire with a culet size of 3.2 mm and 30°. The gasket was copper-beryllium with a 1 mm hole and was 1.5 mm thick. The gasket was not indented.

Before data collection, test measurements of the above setup were performed on the c-axis oriented sapphire anvil. With the known dimensions of the sapphire anvil, the longitudinal speed along c-axis was estimated to be 1100±100 m/s which is in a very good agreement of known value [102].

As for data collection, two channels on the oscilloscope were used. Channel 1 was used to detect the signal coming from the wavegenerator (built-in into the oscilloscope) and going to the emitter transducer. The driving signal was a sine function with the driving peak-to-peak amplitude of 5 V. Channel 2 was used to detect the signal from the receiver transducer. Before starting frequency sweeps, the mechanical connection between the transducers and the anvil was verified by sending a pulse from one transducer to the other one. This method allows also for a careful measurement of the distance between the transducers since the speed of sound in sapphire is known.

The measurements were taken using a sequence written using LabView program which was controlling the oscilloscope settings. The measurements consisted of frequency sweeps of the driving sine function at different temperatures. The frequency step was 1000 Hz, over the range from 1.5 MHz to 2.8 MHz. The cell was

cooled down and was kept at a given temperature, where 3 frequency sweeps were taken to check the reproducibility of the spectrum, but also to reduce any random errors. Additionally, the oscilloscope was set to average acquisition mode which was the running average over 128 acquisitions. Resonant spectra were taken at many different temperatures. However, for clarity, the test measurements presented in Fig. 4.19 contain the data collected at four temperatures. The amplitude of the resulting peaks, Fig. 4.19, was obtained by taking the root mean square of the result of the peak-to-peak amplitude multiplication of Channel 1 and Channel 2. By taking the product, it was ensured that the in-phase signal was measured, i.e. the set-up was in the lock-in mode, further reducing the random noise.

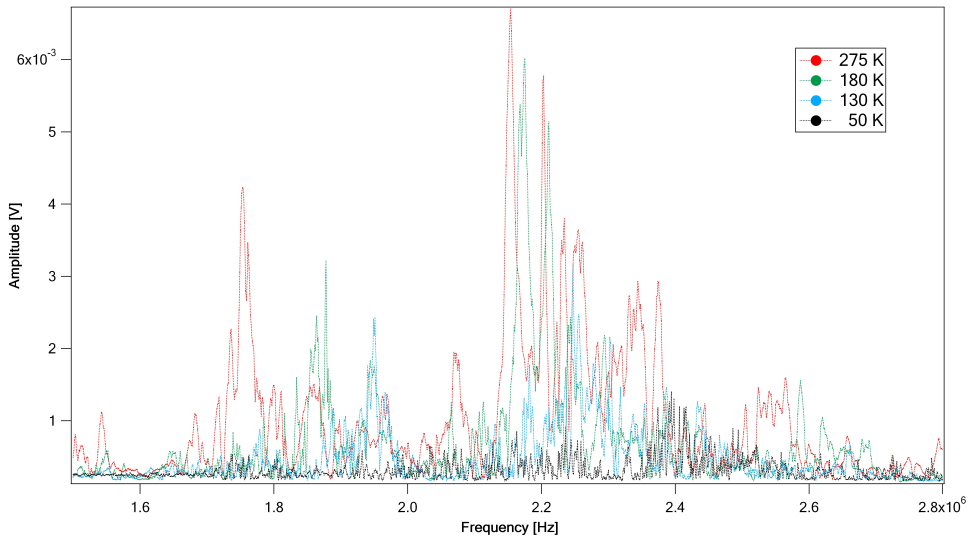

Figure 4.19: Resonant spectrum of the pressure cell loaded with UGe_2 sample. No pressure was applied.

The resonant spectra are complicated and require careful computer simulations for the peak identification. On the other hand, it can be clearly seen from Fig. 4.19 that the peaks are relatively broad as compared with a typical RUS spectrum. The broadening is very likely to be due to the dissipation of ultrasound from different parts of the setup (anvil, gasket, cell body) and the phase boundaries between these parts. The intensity of the peaks clearly decreases with temperature – this effect is not fully understood and might be caused due to several reasons such as diminished performance of the transducer at low temperatures (see also section 6.4.3) but also due to temperature effect on

bonding between the transducer and the anvil. The sapphire face was polished to optical quality and it is likely that at low temperature the bonding was failing. More work is required to study these effects.

Further complications concerning the resonant method originating in the application of the pressure cell are discussed in the next section. The comparison between the resonant ultrasound spectroscopy and high pressure resonant method is also presented.

4.2.4 Complications of the Resonant Technique under High Pressure

The above resonant method differs in two crucial aspects compared to the resonant ultrasound spectroscopy (RUS) explained in section 3.2. The first one is the coupling between a sample and transducers. In RUS, a sample is loosely clamped between two transducers, so all elements are in direct contact. In the pressure cell, transducers are not in direct contact with the sample. Ultrasound is being propagated through one of the anvils before reaching the sample. The sample itself should be in contact with the anvil in order to avoid effect coming from the pressure-transmitting medium. The second difference concerns the boundary conditions. In RUS, a sample is subject to free boundary conditions and sample's edges are free to vibrate. In the pressure cell this is no longer the case since one side of the sample is attached to the sapphire anvil and all other sides are surrounded by the pressure medium. The change of the boundary conditions to hydrostatic conditions will result in changes in the resonant modes which are not fully identified [103].

Previously reported RUS studies under pressure are limited to 1 kbar [104]. The studies were done on a steel sphere and the pressure was induced by helium gas. The steel sphere was placed in a spherical cavity and then inserted into the pressure vessel. Transducers were fixed directly to the sample. The peaks in the spectrum were identified by treating the problem as the free oscillation of three-layered structure superimposed on the static compression [104]. Therefore, the boundary conditions were still considered to be free and, furthermore, the geometry was taken to be completely spherical despite the fact that the pressure vessel had cylindrical shape.

In other pressure work, limited to even lower pressure of 100 bar, a rectangular

parallelepiped sample of fused silica was studied [105]. To solve the resonance problem, a two-dimensional model for a bar with a response similar to a vibrating piston mounted in an infinite baffle was used [105]. The problem of non-free boundary conditions was also considered to implement RUS on a cantilever [106]. The implemented model considered a zero displacement boundary condition at one end of the sample [106]. The model was validated by comparing calculated resonant frequencies to a limiting case involving a long and thin sample [106].

Finally, there is a complication coming from the position of the transducer and the size of the sample. Fig. 4.20 presents theoretical resonant spectra of a generic soft rock sample of different sizes and with different transducers arrangements [107]. The first two top plots in Fig. 4.20 show a sample, which can fall under long bar approximation, with transducers being attached to the corners and to the sides of the sample respectively. As expected, the sample which is clamped by its sides produces fewer peaks compared to the sample clamped by its corners. The spectrum gets more complicated when the sample width is two and four times greater as shown in two bottom plots respectively, Fig. 4.20. This is where, a long bar approximation cannot be applied. It should be noted that the spectra were obtained using free boundary conditions.

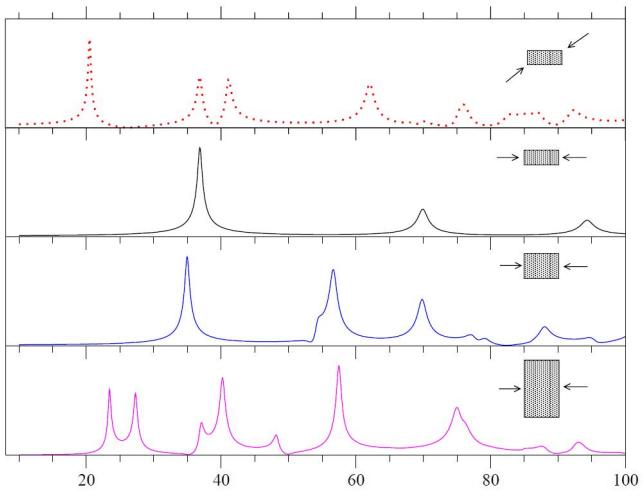

Figure 4.20: The influence of the position of the transducers and the sample size on the resonant spectrum. Vertical axis is the amplitude in arbitrary units and horizontal has units of kHz. Adopted after [107].

4.2.5 Further Work and Future Outlooks

The fully operating pressure cell at cryogenic temperatures with *in situ* ruby fluorescence system was developed. Hence, it was demonstrated that experimental measurements of the resonant spectrum in a pressure cell at cryogenic conditions are conceivable. Data collection and noise reduction was also implemented and optimised. Furthermore, the cell can be used without any modification with different anvils allowing applications of even higher pressures. Obviously, sample space reduction would need to be taken into account when setting up the electronics for the resonant measurements. The main remaining task is to fully analyse and identify the peaks in the complicated measured spectra. In order to achieve that, careful computer simulations are necessary. Unfortunately, due to time constraints and technical challenges concerning the development of the technique, this goal had not yet been achieved.

The list of problems that have to be taken into account for the simulation of resonant spectra include:

1. **Non-free boundary conditions.**

   This remains the central problem of the resonant technique under high pressure.

2. **Non-trivial geometry of the setup.**

   A simplifying factor here would be the fact that the setup exhibits a cylindrical symmetry of all elements including the sample, anvils, gasket and anvil support.

3. **Influence of the pressure medium.**

   Depending on the type of pressure medium (e.g. powdered NaCl, methanol-ethanol mixture, argon), the friction between a sample and the medium might be different which would influence the damping for the oscillations of the sample.

4. **Influence of the phase boundaries.**

   There are several phase boundaries in the setup: transducer-anvil, anvil-sample, sample-gasket, anvil-anvil support. It can be assumed that all

elements are in a very good mechanical contact due to application of high pressure. Nonetheless, each phase will be a source of ultrasonic attenuation and might influence the resonant spectrum.

5. **Effect of pressure application.**

   Pressure application on the setup elements will most inevitably have an influence on the measured spectrum. This is a further complication for the computer simulations. The effect of pressure will be most pronounced for the resonant peaks corresponding to the anvil since the anvil is subject to the highest pressure gradient within the setup (with the culet of the anvil being at maximum pressure and the back of the anvil being at ambient pressure).

Chapter 5

Inelastic Neutron Scattering under High Pressure

This chapter focuses on the inelastic neutron scattering experiment under pressure and was performed to study the longitudinal magnetic fluctuations (moment fluctuations along its direction) in UGe_2. The chapter starts with a brief introduction to neutron scattering using triple axis spectrometry. The comparison discussion between ambient and high pressure data is presented.

5.1 Introduction to Triple-Axis Spectrometry

Neutrons, being electrostatically neutral, can penetrate deeply into the sample and scatter from nuclei which makes them an ideal probe to study condensed matter [108]. On the other hand, they exhibit a magnetic moment and therefore can interact with electrons.

In a scattering event, the energy and momentum conservation require

$$\hbar\omega = E_i - E_f \tag{5.1}$$

$$|\mathbf{Q}| = k_i^2 + k_f^2 - 2k_i k_f \cos\theta_S \tag{5.2}$$

k_i and k_f are the wave-vector magnitudes of the incident and diffracted beams respectively, with $k = 2\pi/\lambda$, where λ is the neutron wavelength [108]. The momentum transferred to the crystal after scattering is $\hbar\,|\mathbf{Q}|$ and $2\theta_S$ is the angle between the incident and final beams [108].

In elastic scattering, $k_i = k_f$ and the condition for Bragg scattering is depicted by the Ewald sphere in three dimensions. The condition to satisfy the Bragg condition is given by

$$\mathbf{Q} = \mathbf{G} = \mathbf{k_f} - \mathbf{k_i} \tag{5.3}$$

where $\mathbf{G}$ is a reciprocal-lattie vector [108].

In inelastic, $k_i \neq k_f$ since there is an energy transfer between neutrons and a sample. For single crystals, the energies depend only on the relative momentum defined with a Brillouin zone and the momentum transfer can be expressed relative to the nearest reciprocal lattice vector $\mathbf{G}$ [108]. Hence,

$$\mathbf{Q} = \mathbf{G} + \mathbf{q} \tag{5.4}$$

If $\mathbf{Q}$ is kept constant, one can consider a simple scenario of varying k_i while keeping k_f. If k_i is bigger than k_f, then the energy is transferred from the neutron beam into the sample. Similarly, if k_i is smaller than k_f, then energy is given away from the sample to the beam.

In inelastic scattering experiments where one is interested in measuring energy excitations such as phonon spectrum or magnetic fluctuations at the transition

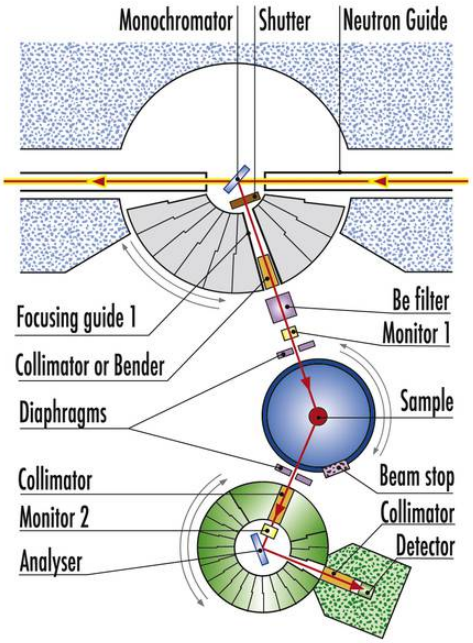

Figure 5.1: Instrument layout of IN14 at the Institut Laue-Langevin (ILL). Taken from the ILL website.

temperature, the triple-axis spectrometry is most commonly used. The three axes correspond respectively to [108]: the monochromator axis, the sample axis and the analyser axis as presented in Fig 5.1. This allows performing either constant-Q or constant-E scans. For example, to keep $\mathbf{Q}$ constant when changing $\mathbf{k_i}$, the angle $2\theta_S$ must change as the orientation of the sample with respect to $\mathbf{k_f}$. In practice, $\mathbf{k_f}$ is kept fixed in space while the sample is being rotated [108]. The other necessary parts of the instrument include monochromators, energy filters, collimators, focusing guide, diaphragms and detector, Fig 5.1. Of particular importance are the monochromators, since they control the intensity of the beam incident on the sample and select the specific wavelength.

Finally, it is worth noting a general result coming from the magnetic scattering. It can be shown [109] that the partial differential cross-section, which is a measure of the counting rate per unit solid angle per energy, for unpolarised beam is given by

$$\frac{d^2\sigma}{d\Omega dE} \propto \frac{k_f}{k_i}(\delta_{ij} - \hat{Q}_i\hat{Q}_j)\left[VS_{m_im_j}(\mathbf{q},\omega) + \langle m_i(\mathbf{q})\rangle\langle m_j(-\mathbf{q})\rangle 2\pi\delta(\omega)\right] \tag{5.5}$$

where k_f and k_i are defined above, $S_{m_i m_j}(\mathbf{q}, \omega)$ is a spin correlation function, m is magnetisation and V is volume. The second term is proportional to $\delta(\omega)$ and involves no energy change of the scattered neutrons – therefore, it gives the information about long-range order and is entirely elastic [109]. The first term is inelastic and it contains information about spin excitations [109].

5.2 Sample Preparation and Characterisation

The UGe_2 sample used in the experiment was a single crystal grown by the Czochralski method. It was spark cut to the dimensions of 6.1×3.4×4.0mm. The electrical resistivity was measured using a second sample (roughly 5 times smaller) coming from the same crystal growth. The resistivity was measured at ambient pressure using the four-point method with a lock-in amplifier and is presented on Fig. 5.4 (a). The PM-FM transition at $T_c = 53$K is indicated by a clear drop in resistivity, Fig 5.4(a). The obtained value of the residual resistivity ratio (RRR) was 62. Both samples were mounted on the pressure cell table as presented in Fig. 5.2.

The sample was pressurised using the large volume two-layered piston-cylinder pressure cell which combines a large sample volume with a safe operating pressure limit of 18 kbar and was optimised for inelastic neutron scattering experiments [110]. The cell is presented in Fig. 5.3. Pressure inside the cell at low temperature was determined to be 11.8 kbar using the established phase diagram of UGe_2. The crystal parameters at that pressure were measured to be: $b = 14.968$Å and $c = 4.100$Å. The rocking curve taken through $Q = 2\pi(0, 0, 1)/c$ at the same pressure gave the mosaic of 1.3° and is presented in Fig. 5.4 (b). This value of Q was chosen since this Bragg peak is almost entirely magnetic due to very small nuclear contribution.

The triple axis spectrometer IN14 at the Institut Laue-Langevin, described above, was used to obtain elastic and inelastic neutron scattering data. For measurements at low temperatures, the cell was loaded in the ILL orange cryostat with a base temperature of 1.5K. The inelastic data points were taken on $Q = 2\pi(0, 0, 1.04)/c$ at different temperatures at three energy transfers of 0.15meV, 0.25meV and 0.35meV. A cold beryllium filter (77 K) was placed on the incident momentum side. A neutron beam with fixed final momentum

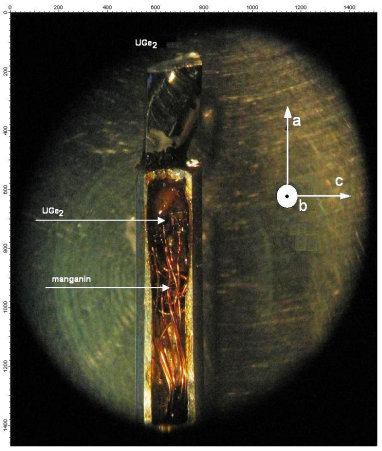

Figure 5.2: Pressure cell table with two UGe_2 samples mounted. The small sample (indicated by an arrow) was used to measure the electrical resistivity. The big sample, mounted on the top part of the table, was used for inelastic neutron scattering.

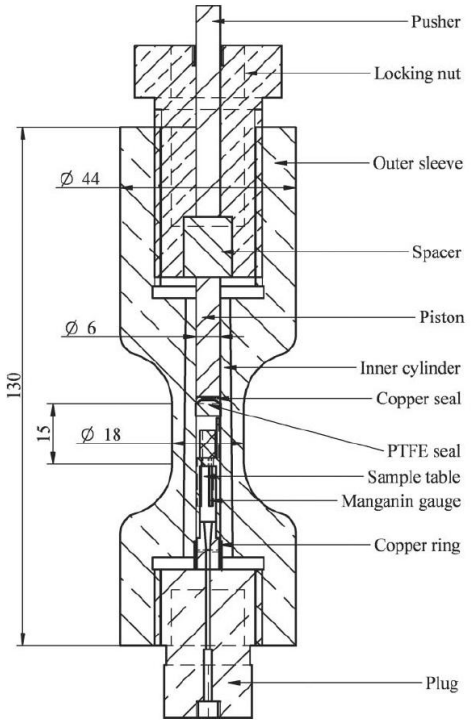

Figure 5.3: Large volume high-pressure cell used to collect inelastic neutron scattering data. The cell allows also for simultaneous transport measurements. Adopted after [110].

$k_f = 1.3\text{Å}^{-1}$ was used. The energy resolution was determined from the incoherent scattering with $Q = 2\pi(0, 0.4, 1.04)/c$ and had a full width at half maximum (FWHM) of 0.10meV. The W-configuration was used as a setup geometry and

a PG (002) analyser with horizontal and vertical focusing. The temperature was measured using a Cernox thermometer which was mounted at the end of the probe very close to the pressure cell.

The neutron scattering intensity of the elastic scan taken on $Q = 2\pi(0, 0, 1)/c$ is proportional to the square of magnetisation and clearly shows the two transitions: first, PM-FM with $T_C = 33.5 \pm 0.5$K; and second, FM1-FM2 with $T_x = 8.5 \pm 0.5$K, Fig. 5.5.

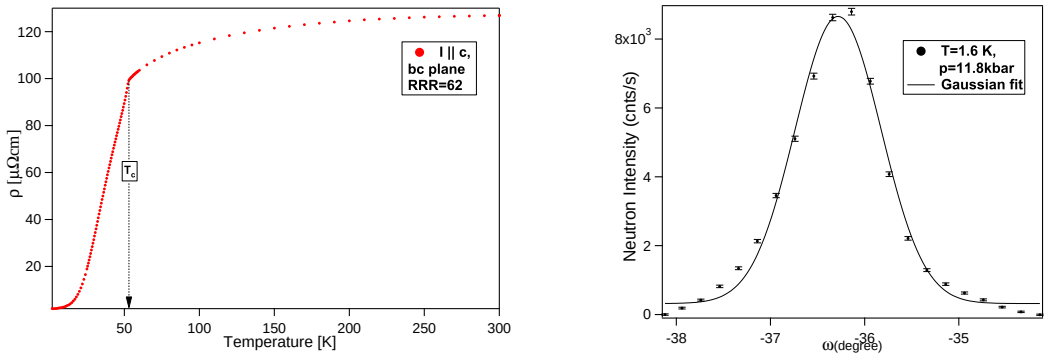

(a) (b)

Figure 5.4: **(a)** Resistivity of UGe_2 at ambient pressure with current along c-axis within bc-plane. The PM-FM transition is observed at $T_c = 53$K. **(b)** The rocking curve taken at $p = 11.8$kbar on $Q = 2\pi(0, 0, 1)/c$ at $T = 1.6$K (background subtracted). Solid line is the Gaussian fit to the data. The measured mosaic was 1.3° at FWHM.

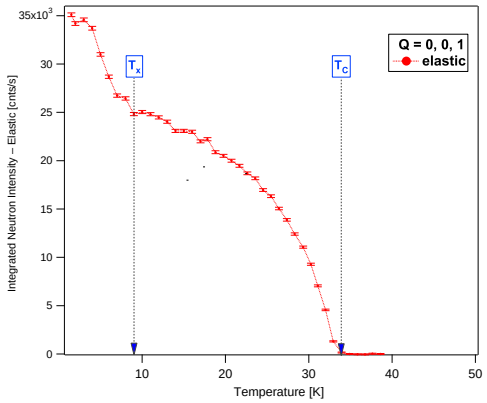

Figure 5.5: Elastic scattering data taken at $Q = 2\pi(0, 0, 1)/c$ and at $p = 11.8$kbar. Two phase transitions are clearly seen: PM-FM with $T_C = 33.5 \pm 0.5$K; and FM1-FM2 with $T_x = 8.5 \pm 0.5$K.

5.3 Results, Analysis and Comparison with Ambient Pressure

The ferromagnetic fluctuations are described in terms of the inelastic magnetic scattering cross section which is by [111]

$$\frac{d^2\sigma}{d\Omega dE} = \frac{k_f}{k_i}\frac{4}{\pi}\left(\frac{m_n\mu_n}{\hbar^2}\right)^2 (\delta_{ij} - \hat{Q}_i\hat{Q}_j)\,|F_Q|^2\,\frac{\chi''_{ij}(\mathbf{q},\omega)}{1-\exp(-\beta\omega)} \tag{5.6}$$

where $\chi''_{ij}(\mathbf{q},\omega)$ is the imaginary part of the dynamic susceptibility, $|F_Q|$ is the magnetic form factor which comes from uranium f electrons and $\mathbf{Q}$ is the total wave-vector and is given by $\mathbf{Q} = \mathbf{q}+\mathbf{G}$. $\mathbf{G}$ is the reciprocal lattice vector and $\mathbf{q}$ lies within the first Brillouin zone [111]. For a nearly ordered itinerant ferromagnet, the imaginary part of the susceptibility is given by [46, 111]

$$\frac{\chi''(\mathbf{q},\omega)}{\omega} = \chi(\mathbf{q},\omega)\frac{\Gamma_\mathbf{q}}{\omega^2+\Gamma_\mathbf{q}^2} \tag{5.7}$$

where the (ij) components were dropped due to the Ising nature of UGe_2 for which the dynamic susceptibility is strongly anisotropic, i.e. $\chi_{aa} \gg \chi_{bb}, \chi_{cc}$ [111]. The above equation has a form of a Lorenztian in terms of $\Gamma_\mathbf{q}$ that is given by

$$\Gamma_\mathbf{q} = \frac{\gamma_q}{\chi(\mathbf{q})} \tag{5.8}$$

where $\chi(\mathbf{q}) = \chi(q,\omega = 0)$. A further simplification is possible, noting that measurements were done at small q, so $\chi(\mathbf{q})$ can be replaced by the uniform susceptibility. Hence, $\chi(\mathbf{q}=\mathbf{0},\omega=0) = \chi_0$ in here. This convenient expression allows to use the data taken using a SQUID magnetometer from [111].

Using the above expressions, one can fit all the data for the whole temperature range with only one free paramter $\gamma_{\mathbf{q}=0} = \gamma_0$ [46, 111].

Fig 5.6 presents the ambient pressure data (normalised with respect to monitor), at three energy transfers of 0.15 meV, 0.25 meV and 0.35 meV with $Q = 2\pi(0,0,1.04)/c$. The data was taken from [111]. No background was subtracted from the data. The overall small background was assumed to be the same for the three energy transfers and was included in the fit as a constant. The sources of background include incoherent scattering and contamination from the Bragg peak. These are more likely to contribute to the lower energy transfers.

On the other hand, the energy resolution was 0.1 meV at FWHM. Therefore, data was collected sufficiently away from the zero energy and the value of Q was chosen to work on the side of the Bragg peak in order to minimise the contamination.

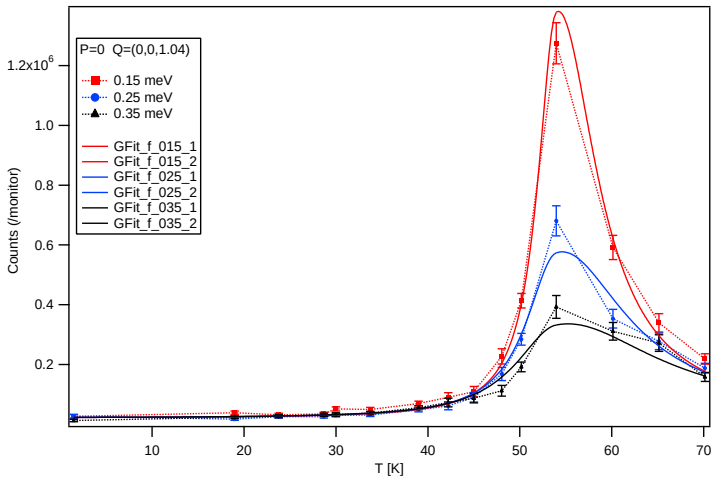

Figure 5.6: Ambient pressure data taken from [111]. The solid lines are result of the simultaneous fit to all data.

Fig 5.7 presents the data at 11.8 kbar (normalised with respect to monitor). The incoherent background measured at $Q = 2\pi(0, 0.4, 1.04)/c$ was subtracted.

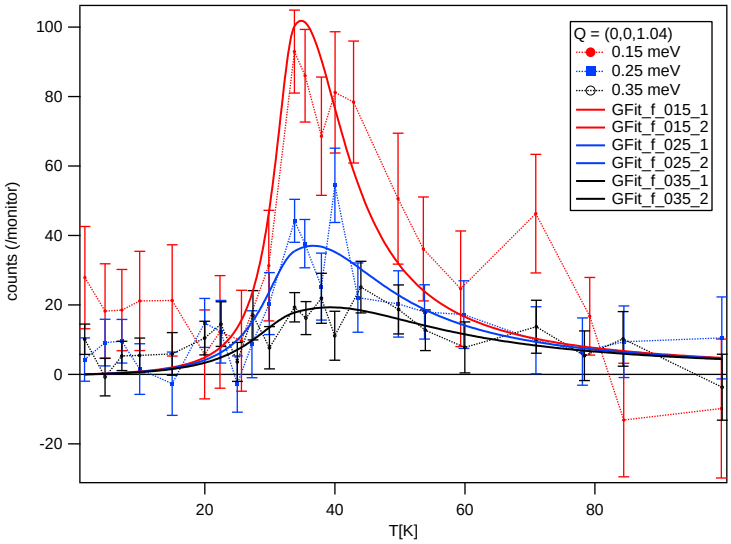

Figure 5.7: Inelastic neutron data. The solid lines are result of the simultaneous fit to all data.

The solid lines in Figs. 5.6 and 5.7 are the fits to the Eq. 5.7 including the Bose factor and three free parameters: a temperature independent constant

background, a scale for the scattering amplitudes and γ_0. As the value of γ_0 does not change with the energy transfer and it is assumed to be temperature independent, the fits were done simultaneously to all three energy transfers. As explained above, the susceptibility in Eq. 5.7 was replaced with the static susceptibility χ_0 given by the Curie−Weiss law. The value of the static susceptibility was obtained using the SQUID magnetometer data taken again from [111]. This value changes at the Curie temperature and its temperature dependence near T_C is predicted by the mean-field theory. There is a difference of a factor of two in the slope, below and above T_C, of the graph of $1/\chi_0$ versus temperature. The change of χ_0 upon the transition was included in the fits. The values of γ_0 obtained from the fits were: $\gamma_0^{0\ \mathrm{kbar}} = 0.70 \pm 0.08\,\mu\mathrm{eV}$ and $\gamma_0^{11.8\ \mathrm{kbar}} = 0.26 \pm 0.03\,\mu\mathrm{eV}$.

The Lorentzian function of ω with the line width $\Gamma(q)$ provides information on the power spectrum of magnetic fluctuations. For a nearly ferromagnetic metal, the conventional paramagnon theory predicts $\Gamma(q) \propto q$ (in the absence of impurities) and $\Gamma(q) \propto q^2$ (in the presence of impurities) [112]. Therefore, the value of $\Gamma(q)$ (and also χ'') vanishes as $q \to 0$. This is a consequence of the spin conservation for a single component Fermi liquid. The linear q dependence of $\Gamma(q)$ can be explained in terms of Landau damping. Taking the spatial period of magnetic oscillation to be L and assuming the electron velocity to be the Fermi velocity v_F, the time for a spin to move between "the peaks" in the magnetic oscillation is given by L/v_F. This simple result can be related to the relaxation rate and one can write $\Gamma \approx v_F q$. Experimental observations of the above dynamics include metals such as Ni or Fe [113].

On the other hand, the vanishing value of $\Gamma(q)$ is not observed in some ferromagnetic systems. They include systems where the several different bands cross the Fermi level, systems with strong spin-orbit coupling or systems with two-component response [112]. As example of the last type is UPt_3 [114]. UGe_2 is also an example of a two-component system with conduction electrons interacting with the local moments (or, more generally, of a multi-component systems with multiple bands interacting with the local moments).

In two-component systems, the contributions to $\Gamma(q)$ come from the localised spins and from the itinerant electrons. The total spin of both components is conserved and the value of $\Gamma(q)$ vanishes for small q (the contributions from the

two components cancel each other). However, the total spin of the localised spins is not a conserved quantity [112] and therefore the value of $\Gamma(q)$ does not vanish. Furthermore, it can be shown that the local $\Gamma(q)$ (i.e. local spin contribution to total one) is proportional to the self-energy of the conduction electrons [112]. If the electron scattering is dominated by magnetic scattering then $\Gamma(q)$ would be proportional to electrical resistivity.

Relating the value of $\Gamma(q)$ with resistivity would explain why γ, obtained from the above fits, is smaller at pressure. As can be seen the resistivity value at T_C is smaller at higher pressures, Fig 5.8 after [115].

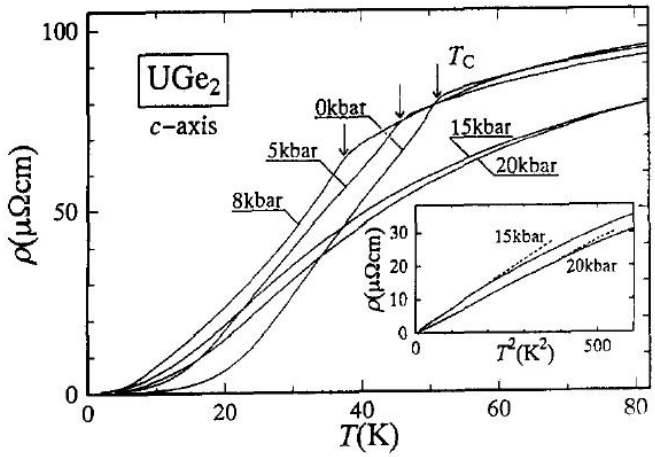

Figure 5.8: Resistivity of UGe_2 as a function of temperature measured at different pressures. After [115].

Finally, it should be noted that attempts to measure phonons with inelastic neutron scattering were made. The experiment was done in order to obtain phononic background contribution (coherent and incoherent) to the magnetic inelastic scattering presented in Fig. 5.7. The experiment was done using thermal neutron three−axis spectrometer spectrometer IN22. Unfortunately, the measured signal was identified to be due to the body of the pressure cell. It was found that this signal was temperature dependent, energy transfer dependent and also depended on the orientation of the cell. Such a complicated background coming from the amorphous material constituting the body of the cell was dominant and it was impossible to obtain the signal from the sample.

5.4 Conclusions

The work presented here does not reveal ferromagnetic spin fluctuations at T_x associated with the FM1-FM2 transition. Instead, the fluctuations at T_C associated with the PM-FM transition were observed. Furthermore, the energy scale of the fluctuations at T_C was shown to decrease at high pressure as compared with the energy scale at ambient pressure where there is no superconductivity [111]. This might suggest that the fluctuations at T_C are unlikely to play a role in inducing superconductivity. On the other hand, the previous results [30,36,111] show that the $5f$ electron still contribute to most of the differential susceptibility and are responsible for most of bulk magnetic properties at the temperature and pressure conditions similar to those presented above. However, it was also suggested by the muon spin spectroscopy measurements [30] that the FM1-FM2 transition might be due to conduction electrons which would not be detected in the above experiment. The inelastic scattering from the conduction electrons is strongly suppressed by the magnetic form factor and cannot be measured in the standard three-axis geometry (the performed experiment was mostly sensitive to f-electron part owing to magnetic form factor).

Chapter 6

Ultrasonic Measurements in the Piston Cylinder Cell

This chapter presents the pulse echo technique experiment under pressure. Sample preparation and the assembling of the piston cylinder cell are described. The data collection of the pulse spectra is discussed. The results at different pressures are presented and analysed.

6.1 Sample Preparation

The sample used for the pulse echo technique was a cubic shape single crystal of UGe_2 which was spark cut to the dimensions of 2.959×1.2×2mm (length × height × width). Length was measured to a greater precision compared with the other dimensions, since it corresponds to the a-axis along which the ultrasound echoes were measured. The orientation of the sample was done by the back-reflection Laue x-ray method scanning both top and bottom faces of the sample. The alignment was done to ±0.5°. The top face was used to mount the transducer, the bottom was used to glue the sample to the pressure cell table, Figs. 6.1, 6.3 and 6.4.

As discussed in Chapter 3, the pulse echo technique requires a fine surface finish but also adequate parallelism between the faces used in the measurement. Therefore, special care was taken when spark cutting the top and bottom faces of the sample. After sparkcutting, the sample was glued to a sapphire cylinder using Crystal Bond. The sapphire was used since it had a very flat face ideal

to ensure parallelism during polishing. The cylinder, with a sample mounted on top, was then inserted into the epoxy resin holder, Fig. 6.2. The void between the sample and the epoxy resin was filled in with wax in order to further support the sample during polishing, Figs. 6.2 and 6.3.

The polishing process involved several steps, Fig. 6.3, with different grain sizes of the silicon carbide grinding paper and was done by hand. The final stage of polishing was done on a soft polishing cloth with a diamond slurry with the grain size of $1\,\mu$m. Therefore, the resulting average surface roughness was much less than $10\,\mu m$. As explained in Chapter 3, such a surface finish was more than adequate since an ultrasonic wave with the frequency of 50 MHz and speed of $5000\,\frac{\mathrm{m}}{\mathrm{s}}$ has a corresponding wavelength of $100\,\mu m$ (very similar to the wavelengths in this experiment). The other side of the sample was polished in order to ensure parallelism but since it was not used to glue the transducer the grain size was bigger than $10\,\mu m$.

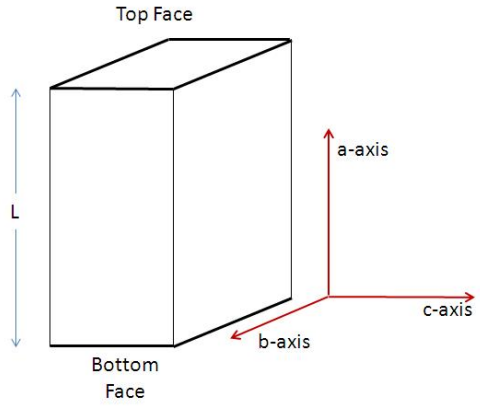

Figure 6.1: The schematic orientation of the UGe_2 sample used in the pulse echo measurements. The pulse was sent along the a-axis, therefore length L had to be measured precisely.

When the polishing was finished, the sample was removed from the polishing holder and was investigated carefully under the microscope. After ensuring the good quality of the surface finish, the sample was ready for mounting the transducer through chemical bonding. The list of adhesive used to connect the transducer to the sample included:

1) GE Varnish
2) Cyanoacrylate

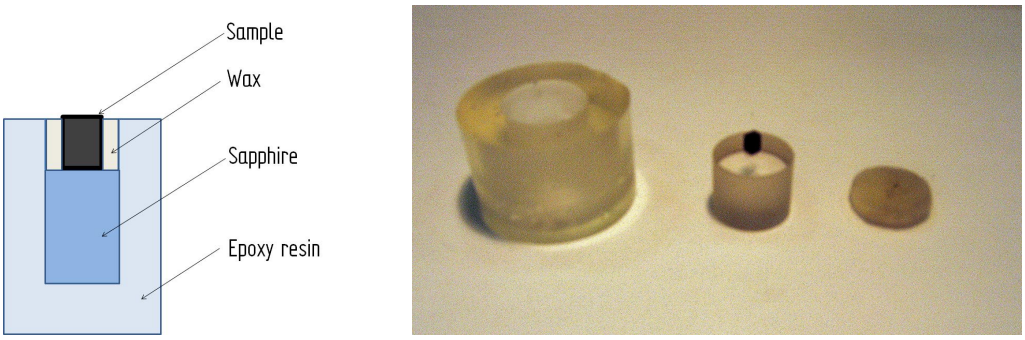

(a) (b)

Figure 6.2: **(a)** A cross-sectional view of the polishing holder. (b) The picture of different parts of the polishing holder and the sample. Starting from the left: epoxy resin, the sample mounted on the sapphire crystal, wax.

3) Crystal Bond
4) Phenyl Acetate
5) Vacuum Grease

The best results were obtained with Cyanoacrylate and Crystal Bond. It must be noted that this step of the sample preparation was the most troublesome. It had to be ensured that the minimal amount of the adhesive is evenly distributed between two elements. If too much was applied, the signal was attenuated by the adhesive. On the other hand, if the amount of adhesive was too small, the contact between two elements was not able to transmit the signal. The correct amount of adhesive was very hard to quantify and therefore the gluing process had to be done by trial and error. Further complication was caused by the small thickness of the transducer. When the glue was applied and the transducer was carefully positioned on the top face of the sample, the two elements had to be clamped together using a vice. The thin transducers were relatively easy to crack if too much force was used. Again, this step had to be done by trial and error.
The quality of the connection between the transducer and the sample, Fig. 6.4, was tested by connecting the setup to the oscilloscope and investigating the raw spectrum for the subsequent echoes. An example of a raw spectrum, coming from a successful connection, is presented in Fig. 6.7.

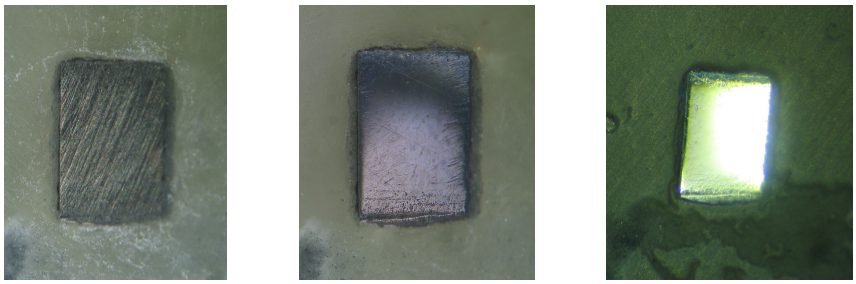

(a) (b) (c)

Figure 6.3: Three initial stages of the polishing process.

6.2 Pressure Cell Preparation

The pressure cell used for the pulse echo measurements was a copper-beryllium piston cylinder cell designed by Christopher Ridley. The cell had a bore size of 5 mm. The cell consisted of a plug which provided a feedthrough for the wires but it was also used, together with a copper washer, to seal the pressure cell from the bottom end. The plug had a sample table which was used to accommodate the sample, Fig. 6.4. After the sample was positioned on the table, the electrical connection with the transducer had to be established. This was achieved by connecting the copper wires of the plug using conducting silver epoxy, Fig. 6.4. The manganin wire, placed under the sample table, was used for the pressure calibration. When all electrical connections were established, the plug was threaded in the main body of the cell and then locked in place by squeezing a soft copper ring (placed between the plug and the body) using a spanner.

When the plug was secured and locked in, the bore of the cell was filled in with the pressure medium. The pressure medium used in this experiment was mineral oil. It had to be ensured that the level of the pressure medium was sufficient to engage the tungsten carbide piston into the bore. The piston sealing was provided by a rubber o-ring and a soft copper washer. A copper-beryllium pusher was placed on the piston. A locking nut was used to close the cell. The pressure was applied by a hydraulic press.

After achieving the desired pressure, the pressure cell was placed in the holding bracket of the cryostat probe. A Cernox thermometer was positioned on the wall of the cell as close to the sample as possible, Fig. 6.5.

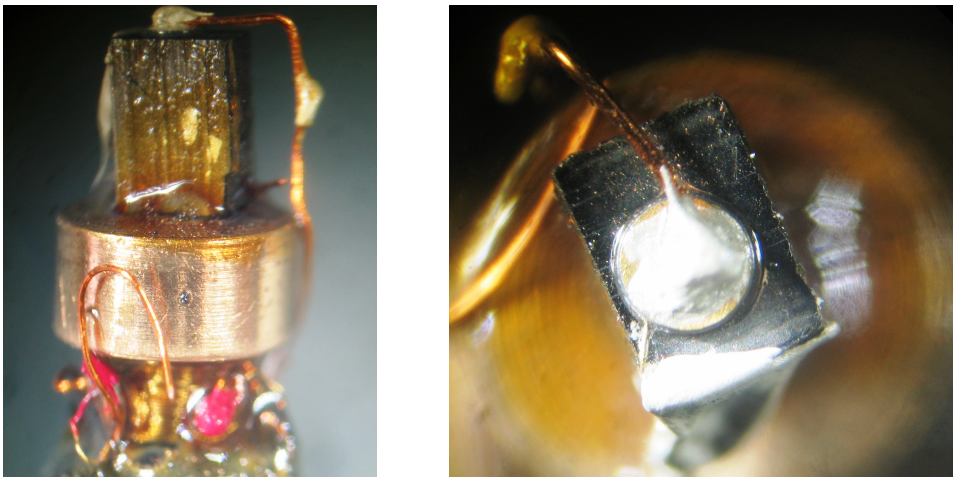

(a) (b)

Figure 6.4: **(a)** UGe_2 sample mounted on the sample table of the piston cylinder cell for pulse echo measurements. **(b)** The top view of the sample and the transducer. Silver epoxy was used for electrical connection.

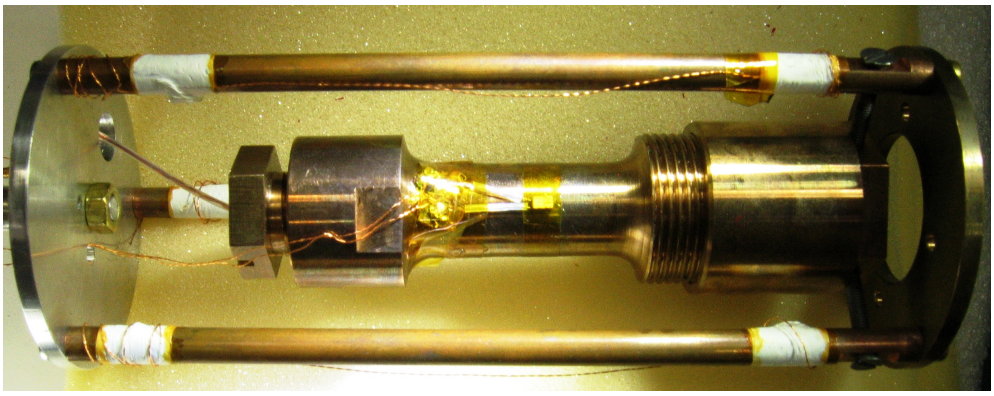

Figure 6.5: The piston cylinder cell mounted on the cryostat probe. The thermometer was attached as close as possible to the sample location on the side of the cell.

6.3 Data Collection

The Agilent DSO–X3052a oscilloscope (500 MHz bandwidth and 4 GSa/s) was used to collect the pulse echo data. The schematic block diagram of the circuitry is presented in Fig. 6.6. The transducer can be considered as a capacitor due to high resistivity of the piezocrystal which is placed in between two metal plates/contact pads. The transducer was connected to the oscilloscope in parallel and the wavegenerator in series. The circuitry had a common ground in order to eliminate any ground loops and avoid interference effects.

Before starting the measurements, the raw spectrum had to be investigated on the scope's screen. The minimum requirement for an acceptable spectrum was a clear peak corresponding to the first echo. The first echo was always the strongest and the easiest to observe since it is attenuated by the sample to the smallest extent.

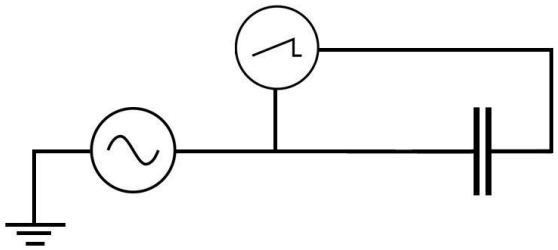

Figure 6.6: Schematic block diagram of the electronic setup for the pulse echo measurements. The transducer can be viewed as a capacitor which is connected in parallel with the oscilloscope (Agilent DSO–X3052A) and in series with the wavegenerator (Agilent DSO–3WAVEGEN).

The spectrum was considered to be of good quality, such as one presented in Fig. 6.7, if three subsequent echoes were observed. In order to distinguish between the peaks coming from the desired reflections (longitudinal wave along a-axis) from noise and interference effects, the amplitude of the peaks had to be at least twice the surrounding background. These peaks were also the most sensitive to any changes of the initial pulse (width and intensity) coming from the wavegenerator – this observation was used additionally to identify the desired peaks. The final check of the raw ultrasonic spectrum was a comparison with the neutron data at ambient pressure from [116]. The results from the neutron studies are presented in Table 6.1. The peak position was easily calculated knowing the speed of sound in particular direction and the length of the sample.

propag^{on}/polar^{on}	a-axis	b-axis	c-axis
a-axis	4300±100	2400±100	2700±100
b-axis	2400±100	3800±100	2600±100
c-axis	2800±100	2200±100	4200±100

Table 6.1: Sound velocities in UGe_2 estimated from the neutron scattering data. Units are $\frac{m}{s}$. Adopted after [108].

All the results presented in this chapter were obtained using a single pulse mode and, hence, there was no need for a signal chopper in the circuitry. The initial pulse had a peak-to-peak intensity of 3.75 V and a width of 20 ns corresponding to a band-width frequency of 50 MHz. The measurements were taken using a LabView program which was controlling the oscilloscope settings but also the cooling rate and the temperature stability of the cryostat.

The measurements consisted of raw spectra containing 8000 datapoints (x, y) each consisting of the values of voltage (y) and time (x). Examples are presented in Figs. 6.7 and 6.8 which correspond to ambient and high pressure data respectively. A single spectrum was collected every 10 s when the oscilloscope was set to average acquisition mode, which was the running average over 500 acquisitions, or every 20 s for the running average over 1000 acquisitions. The data collection rate depended also on the cooling/warming rate of the cryostat, typically 0.1-0.5 K/min. The temperature range of the cryostat was 1.8-300 K. All spectra collected on cooling or warming were loaded into a single text file. A typical cooling or warming took around 12-15 hrs and produced a text file containing 0.5-1.5 GB of raw data.

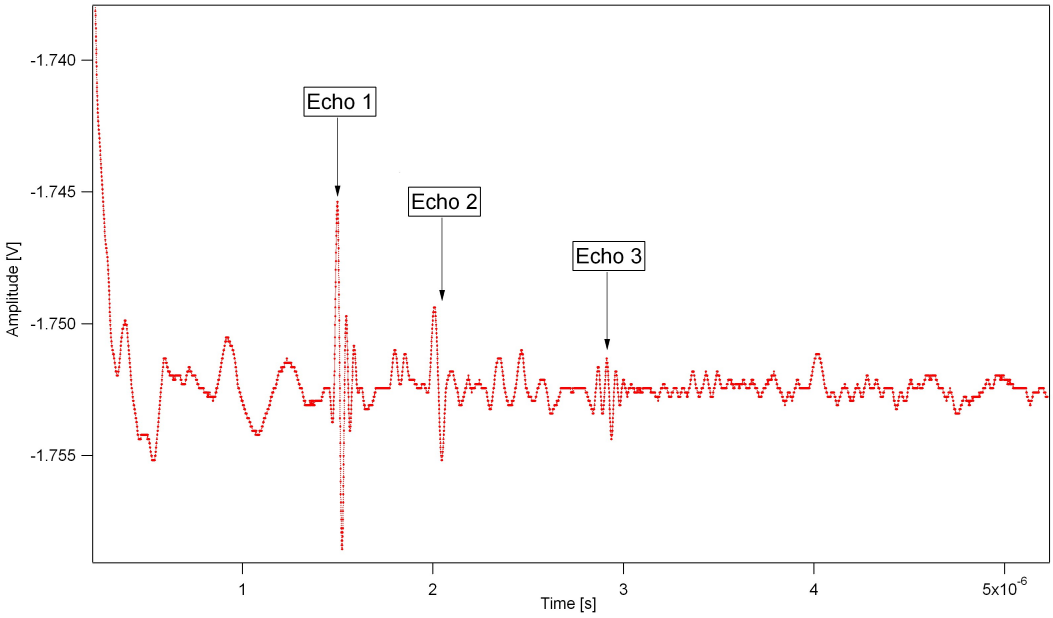

Figure 6.7: The raw data at ambient pressure and room temperature with three echoes clearly seen. The shoulder of the initial peak can also be seen.

The shape of the peaks of the subsequent echoes depends on the form of the initial pulse. In an ideal experiment (perfect bonding, perfect parallelism, no wedge effects, perfect shape of the initial pulse etc.), the shape of the peaks of the subsequent echoes could be described by a wavepacket resulting from a product of a Gaussian and a sine function.

However, in the real experiment, the wavepackets were not symmetrical with respect to its centre. Here, the wavegenerator was operating in a single square pulse mode. However, since the wavegenerator was set to its limit with a pulse width of 20 ns, the shape of a peak was not perfect and was approximated by a half of a sine wave. Furthermore, the distortion of the shape of the wavepacket could come from diffraction effects and the geometry of the sample.

The observation of the asymmetry of the wavepacket suggested that the overall shape could be described by the Ikeda-Carpenter shape. This function is used to model a sharp neutron pulse travelling through a moderator which, in simplified terms, has a very steep rising exponential combined with a slower decaying exponential.
The following function was used to fit the echo peaks

$$f(t) = A\sin(\omega t + \phi)\,[f_{IC}(t - t_0)] \tag{6.1}$$

where f_{IC} is the Ikeda-Carpenter function given by

$$f_{IC}(t-t_0) = \frac{\alpha^3}{2}\left\{(1-R)(t-t_0)^2 e^{-\alpha(t-t_0)} + \frac{2R\beta}{(\alpha-\beta)^3}\left[e^{-\beta(t-t_0)} - e^{-\alpha(t-t_0)}\left(\frac{(\alpha-\beta)^2(t-t_0)^2}{2} + (\alpha-\beta)(t-t_0) + 1\right)\right]\right\} \tag{6.2}$$

where α and β are exponential parameters (corresponding to fast and slow decays in the original problem). R is the so-called mixing coefficient. All the parameters A, ω, ϕ, α, β and R, given by the two equations, were free in the fits.

An example of a fit to the first peak in the spectrum is presented in Fig 6.9. The fitting function was used to identify the peak position and hence obtain the transit time given by Eq. 3.3 which was used to calculate the speed of sound and the elastic constant in a given direction. The fitting function also gave an indication of changes of other parameters of the wavepacktes such as their amplitude or a phase shift as a function of temperature.

As explained above, all data collected on cooling/warming were merged into

a single text file containing several thousand individual spectra. A script written in IGOR Pro Wavemetrics was used to fit the function given by the Eq. 6.1 to each individual spectrum. The script was designed also to split the original data file into individual spectra, so every single one could be plotted. For example, one could select a given temperature and plot the spectrum as it appeared on the oscilloscope screen at that temperature.

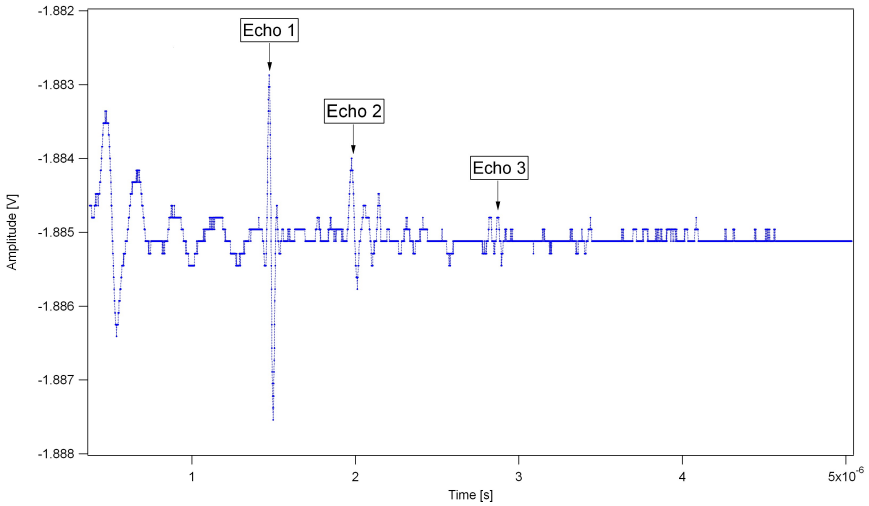

Figure 6.8: The raw data at high pressure and room temperature with three echoes clearly seen. The shoulder of the initial peak can also be seen.

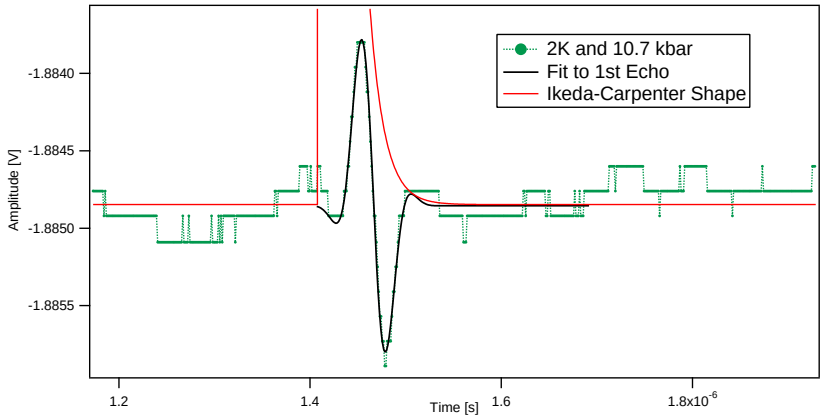

Figure 6.9: An example of a fit to the first echo with the wavepacket function described in the text.

6.4 Results and Discussion

The result section is divided into three parts. The ambient pressure results are presented first. They are followed by the high pressure results. Finally, the results at high magnetic fields are briefly presented. Technical difficulties of the high pressure data collection are also discussed.

6.4.1 Ambient Pressure

The ambient pressure data were collected on the sample described above. The pressure cell was used to mount the sample into the cryostat but it was not loaded nor filled with a pressure medium. The pressure cell acted simply as a sample holder. The same electronic setup, also described above, was used at ambient and high pressure experiments.

The temperature dependence of the position of the peaks (i.e. the transit times) corresponding to the first, second and third echoes is presented in Fig. 6.10 (a–c). The amplitude as a function of temperature of the same peaks is presented in Fig. 6.11 (a–c). Panels (c) on both figures correspond to the third echo in the raw spectrum. This echo had the smallest amplitude since it was attenuated to the greatest extent by the sample. Above 250 K, as can be seen in Fig. 6.11 (c), the peak fitting was problematic due to background noise. Fortunately, the noise was reduced with decreasing temperature and therefore, below 250 K, the fitting was reliable allowing the determination of the transit time.

Using the data from Fig. 6.10 (a–c) and the measured length of the sample, the ultrasonic speed was determined to be $\mathrm{v}_{L_1} = 3950\,\frac{m}{s}$ and $\mathrm{v}_{L_1} = 4080\,\frac{m}{s}$ using the first and third echo respectively from the raw spectrum (using the notation from the Table 2.1). The third echo was the repletion of the first and it covered the total distance of $4L$ compared to $2L$ of the original one. Therefore, covering a longer distance, it is expected to give a more accurate measurement of the true ultrasonic speed. Using the two values and considering the errors associated with the sample length measurement, the longitudinal speed of sound along the a-axis was estimated to be $\mathrm{v}_{L_1} = 4015 \pm 100\,\frac{m}{s}$ at room temperature. Referring to the Table 2.1, it is known that v_{L_1} corresponds to the elastic constant c_{11} and hence it is possible to plot the temperature dependence of c_{11}, Fig. 6.14. The speed of sound corresponding to the second peak in the spectrum was determined

to be $v_{T_2} = 2915 \pm 100 \frac{m}{s}$ at room temperature. As explained, the direction of propagation of the wave was along the a-axis. Comparing this value with the speed obtained from the neutron data, Table 6.1, this echo was identified to correspond to a transverse wave along a-axis with c-axis polarisation. Referring again to the Table 2.1, it is known that v_{T_2} corresponds to the elastic constant c_{55} and hence it is possible to plot the temperature dependence of c_{55}, Fig. 6.14.

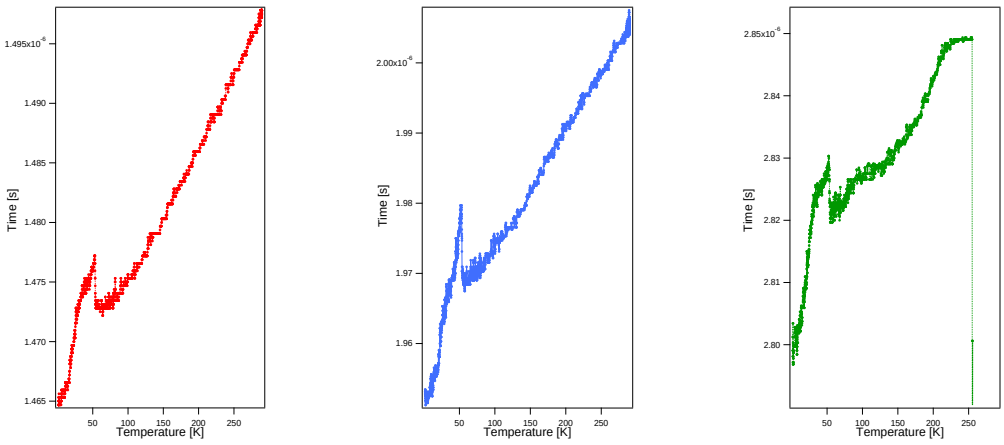

(a) (b) (c)

Figure 6.10: The transit times as a function of temperature for UGe_2 sample described in the text at ambient pressure. **(a)**, **(b)** and **(c)** correspond to the first, second and third echoes respectively in the raw spectrum. The third echo was the most difficult to fit and hence the transit time could be reliably obtained below 250 K where the noise was smaller.

Attenuation

The normalised attenuation associated with the elastic constants c_{11} and c_{55} is presented in Fig. 6.12. The attenuation was calculated using the following expression

$$\alpha = 20 \frac{1}{x_2 - x_1} \log \left(\frac{A(x_1)}{A(x_2)} \right) \tag{6.3}$$

where $A(x_1)$ and $A(x_2)$ are the amplitudes of the ultrasonic wave at positions x_1 and x_2. Here, the units of attenuation are $\frac{\text{db}}{\text{cm}}$ in contrast to the Eq. 3.6. $x_2 - x_1$ was taken to be $2L$ – twice the sample length, since the amplitudes were measured at $2L$ and $4L$. The amplitudes of the first and third echoes were, as explained, associated with c_{11} (blue data in Fig. 6.12). The amplitudes of the second and

fourth echoes were associated with c_{55} (red data in Fig. 6.12) corresponding to the attenuation of the transverse wave with the propagation along the a-axis with c-axis polarisation. It must be noted here, that the fourth echo was even smaller than the third echo and, therefore, the peak fitting was unattainable. On the other hand, a consistent increase of amplitude was observed in the raw spectrum just above $4\,\mu s$, Fig. 6.7, which was identified to be the repetition of the second echo. The amplitude of the fourth echo was taken to be the maximum value of voltage of this feature.

One needs to be careful when interpreting the attenuation results. First of all, all the measurements performed here were done at a constant driving frequency. However, in contrast to the speed of sound, ultrasonic attenuation is frequency dependent since the dissipation of energy will depend on the frequency. Therefore, in order to fully study the behaviour of the attenuation, all the measurements would have to be repeated at different driving frequencies. As already explained in Chapter 3, this would require faster electronics due to the limited sample sizes required for the pressure cell.

Furthermore, the single transducer method is associated with the following problem. The attenuation measured in such a setup will include the attenuation coming from the sample but also from the bonding and the transducer itself. All these elements will behave differently at different conditions of temperature and pressure. This implies that only relative changes of the attenuation may be measured. Finally, the condition for the parallelism is of great importance here and it was shown that condition becomes more critical for higher frequencies since there signal losses will be greater [54]. Nonetheless, there are some characteristic features in the temperature dependence of the attenuation that are described below.

Both attenuation curves, "longitudinal" and "transverse", have clear peaks positioned at around 218 K and 122 K for c_{11} and c_{55} constants respectively. As explained in Chapter 2, such a feature could be a Bordoni peak which was observed previously in metals such as lead, aluminium, silver and copper [54]. Some of the features of the Bordoni peaks were introduced in section 2.2. In order to examine it more closely, one can follow an explanation by [117]. The increase in the ultrasonic attenuation is essentially due to the movement of dislocation lines. If one considers a dislocation line lying along a closely packed plane in a

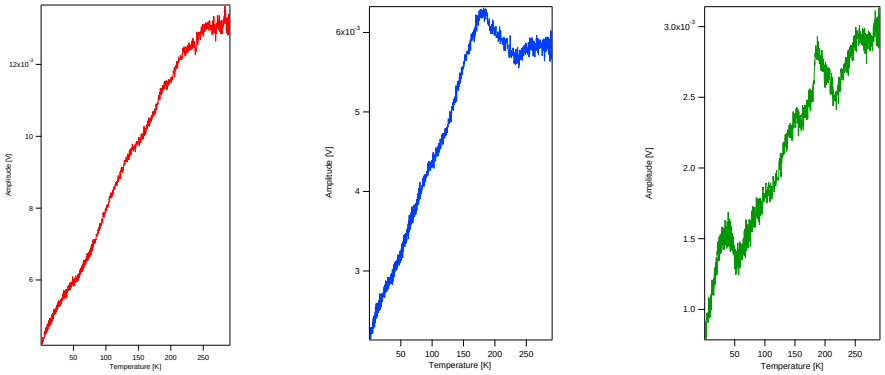

(a) (b) (c)

Figure 6.11: The amplitudes as a function of temperature for UGe_2 sample described in the text at ambient pressure. **(a)**, **(b)** and **(c)** correspond to the first, second and third echoes respectively in the raw spectrum.

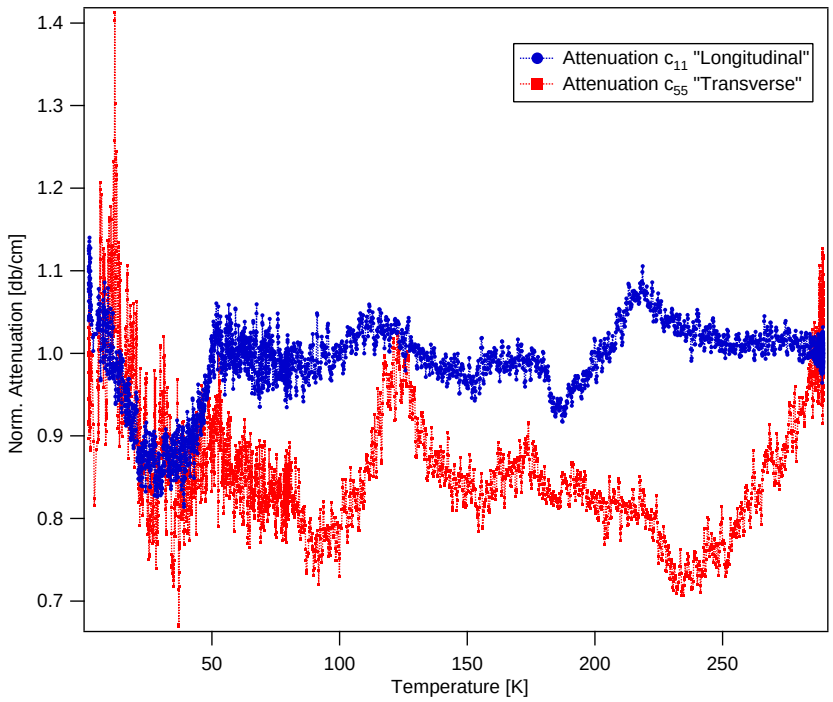

Figure 6.12: Normalised attenuation as a function of temperature. The plots were obtained using Eq. 6.3: attenuation c_{11} was obtained using raw data from Fig. 6.11 panels (a) and (b); attenuation c_{55} from panel (c) and the amplitude of the fourth echo (not shown) as explained in the text.

crystal in the absence of thermal fluctuations, a shear stress is equal to the Peierls stress [54]. The Peierls stress is defined as the force required to move a dislocation from a plane of atoms in a unit cell. When the fluctuations are present at finite

temperatures, the dislocation line will not be confined to its potential energy minimum and might exhibit kinks and bulges – hence, the dislocation line might be "distributed" between different closely packed planes. Stresses much smaller than the Peierls stress will be sufficient to move such kinks, that is, in a direction parallel to the dislocation line, where the potential barriers are small [54]. Under the influence of the propagation of a stress wave (ultrasound) a new formation of kinks is possible and hence the source of energy dissipation of the ultrasound wave. Therefore, the peak originates from the thermally activated process and its relaxation time displays the Arrhenius-type temperature dependence [54]. Or in more simple terms, the temperature at which the peak occurs depends on the driving frequency of the ultrasonic wave and is given by [54]

$$\omega = \omega_0 \exp\left(-\frac{E}{kT}\right) \tag{6.4}$$

where ω_0 is the so-called attempt frequency and E is the activation energy or kink formation energy. If the peak arises from a simple process with only one value of the activation energy and attempt frequency, the dissipation at the given frequency ω is given by [54]

$$\frac{1}{Q} = 2\frac{1}{Q_m}\frac{\left(\frac{\omega}{\omega_m}\right)}{1+\left(\frac{\omega}{\omega_m}\right)^2} \tag{6.5}$$

where $1/Q_m$ is the maximum dissipation and $\omega_m = \omega_0 \exp(-E/kT_B)$. T_B is the temperature where the Bordoni peak is positioned. Q is the quality factor and it is inversely proportional to the ultrasonic attenuation, i.e. $\alpha \propto 1/Q$.

As explained above, all the measurements were done at the same driving frequency. Hence, it is possible to use the Eq. 6.5 to fit the attenuation as a function of temperature with fixed driving frequency. Substituting Eq. 6.4 and the expression for ω_m into 6.5 yields

$$\alpha = \frac{1}{Q} = 2A\frac{\exp\left(-\frac{E}{k}(\frac{1}{T}-\frac{1}{T_B})\right)}{1+\left(\exp\left(-\frac{E}{k}(\frac{1}{T}-\frac{1}{T_B})\right)\right)^2} \tag{6.6}$$

The free parameters in the function are: E, the activation energy which indicates the width of the peak, a temperature independent background and A, describing

the overall amplitude inversely proportional to the maximum dissipation. The results of the fit are presented in Fig. 6.13. The data in Fig. 6.13 were interpolated (Smoothing Spline Algorithm in IgorPro) from the raw data from Fig. 6.12. Only the temperature range in the vicinity of the peak was considered.

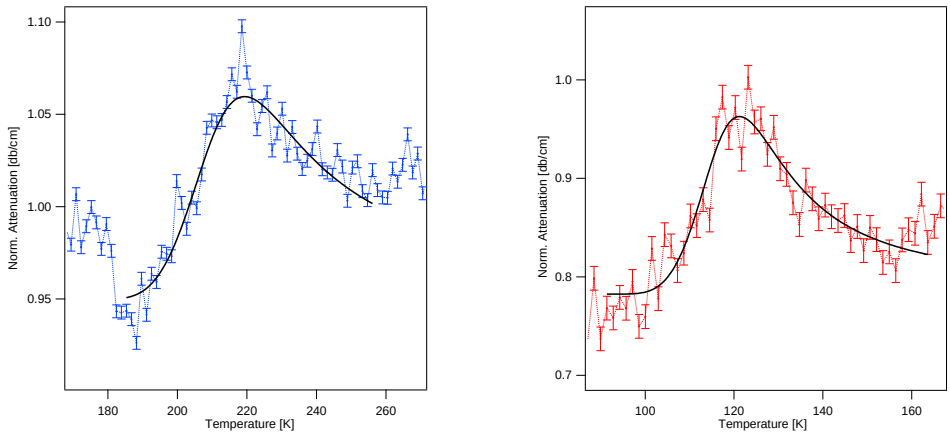

(a) (b)

Figure 6.13: **(a)** The peak in the normalised attenuation as a function of temperature associated with c_{11}. **(b)** The peak in the normalised attenuation as a function of temperature associated with c_{55}.

The values obtained from the fits were $E = 0.29 \pm 0.03\,\text{eV}$ (for c_{11}) and $E = 0.11 \pm 0.01\,\text{eV}$ (for c_{55}). The values found in the literature and obtained experimentally (for the simple metals Pb, Al, Ag and Cu) vary from 0.05 eV to 0.2 eV [54]. It seems, therefore, that the values obtained here are slightly overestimated. It must be noted that the activation energy as well as the attempt frequency are normally obtained by varying the driving frequency and noting the peak temperature. They are then calculated using the Eq. 6.4 rather than 6.5. Furthermore, the above calculation does not provide any information on the value of ω_0.

These results are only indicative within the correct order of magnitude. One of the open questions here concerns the different positions of the peaks for the transverse and longitudinal modes. This difference might originate in the anisotropy of the crystal but this question requires more careful investigations in the future.

Apart from the peaks, attenuation associated with c_{11} exhibits a clear change

at $T_C = 53\,\mathrm{K}$ which is associated with the para- to ferromagnetic transition. The other attenuation, corresponding to the transverse wave, does not exhibit any clear features at the transition. Only a slight increase can be seen at the transition; however, the scatter of the data, at these temperatures, is large. The reason behind the difference between the two attenuation curves might be the fact that only longitudinal ultrasound waves are sensitive to the magnetic phase transitions (see sections 2.3 and 2.4). The ultrasonic attenuation can exhibit a critical behaviour at the transition. However, as before, the measurements were performed at a single driving frequency and in order to fully study the attenuation upon the transition measurements at different frequencies are required.

Nonetheless, the fit suggest that the structure in the attenuation seen above 50 K is real and may be due to the dislocations although with a more complex distribution of activation energies than just considered.

Finally, the values of the attenuation coefficients for both modes at lowest temperature are used to calculate the effective electron mass in the section below. At the lowest temperatures, the main contribution to the attenuation comes from electrons as explained in section 2.3.2.

Elastic Constants

The temperature dependence of the elastic constants c_{11} (blue data) and c_{55} (red data) is presented in Fig. 6.14. The data might be split into three different temperature ranges: (1) the high temperature range where behaviour of the elastic constant is dominated by the anharmonic effects; (2) the phase transition region and (3) the low temperature limit.

(1) High Temperature Range

The high temperature range can be modelled using the Eq. 2.23 which gives the anharmonic phonon contribution to the elastic constant. The equation has two free parameters a and b as well as the zero temperature elastic constant c_0. The results of the fit are the solid lines in Fig. 6.14 and the fitting parameters are summarised in Table 6.2.

Fitting Parameters	Elastic const. c_{11}	Elastic const. c_{55}
a [Pa]	0.0204±0.0002	0.0137±0.0003
b [K]	245±2	151±3
c_0 [Pa]	1.0161±0.0002	1.0195±0.0005
$c_V\Gamma$ [$JK^{-1}m^{-3}$]	0.00017±0.00001	0.00018±0.00001

Table 6.2: Fitting parameters to normalised c_{11} and c_{55}. The parameters were obtained from fitting of the anharmonic temperature background. Γ is the derivative of the Grüneisen parameter with respect to strain and the high temperature heat capacity per unit volume.

The phenomenological relation given by the Eq. 2.23 and the expression for the temperature dependence given by the Eq. 2.18 can be combined together in the high temperature limit and assuming the Debye model. Expanding the second term for $b \ll T$ in the Eq. 2.18 yields

$$\frac{a}{e^{b/T}-1} \approx \left(\frac{a}{b}\right) T \tag{6.7}$$

so the Eq. 2.23 becomes

$$c(T) = c_0 - \left(\frac{a}{b}\right) T \tag{6.8}$$

On the other hand, the third term in the Eq. 2.18 drops for the high temperature limit of the Debye internal energy and the elastic constant can be written as

$$c(T) = c_0 - \frac{1}{2}\Gamma U(T) = C_0 - \frac{1}{2}\Gamma c_V T \tag{6.9}$$

where internal energy $U(T)$ is expressed per volume and is in Pa (i.e. Pa/m^3). c_0 was scaled appropriately to C_0 . Using the above expressions, the second terms can be combined, so

$$\Gamma = \frac{2}{c_V}\left(\frac{a}{b}\right) \quad \text{or} \quad c_V\Gamma = 2\left(\frac{a}{b}\right) \tag{6.10}$$

where Γ is the derivative of the Grüneisen parameter with respect to strain. c_V is the heat capacity per volume ($JK^{-1}m^{-3}$) and is a constant in this high temperature limit. It is therefore possible to estimate the change of the Grüniesnen parameter at different pressures by obtaining the fitting parameters a and b. The value at ambient pressure is given in Table 6.2.

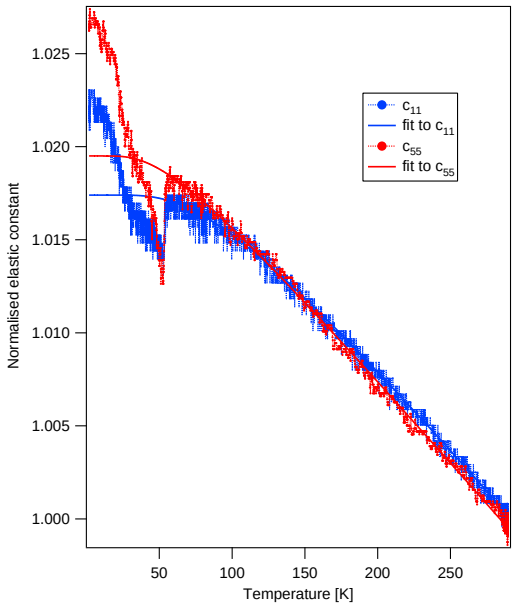

Figure 6.14: Normalised elastic constants c_{11} and c_{55} obtained from the transit time corresponding to the first echo. The solid line is the fit to the high temperature background coming from the anharmonic effects.

(2) Phase Transition Region

Both elastic constants exhibit a sharp drop at the transition. The measured Curie temperature was $T_C = 53.0\,\mathrm{K}$. After the background subtraction and normalisation with respect to the room temperature value, changes of slope around $T = 30\,\mathrm{K}$ can be observed, Fig. 6.15 (b). This change corresponds to the cross-over region on the UGe_2 phase diagram. The change of elastic constant at the transition can be related to the change of heat capacity. In order to derive the desired relations, one should follow the Landau theory of phase transitions whose main points are summarised below. The free energy density in terms of the order parameter η is

$$F = F_0 + \frac{1}{2}a(T)\eta^2 + \frac{1}{4}b\eta^4 + c(\nabla\eta)^2 + ... \tag{6.11}$$

In a system in which the order parameter is coupled to strain, the corresponding expression for the elastic constant for the two cases of bilinear and quadratic coupling is given by [118]

$$c_{ij} = c_{ij}^0 - \sum_{kl} \frac{\partial^2 F}{\partial\varepsilon_i \partial\eta_k} R_{kl} \frac{\partial^2 F}{\partial\varepsilon_j \partial\eta_l} \tag{6.12}$$

where R_{kl} is a matrix which satisfies [118]

$$\sum_{l} R_{kl} \frac{\partial^2 F}{\partial \eta_l \partial \eta_m} = \delta_{km} \tag{6.13}$$

where η_i is the order parameter component.

The formulation of the free energy using the partition function is given by

$$F = -k_B T \ln(Z) = -k_B T \ln \left(\sum_{n} e^{-\beta E_n} \right) \tag{6.14}$$

where E_n are the energy levels of the system. If there is only a single characteristic temperature scale T_C of the system, it is therefore possible to write the magnetic free energy in the following form

$$F_m = -T f(T/T_C) \tag{6.15}$$

Now, the elastic constant in one dimension given by the Eq. 6.12 can be expressed as

$$c = c_0 + \frac{d^2 F_m}{d\varepsilon^2} = c_0 - \left(\frac{dT_c}{d\varepsilon} \right)^2 \left(\frac{T}{T_C^2} \right) C_V^m = c_0 - \Omega^2 T C_V^m \tag{6.16}$$

where one can recognise the Grüneisen parameter

$$\Omega = -\frac{1}{T_C} \frac{\partial T_C}{\partial \varepsilon} \tag{6.17}$$

and C_V^m is magnetic specific heat

$$C_V^m = T \frac{\partial^2 F_m}{\partial T^2} \tag{6.18}$$

The derivation of the last step in the Eq. 6.18 is attached in the Appendix B.

In case of UGe_2, there are two temperature scales: T_C and T_x. It is therefore possible to write the following expression for the free energy of the system

$$F_m = -T \left[f(T/T_C) + g(T/T_x) \right] \tag{6.19}$$

based on the assumption that the partition function will be separable to give the two contributions in the above expression. Noting that, the elastic constant is now given by

$$c = c_0 - \Omega_x^2 T C_V^S - \Omega_C^2 T C_V^W \tag{6.20}$$

where

$$\Omega_x = -\frac{1}{T_x}\frac{\partial T_x}{\partial \varepsilon} \tag{6.21}$$

$$\Omega_C = -\frac{1}{T_C}\frac{\partial T_C}{\partial \varepsilon} \tag{6.22}$$

One can consider C_V^S and C_V^W to be Schottky–like and Weiss–like contributions to the magnetic specific heat capacity. The Schottky contribution for a two-level system is given by [119]

$$C_V^S = R\left(\frac{\Delta}{T}\right)^2 \frac{n_0 n_1 e^{\Delta/T}}{(n_1 + n_0 e^{\Delta/T})^2} \tag{6.23}$$

where n_0 and n_1 are the multiplicities of the ground and excited states. Whereas the Weiss contribution is [120]

$$C_V^W = -\frac{\gamma M_S}{\rho}\frac{\partial M_S}{\partial T} \tag{6.24}$$

where M_s is the sample magnetisation. Using the molecular field theory for ferromagnetism and with $J = 1/2$, it can be expressed by [120]

$$\frac{M_S}{M_M} = \tanh\left(\frac{\mu_m \gamma M_S}{k_B T}\right) \tag{6.25}$$

where M_M is the saturation magnetisation, γ is the molecular field constant (i.e. $H = H_{\text{applied}} + \gamma M$). The above expression is an implicit equation and must be solved numerically or graphically. It can be also written in terms of T_C as [120]

$$\frac{M_S}{M_M} = \tanh\left(\frac{T_C}{T}\frac{M_S}{M_M}\right) \tag{6.26}$$

Hence, using this equation it is possible to numerically calculate the heat capacity given by Eq. 6.28.

The magnetic specific heat is presented in Fig 6.18 (a) (taken from [116]).

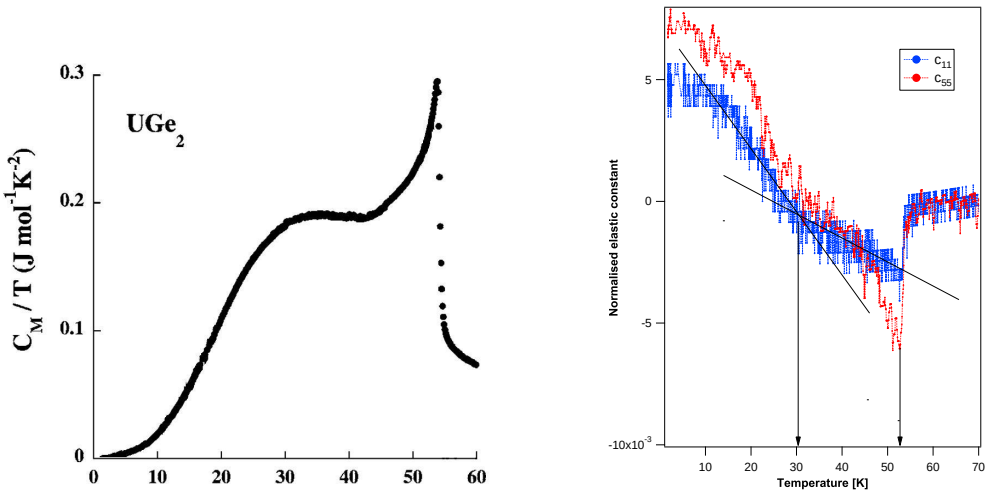

(a) (b)

Figure 6.15: **(a)** Magnetic heat capacity UGe_2 as calculated from neutron scattering data where phonon and electric contributions were subtracted. Adapted from [113]. **(b)** Normalised elastic constants c_{11} and c_{55} with the background subtracted. The arrows and lines are guide to the eye. The right arrow indicates T_C, the left arrow is associated with the cross-over temperature region on the phase diagram.

The peak at T_C is sharp and of Weiss–like type whereas the very broad feature associated with T_x is of Schottky–like type. The former may be attributed to the localised nature of $5f$-electrons and the latter to a crystal field splitting. In practice, the unusual broadening in the crystal field levels in uranium compounds makes it troublesome to detect experimentally with inelastic neutron scattering. (with a possible exception of URu_2Si_2 [121]). Furthermore, $5f$-electrons hybridise with the conduction electrons. Therefore, it must be noted that the above simple two-level model is an oversimplification. Nonetheless, Eq. 6.25 was used to model the elastic constant.

The Schottky–like contribution includes n_0 and n_1 which in the model were set to one (hence, the multiplicity is equal to one). The only free parameter in this contribution was Δ. As for the Weiss–like contribution, the T_C was fixed to be 53.0 K as measured experimentally. The constants in Eq. 6.28 are also known since they can be expressed in terms of the known magnetic moment of UGe_2. Hence, there was no free parameter in the Weiss–like contribution.

The expression for the elastic constant includes also the two Grüneisen parameter which were set free. Therefore, overall there were three free parameters in the model: Δ, Ω_C and Ω_x. The fit is presented in Fig. 6.16.

The values of the parameters obtained from the fit to the elastic constant c_{11} at ambient pressure were: $\Delta = 66.3 \pm 0.3\,\mathrm{K}$, $\Omega_x = 0.27 \pm 0.02$ and $\Omega_C = 6.74 \pm 0.07$. The value of Ω_C obtained from the fit can be compared with the value estimated from the definition of Ω_C. Recalling Eq. 6.25, one can write

$$\Omega_C = -\frac{1}{T_C}\left(\frac{\partial T_C}{\partial \varepsilon}\right)_P = \frac{1}{T_C}\left(\frac{\partial T_C}{\partial P}\right)_\varepsilon \left(\frac{\partial P}{\partial \varepsilon}\right)_{T_C} \tag{6.27}$$

where the cyclic relation for derivatives was used. The first derivative can be obtained by plotting T_C versus pressure as shown in Fig. 6.17 – it is the gradient of the tangent line to the dotted line at zero pressure. The second derivative is a definition of modulus of elasticity, E, evaluated at T_C. Assuming an isotropic and homogenous medium it can be equated to the bulk modulus, i.e. $E = c_B$. Hence,

$$\Omega_C = \frac{c_B}{T_C}\frac{\partial T_C}{\partial P} \tag{6.28}$$

The value of the bulk modulus can be estimated from the elastic constants obtained by neutron scattering at room temperature. The value of the bulk modulus T_C will be only 1-2% different than the value of bulk modulus at room temperature. Using the above equation, the estimated value was $|\Omega_C| = 4.7 \pm 0.7$ which is in a reasonable agreement with the value obtained from the fit. The modulus was introduced since Ω_C is squared in the Eq. 6.24. In fact it is negative due to negative change of T_C with respect to pressure. The value of Ω_x, is much smaller than Ω_C and is possibly underestimated. This result cannot be checked against the slope estimation since this a broad cross-over region on the phase diagram (i.e. no clear gradient of T_x with respect to pressure can be defined). It is also expected that this term should increase with the pressure increase since the cross-over region shrinks and eventually becomes the FM1-FM2 transition as pressure increases (i.e. gradient of T_x with respect to pressure can be evaluated).

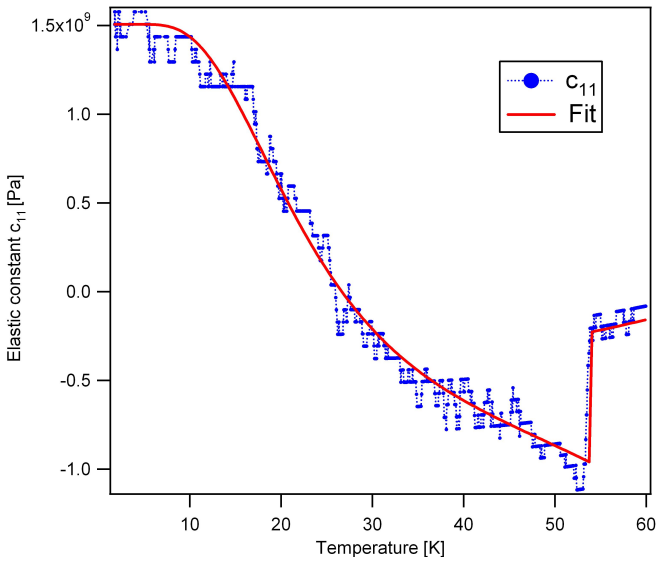

Figure 6.16: Elastic constant c_{11} (blue points) and a fit to the model described in the text (red line).

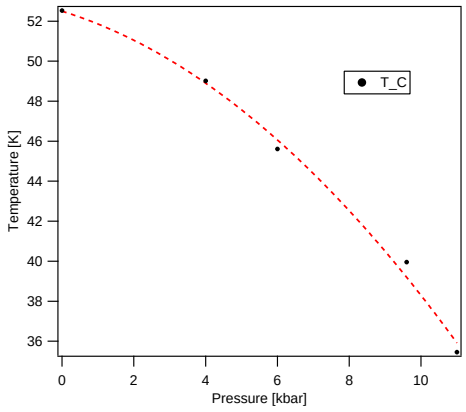

Figure 6.17: T_C as a function of pressure as obtained from the ultrasonic velocity measurements.

(3) Low Temperature Limit

At low temperatures it is possible, to estimate the effective electron mass by combining the ratio of the ultrasonic velocity to Fermi velocity. Quoting the results from Chapter 2, namely "the viscosity model", one can write using Eqs. 2.32 and 2.33

$$\frac{v_T}{v_F} = \frac{Nmq^2l}{5\rho\alpha_T} \tag{6.29}$$

and

$$\frac{v_L}{v_F} = \frac{4Nmq^2l}{15\rho\alpha_L} \tag{6.30}$$

for the transverse and longitudinal case respectively. One can estimate the Fermi velocity from the gradient of the critical field at high pressure (see Appendix C for more details). Using the data from the literature [122] and the measured values of the longitudinal and transverse velocities, the estimated ratios are

$$\frac{v_L}{v_F} = 0.81 \qquad \text{and} \qquad \frac{v_T}{v_F} = 0.59 \tag{6.31}$$

which is what one expects for a heavy fermion material for which $v_S/v_F \approx 1$ [63, 75]. The effective electron mass, m^*, can be expressed by rearranging Eq. 6.32

$$\frac{m^*}{m_e} = \frac{1}{m_e}\frac{15}{4}\frac{v_L}{v_F}\frac{\rho\alpha_L}{Nq^2l} \tag{6.32}$$

At the lowest temperature α_L and α_T were estimated to be 3.5×10^{-2} cm^{-1} and 1.9×10^{-2} cm^{-1} (in absolute units unlike the data in Fig. 6.12) . By estimating density ρ, number of electrons per unit volume N, and taking the ratio of velocities from above and mean free path l from literature [1], one obtains

$$m_L^* = 72.8m_e \qquad \text{and} \qquad m_T^* = 20.0m_e \tag{6.33}$$

where m_L^* and m_T^* refer to longitudinal and transverse values respectively. The first value seems to be overestimated, but the second value is closer to the experimentally measured effective mass at ambient pressure of $m^* \approx 12m_e$ [123].

6.4.2 High Pressures

A summary of high pressure steps is presented in Fig. 6.18. The elastic constant c_{11} as a function of temperature was measured at pressures of 4, 6, 9.5, 11 kbar respectively. The data in Fig. 6.18 were normalised with respect to the room temperature elastic constant at each pressure. The figure presents also the high temperature background fits which were described in the above section.

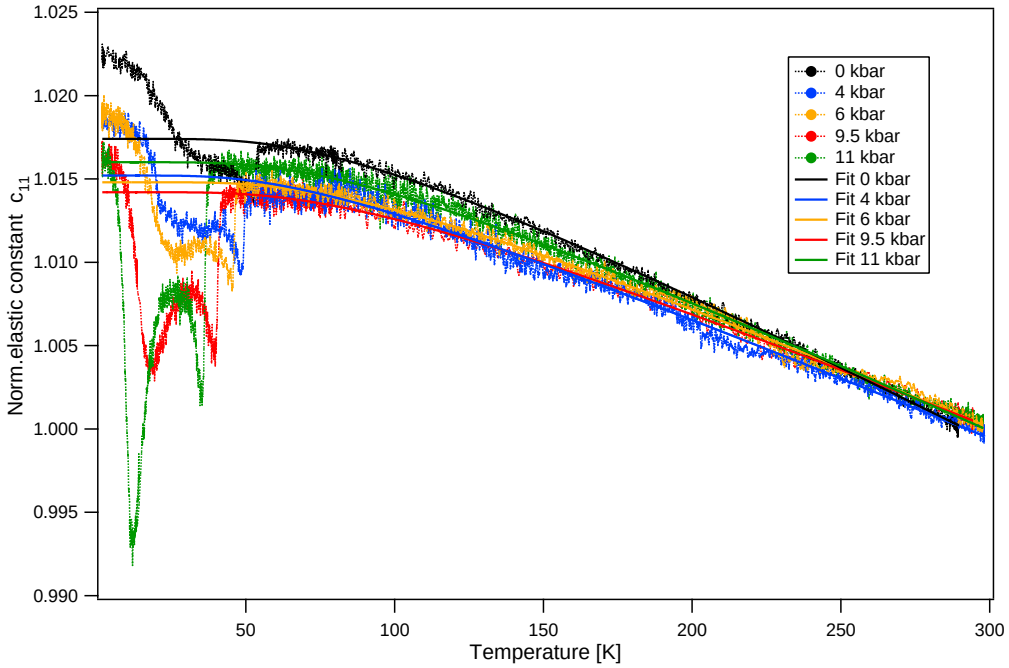

Figure 6.18: Temperature dependence of the elastic constant c_{11} at different pressure points (points) and the fits to the high temperature background (solid lines).The data was normalised with respect to the room temperature values at each pressure.

P [GPa]	T_C [K]	a [Pa]	b [K]	c [Pa]	$c_V\Gamma$ [$JK^{-1}m^{-3}$]
0	53	0.0204 ± 0.0002	245.11 ± 1.69	1.0161	1.66E-04
4	49	0.0163 ± 0.0002	214.93 ± 2.44	1.0150	1.52E-04
6	46	0.0194 ± 0.0002	252.48 ± 1.9	1.0149	1.54E-04
9.5	40.5	0.01862 ± 0.0003	252.57 ± 2.73	1.0142	1.47E-04
11	36	0.0202 ± 0.0002	243.9 ± 1.88	1.0160	1.66E-04

Table 6.3: Fitting parameters to the high temperature background of the normalised elastic constant c_{11} at different pressure points. Error in c is negligible.

As before, the high temperature background is due to the anharmonic phonon effect. The fitting parameters are summarised in Table 6.5. Parameters a, b, c are defined in Eq. 2.23. c is the value of the normalised elastic constant c_{11} at zero temperature. Parameters a and b control the slope of the linear part of the fits, Fig 6.17. Γ is the derivative of the Grüneisen parameter with respect to strain. The table presents $c_V\Gamma$, where c_V is the constant high temperature specific heat (see above discussion, Eqs. 6.7-6.10). No systematic trend is found in the parameters. Only parameters c and $c_V\Gamma$ decrease as pressure increases except the last pressure point, where they return to their ambient pressure value. More pressure steps are required to fully investigate the behaviour of the parameters.

Fig. 6.19 presents the data with the high temperature background subtracted. It can be clearly seen than application of pressure has three systematic effects. First, the drop at T_C is more pronounced with pressure and the value of T_C is supressed. Second, the broad feature associated with T_x is getting sharper and also more pronounced. All these results are consistent with the phase diagram. Third, the value of the elastic constant at zero temperature decreases to near zero with pressure increase.

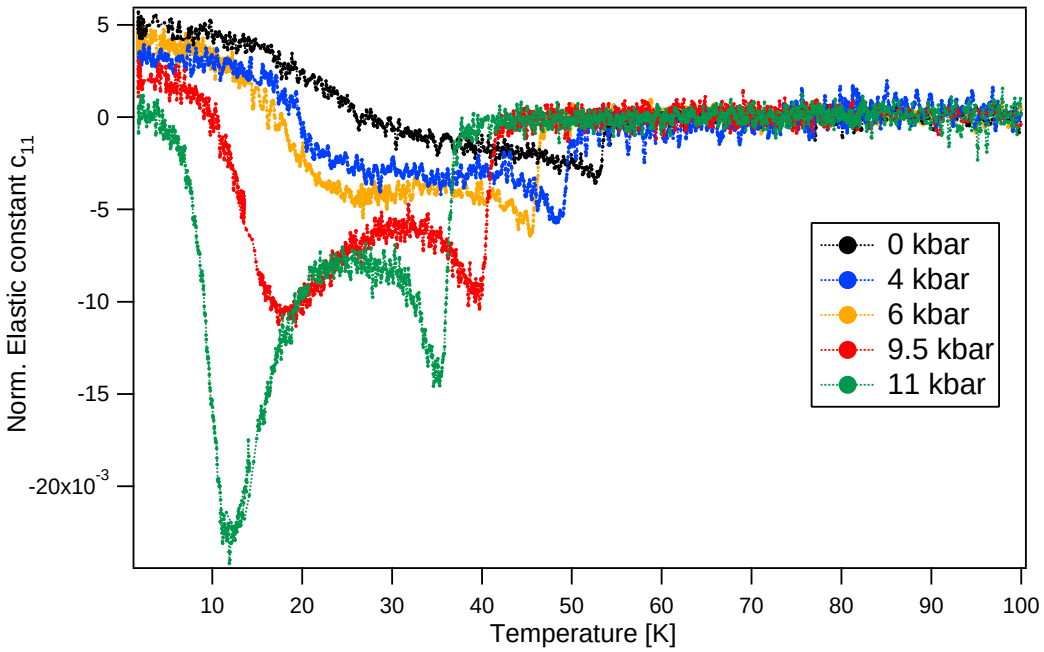

Figure 6.19: Temperature dependence of the elastic constant c_{11} at different pressure points with the high temperature background subtracted.

The ambient pressure model discussed above was used to fit the data at high pressures. The result of the fit is presented in Fig. 6.20. As can be seen, the model fits the data poorly. It was therefore decided to abandon the previous model and propose a new one.

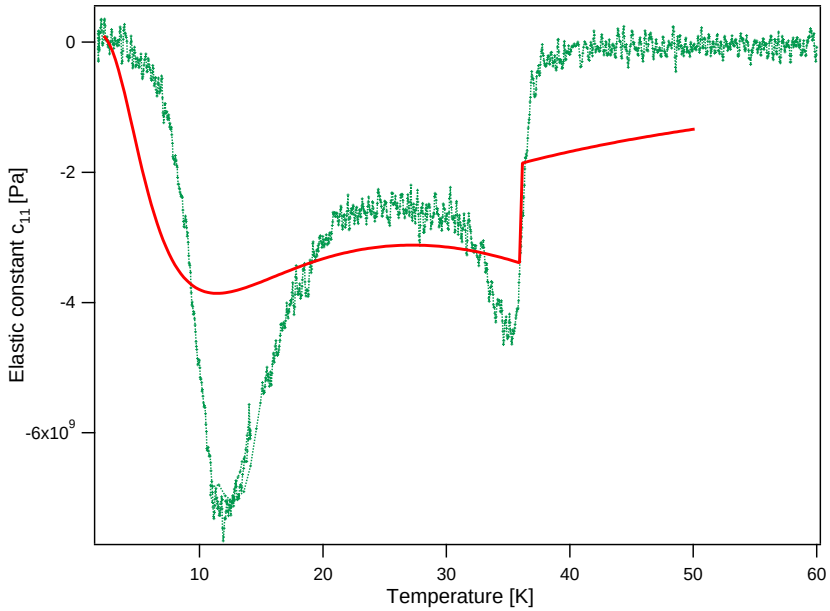

Figure 6.20: Elastic constant at 11 kbar. The solid line is the fit assuming the model used at ambient pressure.

Elastic Constant with Coupled Moments Model

As explained, UGe_2 exhibits two phases transitions at high pressures with two characteristic temperature scales T_x and T_C. These features might be a result of a two-component system in which the two components are coupled. In general the magnetic contribution to the Hamiltonian can be written as

$$\hat{H} = -H_1 m_1 - H_2 m_2 \tag{6.34}$$

where m_1 and m_2 are magnetic moments of the two components. H_1 and H_2 are appropriate exchange fields and can be written in terms of the two moments

$$H_1 = \lambda_{11} m_1 + \lambda_{12} m_2 \tag{6.35}$$

$$H_2 = \lambda_{21} m_1 + \lambda_{22} m_2 \tag{6.36}$$

where $\lambda_{12} = \lambda_{12}$. Now one can write the magnetic moments in terms of Boltzmann probability

$$m_1 = \frac{m_{s1}e^{-\beta H_1} - m_{s1}e^{-\beta H_1}}{e^{-\beta H_1} + e^{\beta H_1}} = m_{s1}\tanh(\beta H_1) \tag{6.37}$$

$$m_2 = \frac{m_{s2}e^{-\beta H_2} - m_{s2}e^{-\beta H_2}}{e^{-\beta H_2} + e^{\beta H_2}} = m_{s2}\tanh(\beta H_2) \tag{6.38}$$

where m_{s1} and m_{s2} are saturation moments. Hence, the coupled equations can be written in the functional form analogous to the expression coming from the Wiess model

$$m_1 = m_{s1}\tanh\left(\beta\lambda_{11}m_1 + \beta\lambda_{12}m_2\right) \tag{6.39}$$

$$m_2 = m_{s2}\tanh\left(\beta\lambda_{21}m_1 + \beta\lambda_{22}m_2\right) \tag{6.40}$$

changing variables yields

$$x_1 = \tanh\left(\Lambda_{11}x_1 + \Lambda_{12}x_2\right) \tag{6.41}$$

$$x_2 = \tanh\left(\Lambda_{21}x_1 + \Lambda_{22}x_2\right) \tag{6.42}$$

where $x = \frac{m}{m_s}$ and $\Lambda_{11} = \lambda_{11}m_{s1}^2$, $\Lambda_{12} = \lambda_{12}m_{s1}m_{s2}$ and $\Lambda_{22} = \lambda_{22}m_{s2}^2$ are appropriate parameters in units of temperature. Λ_{12} is the coupling term between the moments. In case of no coupling, Λ_{11} would be T_C and Λ_{22} would be T_x.

It is then necessary to derive the new expression for the heat capacity for the above system. By definition, the heat capacity at constant volume is given by

$$C_V = T\frac{dS}{dT} \tag{6.43}$$

Entropy for the above system can be written as

$$S = -k_B\left[\sum p_1\ln(p_1) + \sum p_2\ln(p_2)\right] \tag{6.44}$$

where the contributions come from the two moments, so

$$\begin{aligned}\frac{S}{k_B} = & -\frac{e^{-\beta H_1 m_{s1}}}{e^{-\beta H_1 m_{s1}}+e^{\beta H_1 m_{s1}}}\ln\left(\frac{e^{-\beta H_1 m_{s1}}}{e^{-\beta H_1 m_{s1}}+e^{\beta H_1 m_{s1}}}\right) \\ & -\frac{e^{\beta H_1 m_{s1}}}{e^{-\beta H_1 m_{s1}}+e^{\beta H_1 m_{s1}}}\ln\left(\frac{e^{\beta H_1 m_{s1}}}{e^{-\beta H_1 m_{s1}}+e^{\beta H_1 m_{s1}}}\right) \\ & -\frac{e^{-\beta H_2 m_{s2}}}{e^{-\beta H_2 m_{s2}}+e^{\beta H_2 m_{s2}}}\ln\left(\frac{e^{-\beta H_2 m_{s2}}}{e^{-\beta H_2 m_{s2}}+e^{\beta H_2 m_{s2}}}\right) \\ & -\frac{e^{\beta H_2 m_{s2}}}{e^{-\beta H_2 m_{s2}}+e^{\beta H_2 m_{s2}}}\ln\left(\frac{e^{\beta H_2 m_{s2}}}{e^{-\beta H_2 m_{s2}}+e^{\beta H_2 m_{s2}}}\right)\end{aligned} \tag{6.45}$$

Therefore, combining the above expression with Eqs. 6.37-38 and Eqs. 6.43-44, one can numerically solve the coupled equations and numerically differentiate entropy to obtain the heat capacity which will have two contributions coming from H_1 and H_2. Finally, the equation for the elastic constant is now given by

$$c = c_0 - \Omega_x^2 T C_V^{H_2} - \Omega_C^2 T C_V^{H_1} \tag{6.46}$$

Compared to the ambient pressure case, the high pressure model has five parameters: Λ_{11}, Λ_{12}, Λ_{22}, Ω_x and Ω_C. The two Grüneisen parameters are defined exactly in the same way as before. The results of the fits are presented in Fig. 6.21. Ambient pressure data were fitted again to the above model for the completeness of the results. The fitting parameters obtained at different pressure points are summarised in Table 6.3. The comparison between the values of Ω_C obtained from the fits and from the slope of the PM-FM line are summarised in Table 6.4.

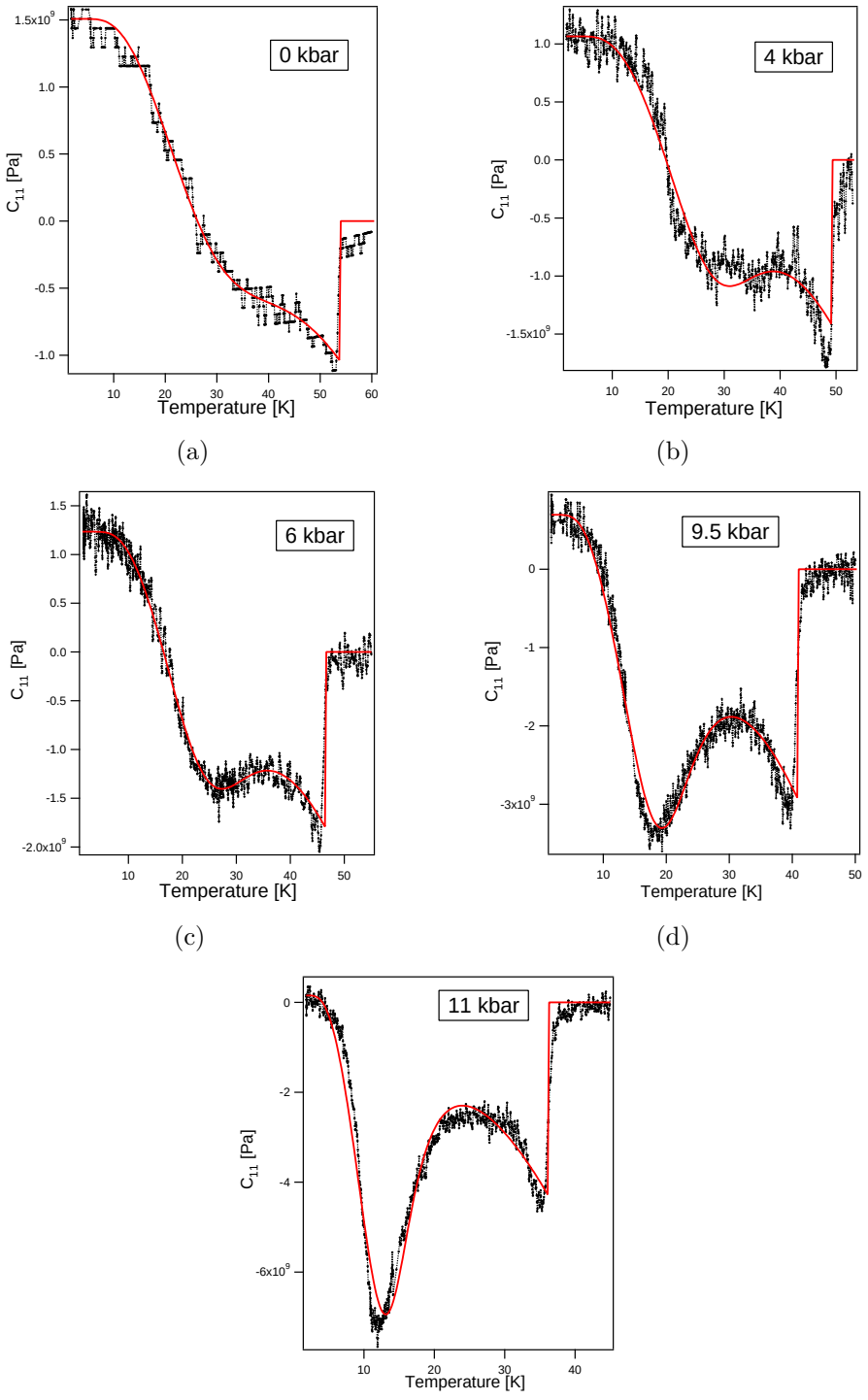

Figure 6.21: High pressure results. The solid line is the fit to the date with the model is described in the text. **(a)** 0 kbar, **(b)** 4 kbar, **(c)** 6 kbar, **(d)** 9.5 kbar, **(e)** 11 kbar. The background above T_C was set to zero for **(a-b)**. More details included in the text.

P [GPa]	Λ_{11} [K]	Λ_{12} [K]	Λ_{22} [K]	Ω_x	Ω_C
0	50±9	11.7±1.7	20 ± 2	9.51±0.48	4.67±0.70
4	48±6	6.7±0.6	21 ± 1	10.34±0.21	5.87±0.59
6	45±1	6.6±0.1	19 ± 1	12.25±0.25	6.14±0.12
9.5	40±1	4.0±0.1	15.9 ± 0.2	17.91±0.27	7.56±0.24
11	36±1	2.40±0.05	11.6 ± 0.2	28.99±0.29	9.21±0.10

Table 6.4: Fitting parameters to temperature dependence of the elastic constant. The parameters were obtained from the model described in the text.

P [GPa]	T_C [K]	dT_C/dP [K/GPa]	Ω_C from slope	Ω_C from fit	Discrepancy %
0	53.0	-0.4	0.73	4.67	541
4	49.0	-1.2	2.36	5.87	148
6	45.6	-1.6	3.38	6.14	81
9.5	40.0	-2.3	5.55	7.56	36
11	35.5	-2.6	7.06	9.21	30

Table 6.5: Comparison of the fitting parameters Ω_C obtained from the fits and from the slope of the PM-FM phase line in the phase diagram.

The systematic dependence of all fitting parameters can be clearly seen. As expected Λ_{11} and Λ_{22} decrease with pressure as they indicate the T_C and T_x. Also, the increase of Ω_C is consistent with the phase diagram of UGe_2, as the slope of PM-FM transition becomes steeper at higher pressures. The discrepancy of the values obtained from the fits with the values estimated from the slope become smaller indicating that the model is more reliable at higher pressures.

As for Ω_x, it cannot be compared to the value obtained with the slope of FM1-FM2 transition since the slope is only defined at p_x=1.25 GPa. However, using the point obtained from inelastic neutron scattering (p=1.2 GPa and corresponding T_x=8.5 K) and the point obtained from the ultrasonic measurements (p=1.2 GPa and corresponding T_x=8.5 K), $|\Delta T_x/\Delta P|$=35 K/GPa and the corresponding parameter is estimated to be Ω_x=280. This value is overestimated by an order of magnitude as compared to the value obtained from the fits of 28.99±0.29. Nonetheless, the overall pressure dependence of Ω_x is also consistent with the phase diagram. Its values are higher than Ω_C reflecting a more steeply sloped

line of the FM1-FM2 transition.

The pressure dependence of the coupling parameter is presented in Fig. 6.22. It indicates that the two components of the system become more decoupled as pressure increases. It can be predicated that this parameter will vanish at pressures between 12-14 kbar where the cross-over region between FM1 and FM2 becomes proper first order transition.

As already explained, the discrepancy in Table 6.5 demonstrates that the model was more reliable at higher pressures. Indeed, the model predicted correctly the value of the background above T_C, Fig. 6.21 (e). For the rest of the pressure points, the values above T_C were simply the equal to the elastic constant at zero temperature. This is because the systems of the coupled equations 6.39-6.40 used in the model returns zero values above T_C and hence the two terms involving heat capacities in Eq. 6.46 are simply zero (i.e. c=c_0). After the fits were done, the constant was subtracted from values above T_C. This is a main drawback of the model.

One possible solution would be to modify the high pressure model to include contributions similar to the ambient pressure model which predicted correctly the background above T_C, Fig 6.16. The final model should be a transition from the ambient pressure case to the 11kbar case including the features of both – the above results could be viewed as limiting cases of such a model (ambient pressure limit and high pressure limit).

Finally, the systematic effect in the measured and fitted data was a decrease of the elastic constant at zero temperature. Fig 6. shows pressure dependence of zero temperature elastic constant. If one assumes a free electron model then it can be shown that the bulk modulus of the electronic gas is directly proportional to the Fermi energy. The decrease of the elastic constant with pressure at lowest temperature would then indicate an increase in the effective mass which is consistent with previous observations [123].

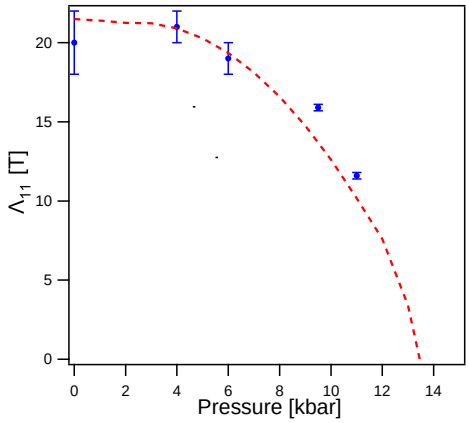

Figure 6.22: The pressure dependence of the parameter Λ_{12} indicating that at higher pressure the two components of the system become less strongly coupled. The dotted line is guide to eye.

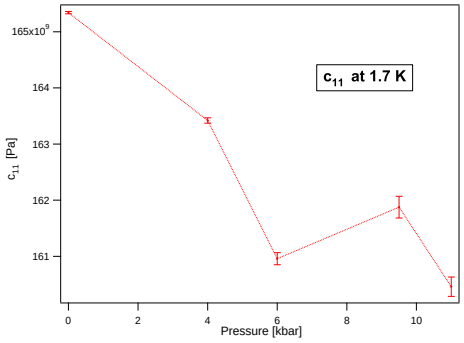

Figure 6.23: Pressure dependence of zero temperature elastic constant c_{11}.

6.4.3 Difficulties at High Pressures

Collecting data at high pressures proved to be a challenging process due to problems which can be categorised into the two main groups:

- **Signal Intensity**

  The intensity of the subsequent peaks in the raw spectrum was found to decrease on the pressure increase. At the highest pressure and low temperatures, only the first echo could be fitted and used to calculate the elastic constant. At room temperature three peak could be seen in the raw spectrum (Fig. 6.8), however the signal intensity drops as temperature decreases since the piezoelectric constant of the piezocrystal also decreases [124].

This is also why the ultrasonic attenuation coefficient could not be estimated at high pressures since it requires two peaks (first and second echoes) corresponding the same elastic constant. The effect of signal becoming weaker at high pressure could be an effect of pressure application on the piezocrystal which can have a potential effect on the efficiency of the ultrasound production. There was also one instance when signal was lost altogether at around 6 kbar despite no clear mechanical damage to the transducer was observed.

- **Pressure Cell Loading**

  The Piston Cylinder Cell used in the project was a prototype version designed by Christopher Ridley. Few modifications to the original design, including dropping the aluminium capsule design, were required before the cell was fully operational. The biggest problem was the piston failure which buckled on loading at around 10 kbar, Fig. 6.23. The copper beryllium piston was then replaced with the tungsten carbide one and allowed achieving higher pressures.

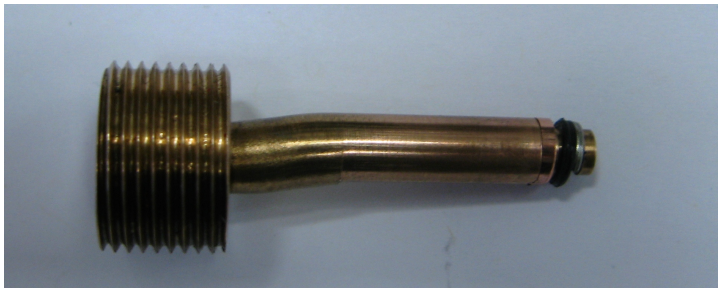

Figure 6.24: An example of a mechanical failure of the pressure cell setup. The piston was buckled on the pressure increase at around 10 kbar.

6.4.4 High Magnetic Fields

The difficulties described above caused a significant interruption to the progress of the project. The results at high fields were collected just before the end of the project and are not analysed. Fig. 6.23 presents the temperature dependence of the ultrasonic velocities corresponding to the elastic constant c_{11}. Application of the external field strongly suppresses the PM-FM transition at T_C. Suppression of the feature at T_x is much weaker and as the magnetic field increases the value of T_x decreases.

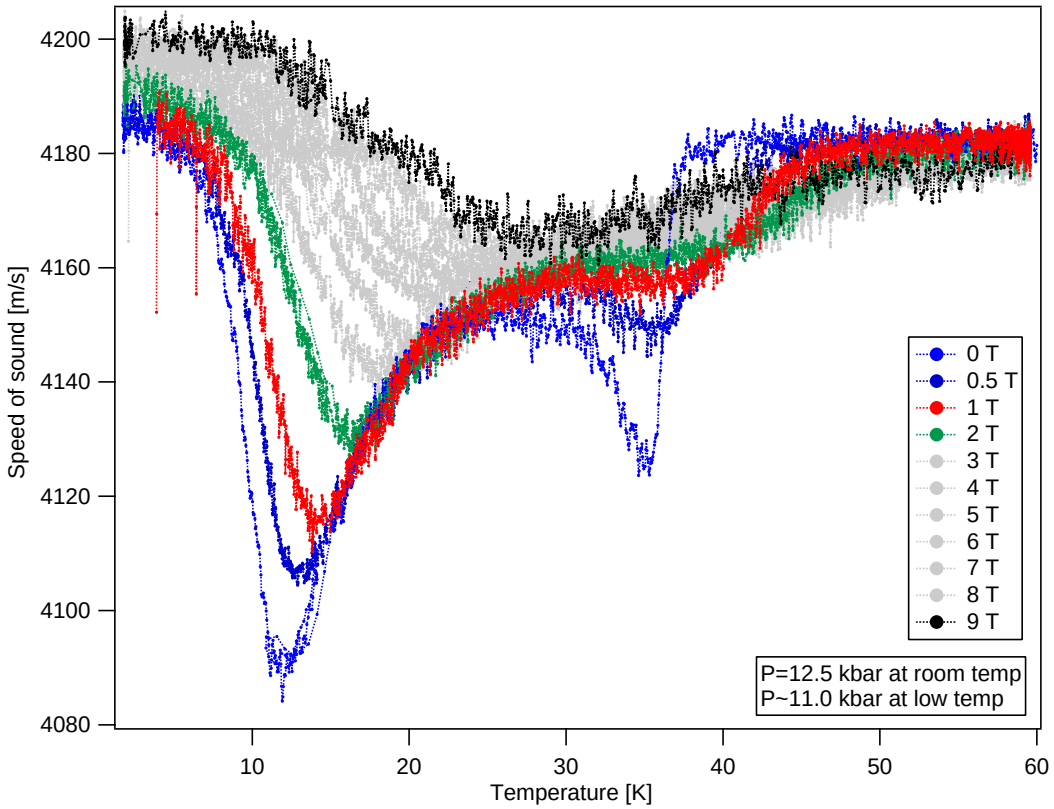

Figure 6.25: Temperature dependence of the speed of sound associated with c_{11} at 11 kbar in external magnetic field.

6.5 Conclusions and Future Work

Employing the pulse echo technique inside the piston cylinder cell to measure temperature dependence of the elastic constant was proven successful. The measured elastic constant c_{11} displays clear feature reflecting different parts of the phase diagram of UGe_2.

The measured temperature dependence of the elastic constant was modelled with two terms contributing to the magnetic heat capacity associated with two Grüneisen parameters Ω_x and Ω_C. The model assumed a coupling parameter between the two components. The rationale behind the model is that ordering of one component drives the splitting of energies for the second component (or more precisely the exchange field would cause the splitting). At ambient pressure, the two components are strongly coupled, with the largest value of Λ_{12}, and the system undergoes only one phase transition (PM-FM). At the highest obtained pressure point, with the smallest value of Λ_{12}, the second transition occurs and the two component are only weakly coupled. Such an interpretation would justify the claim that the FM1-FM2 transition is a change of electronic structure due to localised electrons which would also cause a change of local moment. The high field data presented above show that T_x is only weakly suppressed with applied field as compared to T_C. The field data could be fitted to deduce an effective moment and this could be compared with the jump in moment seen at T_x.

Finally, an unexpected finding is the evolution of the elastic constant at low temperatures (with a clear upturn above the subtracted background). At low temperatures, the electronic contribution to the elastic constant would be dominant. Similar behaviour at low temperatures was observed for some elastic constants in UPt_3 [125]. One could try using the deformation theory with coupling to the conduction electrons at low temperature to explain the experimental observations. This remains to be done in the future.

Chapter 7

Conclusions and Future Outlooks

The main goal of the thesis was to experimentally investigate the metamagnetic transition (FM1-FM2) in the ferromagnetic superconductor UGe_2. This transition is thought to play the key role in the unconventional superconductivity of UGe_2. The project provided more information about the nature of the transition (as summarized below) but its origin is still not fully understood.

The project could be divided into three main parts:

- **Neutron Inelastic Scattering**

  The neutron inelastic scattering results do not reveal fluctuations at the FM1-FM2 transition despite the fact that they were obtained at 12 kbar where this transition temperature is maximised. Only a small increase of scattering was observed at the vicinity of the transition. The increase was observed at the lowest energy transfer at the limit of the instrument resolution and hence any more detailed analysis is unviable. At the same pressure, the ferromagnetic fluctuations detected at T_C associated with the PM-FM transition exhibited non-Landau damping. This result was compared with the ambient pressure case and it was shown that the energy scale of the fluctuations was decreased at high pressure. The decrease can be explained by relating the fluctuation energy scale to the resistivity which is also decreased at high pressures. These findings would support recent theory by [112]. The absence of fluctuation at T_C must be interpreted carefully since the experiment was sensitive mostly to the $5f$-electrons and

would not detect the contribution of the conduction band being strongly suppressed by the magnetic form factor. Furthermore, the source of the small increase of the scattering near T_x si confined to very low energies and may indicate the presence of additional fluctuations below T_x.

- **Pulse Echo Technique at High Pressures**

  The measurements of elastic constant c_{11} at ambient and high pressures revealed clear features associated with the two transition, T_x and T_C. The temperature dependence of c_{11} resembled the temperature dependence of the magnetic part of the heat capacity. This observation helped providing two models explaining the results, one at ambient pressure and one at high pressures. The ambient pressure model included two types of magnetic heat capacity, Schottky–like and Wiess–like associated with the Ω_x and Ω_T parameters respectively. The values of parameters obtained from the fits could be compared with the values obtained from the gradients of the phase line on the UGe_2 phase diagram. They were found to be in agreement.

  The high pressure model included coupling between moments of the two-component system in which ordering of one component drives the splitting of energies for the second component. The behaviour of the fitting parameters (including the Ω_x and Ω_T) was consistent with the phase diagram of UGe_2 and explained important features of c_{11} with pressure increase. The features at T_C and T_x are more pronounced since the values of Ω_C and Ω_T increase with pressure since the gradients of the phase lines increase. However, the model predicted the background above T_C only for the highest pressure point. The future work should include the features of two models, ambient and high pressure to explain the intermediate pressure points.

  In addition to the above results, the Bordoni–like peaks in the ultrasonic attenuation coefficient were observed at ambient pressure. This observation does not contribute to the question of the nature of the FM1-FM2 but it might have a potential application serving as an indication of the quality of crystal mosaicity.

- **Instrumentation Development**

  The novel experimental technique, which involved mounting the transducer inside the pressure cell, made the pulse echo measurements possible. However, other instruments developed during the project open new possibilities. In particular, the 2-axis High Pressure Rotation Stage can be used to extend the phase diagram to pressure up to 5 GPa and magnetic fields up to 9 T together with the investigation of the angular dependence of transport measurements. This would allow probing the predicted wing-structure of the phase diagram [35] and also increase a chance of finding new quantum critical points. The 2-axis Rotation Stage can be also used to measure the angular dependence of resistivity in the vicinity of the FM1-FM2 transition.

  The High Pressure Resonant Technique was proved to be successful but the collected data show great complexity and require computer simulations to be analysed. The computer simulations are essential for data interpretation but are also very likely to help improving the experimental method itself (e.g. they might suggest different position of the transducers in the setup). This technique is the most challenging, both experimentally and in terms of data handling, but offers the most amount of information (several different modes can be measured at once). Finally, using this technique one can easily achieve temperature and pressure conditions (as demonstrated by the test results) required to probe the FM1-FM2 transition.

The future work would include the measurements of c_{11} at higher pressures in order to cross the FM1-FM2 transition. It should also include repeating the measurements at different ultrasonic frequencies in order to obtain ultrasonic attenuation coefficient as a function of temperature. Good quality measurements of the attenuation would provide a lot of insight on the transition since they can be related to the spin correlation function. Measurements at higher frequencies would require application of faster and more sensitive electronics (wave generator and oscilloscope). Further improvement in terms of data collection can include also low-noise filter and high frequency amplifiers which would provide a spectrum with more than one or two clear peaks.

APPENDIX A

Sound modes and corresponding elastic constants for an orthorhombic system. Adopted after [126] and [127].

Mode	**Propagation**	**Polarisation**	**Elastic Constant**
L	a [100]	[100]	c_{11}
T	a [100]	[010]	c_{66}
T	a [100]	[001]	c_{55}
T	b [010]	[100]	c_{66}
L	b [010]	[010]	c_{22}
T	b [010]	[001]	c_{44}
T	c [001]	[100]	c_{55}
T	c [001]	[010]	c_{44}
L	c [001]	[001]	c_{33}
QL	a–b	$\perp$[001]	c_{12}
QT	a–b	$\perp$[001]	c_{12}
T	a–b	[001]	c_{55} & c_{44}
QL	b–c	$\perp$[100]	c_{23}
QT	b–c	$\perp$[100]	c_{23}
T	b–c	[100]	c_{55} & c_{66}
QL	a–c	$\perp$[010]	c_{13}
QT	a–c	$\perp$[010]	c_{13}
T	a–c	[010]	c_{44} & c_{66}

Sound velocity–elastic constant ($v_S - c_{ij}$) relations corresponding to the above modes. Adopted after [126] and [127].

Mode	**Propagation**	**Polaristion**	$v_S - c_{ij}$ **relation**
L	a [100]	[100]	$c_{11} = \rho v_S^2$
T	a [100]	[010]	$c_{66} = \rho v_S^2$
T	a [100]	[001]	$c_{55} = \rho v_S^2$
T	b [010]	[100]	$c_{22} = \rho v_S^2$
L	b [010]	[010]	$c_{66} = \rho v_S^2$
T	b [010]	[001]	$c_{44} = \rho v_S^2$
T	c [001]	[100]	$c_{33} = \rho v_S^2$
T	c [001]	[010]	$c_{55} = \rho v_S^2$
L	c [001]	[001]	$c_{44} = \rho v_S^2$
QL	a–b	$\perp$[001]	$c_{12} = \sqrt{\frac{(c^2C_{11}+s^2C_{66}-\rho v_S^2)(c^2C_{66}+s^2C_{22}-\rho v_S^2)}{c^2s^2}} - C_{66}$
QT	a–b	$\perp$[001]	$c_{12} = \sqrt{\frac{(c^2C_{11}+s^2C_{66}-\rho v_S^2)(c^2C_{66}+s^2C_{22}-\rho v_S^2)}{c^2s^2}} - C_{66}$
T	a–b	[001]	$\rho v_S^2 = c^2C_{55} + s^2C_{44}$
QL	b–c	$\perp$[100]	$c_{23} = \sqrt{\frac{(c^2C_{22}+s^2C_{44}-\rho v_S^2)(c^2C_{44}+s^2C_{33}-\rho v_S^2)}{c^2s^2}} - C_{44}$
QT	b–c	$\perp$[100]	$c_{23} = \sqrt{\frac{(c^2C_{22}+s^2C_{44}-\rho v_S^2)(c^2C_{44}+s^2C_{33}-\rho v_S^2)}{c^2s^2}} - C_{44}$
T	b–c	[100]	$\rho v_S^2 = c^2C_{66} + s^2C_{55}$
QL	a–c	$\perp$[010]	$c_{13} = \sqrt{\frac{(s^2C_{11}+c^2C_{55}-\rho v_S^2)(s^2C_{55}+c^2C_{33}-\rho v_S^2)}{c^2s^2}} - C_{55}$
QT	a–c	$\perp$[010]	$c_{13} = \sqrt{\frac{(s^2C_{11}+c^2C_{55}-\rho v_S^2)(s^2C_{55}+c^2C_{33}-\rho v_S^2)}{c^2s^2}} - C_{55}$
T	a–c	[010]	$\rho v_S^2 = s^2C_{66} + c^2C_{44}$

where $s = \sin\theta$ and $c = \cos\theta$ and θ is the angle of rotation for the respective axis. More details can be found in [54].

APPENDIX B

For a system with a single characteristic energy scale T_C, the free energy can be written as

$$F = -Tf\left(\frac{T}{T_C}\right) \tag{1}$$

where $f(T/T_C)$ is some functional form defined by the partition function.

(A)

From (1), it follows that

$$\begin{aligned}\frac{\partial F}{\partial T} &= -f\left(\frac{T}{T_C}\right) - T\frac{\partial f}{\partial T} \\ &= -f(x) - \frac{T}{T_C}\frac{\partial f}{\partial x} \\ &= -f(x) - x\frac{\partial f}{\partial x}\end{aligned} \tag{2}$$

where $x = \frac{T}{T_C}$, so

$$\frac{\partial f}{\partial T} = \frac{1}{T_C}\frac{\partial f}{\partial x} \tag{3}$$

Differentiating with respect to temperature again yields

$$
\begin{aligned}
\frac{\partial^2 F}{\partial T^2} = & -\frac{\partial}{\partial T} f\left(\frac{T}{T_C}\right) - \frac{\partial}{\partial T}\left(T\frac{\partial f}{\partial T}\right) \\
= & -\frac{1}{T_C}\frac{\partial f}{\partial x} - \left[\frac{\partial T}{\partial T}\frac{\partial f}{\partial T} + T\frac{\partial}{\partial T}\left(\frac{\partial f}{\partial x}\frac{\partial x}{\partial T}\right)\right] \\
= & -\frac{1}{T_C}\frac{\partial f}{\partial x} - \frac{1}{T_C}\frac{\partial f}{\partial x} - \frac{T}{T_C}\frac{\partial}{\partial T}\left(\frac{\partial f}{\partial x}\right) \\
= & -\frac{1}{T_C}\frac{\partial f}{\partial x} - \frac{1}{T_C}\frac{\partial f}{\partial x} - \frac{T}{T_C^2}\left(\frac{\partial^2 f}{\partial x^2}\right) \\
= & \frac{1}{T_C}\left[-2\frac{\partial f}{\partial x} - x\frac{\partial^2 f}{\partial x^2}\right]
\end{aligned}
\tag{4}
$$

By definition, heat capacity at constant volume is given by

$$
\begin{aligned}
C_V = & T\frac{\partial^2 F}{\partial T^2} \\
= & \frac{T}{T_C}\left[-2\frac{\partial f}{\partial x} - x\frac{\partial^2 f}{\partial x^2}\right] \\
= & -2xf(x) - x^2\frac{\partial f}{\partial x}
\end{aligned}
\tag{5}
$$

(B)

From (2), it also follows that

$$
\begin{aligned}
\frac{\partial F}{\partial \varepsilon} = & -T\frac{\partial f}{\partial x}\frac{\partial x}{\partial T_C}\frac{\partial T_C}{\partial \varepsilon} \\
= & \frac{T^2}{T_C^2}\frac{\partial T_C}{\partial \varepsilon}\frac{\partial f}{\partial x} \\
= & x^2\frac{\partial T_C}{\partial \varepsilon}\frac{\partial f}{\partial x}
\end{aligned}
\tag{6}
$$

where $x = \frac{T}{T_C}$, so

$$
\frac{\partial x}{\partial \varepsilon} = \frac{\partial x}{\partial T_C}\frac{\partial T_C}{\partial \varepsilon} = -\frac{T}{T_C^2}\frac{\partial T_C}{\partial \varepsilon} \tag{7}
$$

therefore

$$
\frac{\partial f}{\partial \varepsilon} = \frac{\partial f}{\partial x}\frac{\partial x}{\partial \varepsilon} = -\frac{T}{T_C^2}\frac{\partial T_C}{\partial \varepsilon}\frac{\partial f}{\partial x} \tag{8}
$$

Differentiating with respect to strain again yields

$$\begin{aligned}\frac{\partial^2 F}{\partial \varepsilon^2} =& -\frac{T}{T_C^2}\left(\frac{\partial T_C}{\partial \varepsilon}\right)^2 \frac{\partial}{\partial x}\left(x^2 \frac{\partial f}{\partial x}\right) \\ =& \frac{T}{T_C^2}\left(\frac{\partial T_C}{\partial \varepsilon}\right)^2 \left[-2x\frac{\partial f}{\partial x} - x^2 \frac{\partial^2 f}{\partial x^2}\right]\end{aligned} \tag{9}$$

Therefore, using (5)

$$\frac{\partial^2 F}{\partial \varepsilon^2} = \frac{T}{T_C^2}\left(\frac{\partial T_C}{\partial \varepsilon}\right)^2 C_V = \Omega_C^2 T C_V \tag{10}$$

where

$$\Omega_C = -\frac{1}{T_C}\frac{\partial T_C}{\partial \varepsilon} \tag{11}$$

And finally, the elastic constant is given by

$$c = c_0 - \frac{\partial^2 F}{\partial \varepsilon^2} = c_0 - \Omega_C^2 T C_V \tag{12}$$

APPENDIX C

In order to estimate the effective mass using

$$\frac{v_T}{v_F} = \frac{Nmq^2l}{5\rho\alpha_T} \quad \text{or} \quad \frac{v_L}{v_F} = \frac{4Nmq^2l}{15\rho\alpha_L}$$

one needs to estimate v_F, N. q is the wavenumber of ultrasound specified in the experiment, l is the electron mean free path which can be taken from [1]. N is number of electrons per unit cell and ρ is mass density of UGe_2.

The BCS theory gives the coherence length (maximum extent of a Cooper pair) expressed as

$$\xi_0 = \frac{\hbar v_F}{\pi\Delta}$$

where the v_F is the Fermi velocity and Δ is the superconducting gap and can be expressed as

$$\Delta = 1.76 k_B T_C$$

rearranging for the Fermi velocity leads to

$$v_F = 1.76\pi k_B T_C \frac{\xi_o}{\hbar}$$

where the coherence length can be estimated from the slope of the critical field since

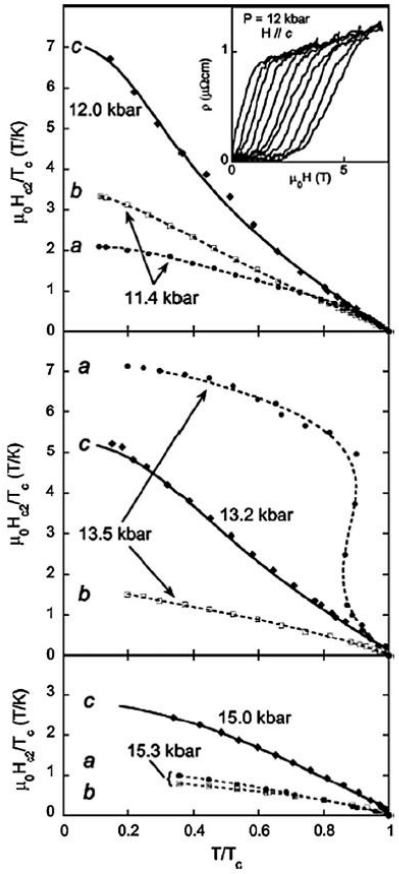

Figure 1: Upper critical field for UGe_2 at different pressures.

$$H_{c2} = \frac{\Phi_0}{2\pi\xi_0^2}\left(1 - \frac{T}{T_C}\right)$$

hence

$$-T_C \frac{dH_{c2}}{dT} \approx \frac{\Phi_0}{2\pi\xi_0^2}$$

The critical fields are presented below and are taken from [122]. Hence, it is possible to estimate ξ_0 and therefore v_F. The above expressions can be found in "Superconductivity, Superfluids and Condensates" by J. F. Annet (Oxford University Press, 2004).

Bibliography

[1] S. Saxena, P. Agarwal, K. Ahilan, F. Grosche, R. Haselwimmer, M. Steiner, E. Pugh, I. Walker, S. Julian, P. Monthoux, G. Lonzarich, A. Huxley, I. Sheikin, D. Braithweite, and J. Flouquet, "Superconductivity on the border of itinerant electron ferromagnetism in UGe2," *Nature*, vol. 406, pp. 587–592, 2000.

[2] H. K. Onnes, "Further experiments with liquid helium. G. On the electrical resistance of pure metals, etc. VI. On the sudden change in the rate at which the resistance of mercury disappears.," *Commun. Phys. Lab. Univ. Leiden*, no. 119b, 1911.

[3] G. Vidali, *Superconductivity: The Next Revolution?* Cambridge: Cambridge University Press, first edit ed., 1993.

[4] P. M. Grant, "Down the path of least resistance," *Physics World*, vol. 24, no. SUPERCONDUCTIVITY: The first 100 years., 2011.

[5] G. A. Saunders and P. J. Ford, *The Rise of the Superconductors.* CRC Press, first edit ed., 2004.

[6] J. G. Bednorz and K. A. Miiller, "Condensed Matt Possible High T c Superconductivity in the Ba - L a - C u - 0 System," *Z. Phys. B - Condensed Matter*, vol. 193, pp. 189–193, 1986.

[7] J. Annett, *Superconductivity, Superfluids and Condensates.* Oxford: Oxford University Press, 2004.

[8] A. Einstein, "Theoretische Bemerkungen zur Supraleitung der Metalle," *Het Natuurkundig Laboratorium der Rijksuniversiteit te Leiden in de Jaren 1904-1922*, vol. 429, 1922.

[9] S. Blundell, "The forgotten brothers," *Physics World*, no. SUPERCONDUCTIVITY: The first 100 years., 2011.

[10] V. Ginzburg and L. Landau, "On the theory of superconductivity," *Zh. Eksp. Teor. Fiz.*, vol. 36, 1959.

[11] J. Bardeen, L. N. Cooper, and J. R. Schrieffer, "Theory of superconductivity," *Physical Review Letters*, vol. 108, p. 1175, 1957.

[12] F. Steglich, J. Aarts, C. Bredl, W. Lieke, D. Meschede, W. Franz, and H. Schafer, "Superconductivity in the Presence of Strong Pauli Paramagnetism: CeCu2Si2," vol. 437, no. 25, pp. 1892–1896, 1979.

[13] F. Steglich, J. Arndt, O. Stockert, S. Friedemann, M. Brando, C. Klingner, C. Krellner, C. Geibel, S. Wirth, S. Kirchner, and Q. Si, "Magnetism, f-electron localization and superconductivity in 122-type heavy-fermion metals," *Journal of Physics: Condensed Matter*, vol. 24, p. 294201, 2012.

[14] R. Joynt and L. Taillefer, "The superconducting phases of UPt_ {3}," *Reviews of Modern Physics*, vol. 74, no. 1, pp. 235–294, 2002.

[15] G. R. Stewart, "Non-Fermi-liquid behavior in d- and f -electron metals," *Reviews of Modern Physics*, vol. 73, no. OCTOBER, pp. 797–854, 2001.

[16] P. Gegenwart, Q. Si, and F. Steglich, "Quantum criticality in heavy-fermion metals," *Nature Physics*, vol. 4, no. 3, pp. 186–197, 2008.

[17] J. R. Schrieffer and P. A. Wolff, "Relation between the Anderson and Kondo Hamiltonians," *Physical Review Letters*, vol. 149, no. 2, p. 491, 1966.

[18] E. Beaurepaire, H. Bulou, F. Scheurer, and K. Jean-Paul, *Magnetism and Synchrotron Radiation*. Springer-Verlag Berlin Heidelberg, 1 ed., 2010.

[19] B. Coqblin, C. Lacroix, M. a. Gusmão, and J. R. Iglesias, "Band-filling effects on the Kondo-lattice properties," *Physical Review B*, vol. 67, 2003.

[20] M. Vojta, "Quantum phase transitions," *Repts. Prog. Phys.*, vol. 66, no. 12, pp. 2069–2110, 2003.

[21] C. E. Olsen, "Magnetic Properties of Uranium Digermanide," *Journal of Applied Physics*, vol. 31, no. 5, p. S340, 1960.

[22] P. Boulet, A. Daoudi, M. Potel, H. Noel, G. Gross, G. Andre, and F. Bouree, "Crystal and magnetic structure of the uranium digermanide UGe2," *Journal of Alloys and Compounds*, vol. 247, no. 104-108, 1997.

[23] K. Oikawa, T. Kamiyama, H. Asano, Y. Onuki, and M. Kohgi, "Crystal Structure of UGe 2," *Journal of the Physical Society of Japan*, vol. 65, pp. 3229–3232, 1996.

[24] D. Aoki and J. Flouquet, "Superconductivity and Ferromagnetic Quantum Criticality in Uranium Compounds," *Journal of the Physical Society of Japan*, vol. 83, no. 6, p. 061011, 2014.

[25] Y. nuki, U. Isamu, W. Y. Sung, U. Izuru, S. Kazuhiko, T. Fukuhara, H. Sato, S. Takayanagi, M. Shikama, and A. Ochiai, "Magnetic and Electrical Properties of UGe Intermetallic Compounds," *Journal of the Physical Society of Japan*, vol. 61, no. 1, pp. 293–299, 1992.

[26] G. Oomi, K. Nishimura, Y. Onuki, and S. Yun, "Anomalous thermal expansion of single-crystalline UGe2," *Physica B: Condensed Matter*, vol. 186-188, pp. 758–760, 1993.

[27] A. B. Shick and W. E. Pickett, "Magnetism, spin-orbit coupling, and superconducting pairing in UGe2," *Physical Review Letters*, vol. 86, no. 2, pp. 300–303, 2001.

[28] A. Huxley, S. Raymond, and E. Ressouche, "Magnetic Excitations in the Ferromagnetic Superconductor UGe2," *Physical Review Letters*, vol. 91, no. 20, pp. 2–5, 2003.

[29] S. Raymond and a. Huxley, "Spin dynamics of the ferromagnetic superconductor UGe2," *Physica B: Condensed Matter*, vol. 350, no. 4, pp. 33–35, 2004.

[30] S. Sakarya, P. C. M. Gubbens, a. Yaouanc, P. Dalmas de Réotier, D. Andreica, a. Amato, U. Zimmermann, N. H. van Dijk, E. Brück, Y. Huang, and T. Gortenmulder, "Positive muon spin rotation and relaxation measurements on the ferromagnetic superconductor UGe_{2} at ambient and high pressure," *Physical Review B*, vol. 81, no. 2, pp. 1–19, 2010.

[31] H. Takahashi, N. Mori, Y. Onuki, and S. Yun, "Effect of pressure on magnetic ordering in UGe2," *Physica B: Condensed Matter*, vol. 186-188, pp. 772–774, 1993.

[32] G. Oomi, T. Kagayama, and Y. Onuki, "Critical electron scattering in UGe2 near the magnetic phase transition induced by pressure," *Journal of Alloys and Compounds*, vol. 271-273, pp. 482–485, 1998.

[33] V. Taufour, D. Aoki, G. Knebel, and J. Flouquet, "Tricritical point and wing structure in the itinerant ferromagnet UGe 2," *Physical Review Letters*, vol. 105, no. November, pp. 1–4, 2010.

[34] A. Huxley, E. Ressouche, B. Grenier, D. Aoki, J. Flouquet, and C. Pfleiderer, "The co-existence of superconductivity and ferromagnetism in actinide compounds," *Journal of Physics: Condensed Matter*, vol. 15, no. 28, pp. S1945–S1955, 2003.

[35] H. Kotegawa, V. Taufour, D. Aoki, G. Knebel, and J. Flouquet, "Evolution toward Quantum Critical End Point in UGe_2," p. 5, 2011.

[36] C. Pfleiderer and A. D. Huxley, "Pressure dependence of the magnetization in the ferromagnetic superconductor UGe2.," *Physical review letters*, vol. 89, no. 14, p. 147005, 2002.

[37] Y. Kitaoka, H. Kotegawa, a. Harada, S. Kawasaki, Y. Kawasaki, Y. Haga, E. Yamamoto, Y. nuki, K. M. Itoh, E. E. Haller, and H. Harima, "Ge-NQR study under high pressure," *Journal of Physics: Condensed Matter*, vol. 17, pp. S975–S986, 2005.

[38] K. Kuwahara, T. Sakai, M. Kohgi, Y. Haga, and Y. Onuki, "Elastic anomalies of UGe2," *Journal of Magnetism and Magnetic Materials*, vol. 310, no. 2, pp. 362–364, 2007.

[39] E. Stryjewski and N. Giordano, "Metamagnetism," *Advances in Physics*, vol. 26, no. 5, pp. 487–650, 1977.

[40] H. Yamada, "Metamagnetic transition and susceptibility maximum in an itinerant-electron system," *Physical Review B*, vol. 47, no. 17, pp. 11211–11219, 1993.

[41] T. Goto, Y. Shindo, H. Takahashi, and S. Ogawa, "Magnetic properties of the itinerant metamagnetic system Co(S1-xSex)2 under high magnetic fields and high pressure," *Physical Review B*, vol. 56, no. 21, pp. 14019–14028, 1997.

[42] K. G. Sandeman, G. G. Lonzarich, and A. J. Schofield, "Ferromagnetic superconductivity driven by changing Fermi surface topology.," *Physical review letters*, vol. 90, no. April, p. 167005, 2003.

[43] K. Kubo, "Ferromagnetism and Fermi surface transition in the periodic Anderson model: Second-order phase transition without symmetry breaking," *Physical Review B - Condensed Matter and Materials Physics*, vol. 87, no. 19, pp. 1–9, 2013.

[44] S. Watanabe and K. Miyake, "Coupled CDW and SDW Fluctuations as an Origin of Anomalous Properties of Ferromagnetic Superconductor UGe2," *Journal of the Physical Society of Japan*, vol. 71, no. 10, pp. 2489–2499, 2002.

[45] D. Fay and J. Appel, "Coexistence of p-wave superconductivity and itinerant ferromagnetism.," *Phys. Rev. B*, vol. 22, no. 7, p. 3173, 1980.

[46] C. Stock, D. A. Sokolov, P. Bourges, P. H. Tobash, K. Gofryk, F. Ronning, E. D. Bauer, K. C. Rule, and a. D. Huxley, "Anisotropic critical magnetic fluctuations in the ferromagnetic superconductor UCoGe," *Physical Review Letters*, vol. 107, no. 18, pp. 1–5, 2011.

[47] B. Luthi, "Elasticity," in *Physical Acoustics in the Solid State*, ch. 3, pp. 27–46, Berlin: Springer, 1 ed., 2005.

[48] G. Grimvall, "Elasticity. Basic Relations," in *Thermophysical Properties of Materials*, ch. 3, pp. 27–45, Elsevier, 1999.

[49] G. Grimvall, "Sound Waves," in *Thermophysical Properties of Materials*, ch. 5, pp. 70–78, Elsevier, 1999.

[50] G. Leibried and W. Ludwig, "Theory of Anharmonic Effects in Crystals," *Solid State Physics*, vol. 12, pp. 276–444, 1961.

[51] Y. Varshni, "Temperature Dependence of the Elastic Constants," *Physical Review B*, vol. 2, no. 10, pp. 3952–3958, 1970.

[52] J. S. Koehler, *Imperfections Nearly Perfect Crystals*. New York: John Wiley & Sons, 1952.

[53] A. Granato and K. Lücke, "Theory of mechanical damping due to dislocations," *Journal of Applied Physics*, vol. 27, no. 6, pp. 583–593, 1956.

[54] R. Truell, *Ultrasonic methods in solid state physics*. 1969.

[55] G. A. Alers and D. O. Thompson, "Dislocation contributions to the modulus and damping in copper at megacycle frequencies," *Journal of Applied Physics*, vol. 32, no. 2, pp. 283–293, 1961.

[56] D. J. Gunton and G. A. Saunders, "Bordoni peak formation as a result of a martensitic transformation," *Nature*, vol. 250, pp. 216–218, 1974.

[57] S. Levy and R. Truell, "Ultrasonic Attenuation in Magnetic Single Crystals," *Reviews of Modern Physics*, vol. 25, no. 1, 1953.

[58] B. Luthi, "Acoustic Waves in the Presence of Magnetic Ions," in *Physical Acoustics in the Solid State*, ch. 5, pp. 67–92, Berlin: Springer, 1 ed., 2005.

[59] B. Luthi, "Ultrasonics in Low Dimensional Spin and Electronic Peierls-Systems," in *Physical Acoustics in the Solid State*, ch. 12, pp. 289–325, Berlin: Springer, 1 ed., 2005.

[60] M. Divis, P. Lukac, and P. Svoboda, "Magnetoelastic interactions in the orthorhombic RECu2 compounds (RE identical to Tb, Dy, Ho, Er, Tm)," *Journal of Physics: Condensed Matter*, vol. 2, no. 37, pp. 7569–7573, 1990.

[61] P. Morin, J. Rouchy, and D. Schmitt, "Susceptibility formalism for magnetic and quadrupolar interactions in hexagonal and tetragonal rare-earth compounds," *Physical Review B*, vol. 37, no. 10, pp. 5401–5413, 1988.

[62] A. B. Bhatia, *used book Ultrasonic Absorption: An Introduction to the Theory of Sound Absorption and Dispersion in Gases, Liquids and Solids*. Oxford: Oxford University Press, 1967.

[63] C. Lupien, *Ultrasound Attenuation in the Unconventional Superconductor Sr2RuO4*. PhD thesis, University of Toronto, 2002.

[64] A. B. Pippard, "Theory of Ultrasonic Attenuation in Metals and Magneto-Acoustic Oscillations," *Proceedings of the Royal Society of London. Series A, Mathematical and Physical Sciences*, vol. 257, no. 1289, pp. 165–193, 1960.

[65] A. B. Pippard, "Ultrasonic attenuation in metals.," *Philosophical Magazine Series*, vol. 46, no. 381, pp. 1104–1114, 1955.

[66] G. Simon, "Propagation of Ultrasound in Ferromagnetic Metals at Low Temperatures," *Physical Review Letters*, vol. 128, no. 1, 1962.

[67] W. P. Mason, "Ultrasonic attenuation due to lattice-electron interaction in normal conducting metals," *Physical Review*, vol. 97, no. 2, pp. 557–558, 1955.

[68] F. S. Khan and P. B. Allen, "Sound attenuation by electrons in metals," *Physical Review B*, vol. 35, no. 3, pp. 1002–1019, 1987.

[69] C. Herring and C. Kittel, "On the Theory of Spin Waves in Ferromagnetic Media," *Physical Review*, vol. 81, no. 5, pp. 869–880, 1951.

[70] C. Kittel, "Interaction of Spin Waves and Ultrasonic Waves in Ferromagnetic Crystals," *Physical Review*, vol. 110, no. 4, pp. 836–841, 1958.

[71] B. Luthi, "Ultrasonics at Magnetic Phase Transitions," in *Physical Acoustics in the Solid State*, ch. 6, pp. 93–108, Berlin: Springer, 2005.

[72] K. Kawasaki and A. Ikushima, "Velocity of Sound in MnF2 near the Néel Temperature," *Physical Review B*, vol. 1, no. 7, pp. 3143–3151, 1970.

[73] B. Golding, "Ultrasonic propagation in RbMnF3 near the magnetic critical point," *Physical Review Letters*, vol. 20, no. 1, pp. 5–7, 1968.

[74] B. Luthi, "Magnetoacoustics in intermetallic f-electron systems," *Journal of Magnetism and Magnetic materials*, vol. 52, 1985.

[75] B. Luthi, "Unstable Moment Compounds," in *Physical Acoustics in the Solid State*, ch. 9.

[76] B. Luthi, "Experimental Techniques," in *Physical Acoustics in the Solid State*, ch. 2, pp. 5–26, Berlin: Springer, 1 ed., 2005.

[77] T. L. Jordan and Z. Ounaies, "Piezoelectric Ceramics Characterization," tech. rep., NASA, Hampton, Virginia, 2001.

[78] G. Li and J. R. Gladden, "High Temperature Resonant Ultrasound Spectroscopy: A Review," *International Journal of Spectroscopy*, vol. 2010, pp. 1–13, 2010.

[79] J. Maynard, "Resonant Ultrasound Spectroscopy," *Physics Today*, vol. 49, no. 1, p. 26, 1996.

[80] A. Jayaraman, "Ultrahigh pressures," *Review of Scientific Instruments*, vol. 57, no. 6, pp. 1013–1031, 1986.

[81] L. Dubrovinsky, N. Dubrovinskaia, V. B. Prakapenka, and A. M. Abakumov, "Implementation of micro-ball nanodiamond anvils for high-pressure studies above 6Mbar," *Nature Communications*, vol. 3, p. 1163, 2012.

[82] C. Ridley, M. Jacobsen, and K. Kamenev, "A finite-element study of sapphire anvils for increased sample volumes," *High Pressure Research*, no. May 2015, pp. 1–14, 2015.

[83] I. N. Goncharenko, "Neutron diffraction experiments in diamond and sapphire anvil cells," *High Pressure Research*, vol. 24, no. 1, pp. 193–204, 2004.

[84] I. R. Walker, "Nonmagnetic pistoncylinder pressure cell for use at 35 kbar and above," *Review of Scientific Instruments*, vol. 70, no. 8, p. 3402, 1999.

[85] L. H. Dmowski and E. Litwin-Staszewska, "The variation of the pressure coefficient of manganin sensors at low temperatures," *Measurement Science and Technology*, vol. 10, no. 5, pp. 343–347, 1999.

[86] M. Gauthier, D. Lheureux, F. Decremps, M. Fischer, J. P. Itié, G. Syfosse, and A. Polian, "High-pressure ultrasonic setup using the Paris-Edinburgh press: Elastic properties of single crystalline germanium up to 6 GPa," *Review of Scientific Instruments*, vol. 74, no. 8, pp. 3712–3716, 2003.

[87] S. D. Jacobsen, H. J. Reichmann, A. Kantor, and H. A. Spetzler, "A gigahertz ultrasonic interferometer for the diamond anvil cell and high-pressure elasticity of some iron-oxide minerals," *Advances in High-Pressure Techniques for Geophysical Applications*, pp. 25–48, 2005.

[88] O. F. Yagafarov, E. L. Gromnitskaya, a. G. Lyapin, and V. V. Brazhkin, "Elastic properties of fullerites C60 and C70 Under Pressure," *Journal of Physics: Conference Series*, vol. 215, p. 012054, 2010.

[89] H. J. Mueller, J. Lauterjung, F. R. Schilling, C. Lathe, and G. Nover, "Symmetric and asymmetric interferometric method for ultrasonic compressional and shear wave velocity measurements in piston-cylinder and multi-anvil high-pressure apparatus," *European Journal of Mineralogy*, vol. 14, no. 3, pp. 581–589, 2002.

[90] K. L. Darling, G. D. Gwanmesia, J. Kung, B. Li, and R. C. Liebermann, "Ultrasonic measurements of the sound velocities in polycrystalline San Carlos olivine in multi-anvil, high-pressure apparatus," *Physics of the Earth and Planetary Interiors*, vol. 143, no. 1-2, pp. 19–31, 2004.

[91] S. D. Jacobsen, H. Spetzler, H. J. Reichmann, and J. R. Smyth, "Shear waves in the diamond-anvil cell reveal pressure-induced instability in (Mg,Fe)O.," *Proceedings of the National Academy of Sciences of the United States of America*, vol. 101, no. 16, pp. 5867–5871, 2004.

[92] W. a. Bassett, H. J. Reichmann, R. J. Angel, H. Spetzler, and J. R. Smyth, "New diamond anvil cells for gigahertz ultrasonic interferometry and X-ray diffraction," *American Mineralogist*, vol. 85, no. 2, pp. 283–287, 2000.

[93] R. H. Webb and R. B. Griffiths, "Crystal Rotator for Cryostat," *Review of Scientific Instruments*, vol. 32, no. 3, p. 363, 1961.

[94] N. S. Selby, M. Crawford, L. Tracy, J. L. Reno, and W. Pan, "In situ biaxial rotation at low-temperatures in high magnetic fields," *Review of Scientific Instruments*, vol. 85, no. 9, p. 095116, 2014.

[95] R. Fanciulli, I. Cerjak, and J. L. Herek, "Low-noise rotating sample holder for ultrafast transient spectroscopy at cryogenic temperatures," *Review of Scientific Instruments*, vol. 78, no. 5, p. 053102, 2007.

[96] D. J. Wang, C. C. Chiu, and C. M. Cheng, "Design of a multi-axis cryogenic sample manipulator for soft X-ray and VUV spectroscopy," *Journal of Physics: Conference Series*, vol. 425, no. 12, p. 122007, 2013.

[97] D. M. Pajerowski and M. W. Meisel, "Magnetometer probe with low temperature rotation and optical fibers," *Journal of Physics: Conference Series*, vol. 150, no. 1, p. 012034, 2009.

[98] B. L. Blackford, M. H. Jericho, and M. G. Boudreau, "A vertical/horizontal two-dimensional piezoelectric driven inertial slider micropositioner for cryogenic applications," *Review of Scientific Instruments*, vol. 63, no. 4, p. 2206, 1992.

[99] CRYOGENIC LTD, "http://www.cryogenic.co.uk/products/rotating-sample-probes," 2015.

[100] JANIS COMPANY, "http://www.janis.com/CryogenicAccessories_KeySupplier.aspx," 2015.

[101] OXFORD INSTRUMENTS, "http://www.oxford-instruments.com/products/cryogenic-environments," 2015.

[102] J. M. Winey, Y. M. Gupta, and D. E. Hare, "R-Axis Sound Speed and Elastic Properties of Sapphire Single Crystals," *J. Appl. Phys.*, vol. 90, no. 6, pp. 3109–3111, 2001.

[103] D. G. Isaak, J. D. Carnes, and O. L. Anderson, "Elasticity of fused silica spheres under pressure using resonant ultrasound spectroscopy," *J. Acoust. Soc. Am.*, vol. 104, no. 4, pp. 2200–2206, 1998.

[104] I. Ohno, M. Kimura, Y. Hanayama, H. Oda, and I. Suzuki, "Pressure dependence of the elasticity of a steel sphere measured by the cavity resonance method," *The Journal of the Acoustical Society of America*, vol. 110, no. 2, p. 830, 2001.

[105] H. Zhang, R. S. Sorbello, C. Hucho, J. Herro, J. R. Feller, D. E. Beck, M. Levy, D. Isaak, J. D. Carnes, and O. Anderson, "Radiation impedance of resonant ultrasound spectroscopy modes in fused silica," *J. Acoust. Soc. Am.*, vol. 103, no. 5, pp. 2385–2394, 1998.

[106] F. Farzbod, "Resonant ultrasound spectroscopy for a sample with cantilever boundary condition using Rayleigh-Ritz method," *Journal of Applied Physics*, vol. 114, no. 2, p. 024902, 2013.

[107] B. J. Zadler, J. H. L. Le Rousseau, J. a. Scales, and M. L. Smith, "Resonant ultrasound spectroscopy: Theory and application," *Geophysical Journal International*, vol. 156, no. 1, pp. 154–169, 2004.

[108] G. Shirane, S. Shapiro, and J. Tranquada, *Neutron Scattering with a Triple-Axis Spectrometer*. Cambridge: Cambridge University Press, 2002.

[109] P. M. Chaikin and T. C. Lubensky, *Principles of Condensed Matter Physics*. Cambridge: Cambridge University Press, 2000.

[110] W. Wang, D. a. Sokolov, a. D. Huxley, and K. V. Kamenev, "Large volume high-pressure cell for inelastic neutron scattering," *Review of Scientific Instruments*, vol. 82, no. 7, 2011.

[111] A. Huxley, S. Raymond, and E. Ressouche, "Magnetic Excitations in the Ferromagentic Superconductor UGe2," *Physical Review Letters*, vol. 91, no. 20, pp. 2–5, 2003.

[112] A. V. Chubukov, J. J. Betouras, and D. V. Efremov, "Non-Landau damping of magnetic excitations in systems with localized and itinerant electrons," *Physical Review Letters*, vol. 112, no. 3, pp. 1–5, 2014.

[113] G. Shirane, O. Steinsvoll, Y. J. Uemura, and J. Wicksted, "DYNAMICS OF ITINERANT FERROMAGNETS ABOVE T//c.," *Journal of Applied Physics*, vol. 55, no. 6 pt 2A, pp. 1887–1892, 1983.

[114] N. Bernhoeft and G. Lonzarich, "Scattering of slow neutrons from long-wavelength magnetic fluctuations in UPt3," *Journal of Physics: Condensed Matter*, vol. 7, no. 37, p. 7325, 1995.

[115] G. Oomi, T. Kagayama, K. Nishimura, S. Yun, and Y. nuki, "Electrical resistivity of single crystalline UGe2 at high pressure and high magnetic field," *Physica B: Condensed Matter*, vol. 206-207, pp. 515–518, 1995.

[116] S. Raymond and a. Huxley, "Phonon spectrum of the ferromagnetic superconductor UGe2 and consequences for its specific heat," *Physical Review B - Condensed Matter and Materials Physics*, vol. 73, no. 9, pp. 1–5, 2006.

[117] A. Seeger, H. Donth, and F. Pfaff, "The mechanism of low temperature mechanical relaxation in deformed crystals," *Discussions of the Faraday Society*, vol. 23, p. 19, 1957.

[118] J. C. Slonczewski and H. Thomas, "Interaction of elastic strain with the structural transition of strontium titanate," *Physical Review B*, vol. 1, no. 9, pp. 3599–3608, 1970.

[119] S. Blundell and K. Blundell, *Concepts in Thermal Physics*. Oxford: Oxford University Press, 2006.

[120] D. H. Matrin, *Magnetism in Solids*. London: Iliffe Books LTD, 1967.

[121] C. Broholm and H. Lin, "Magnetic excitations in the heavy-fermion superconductor URu2Si2," *Physical Review B*, vol. 43, no. 16, 1991.

[122] A. Huxley, "Ferromagnetic Superconductors," *Physica C: Superconductivity and its Applications*, vol. 514, pp. 368–377, 2015.

[123] T. Terashima, T. Matsumoto, C. Terakura, S. Uji, N. Kimura, M. Endo, T. Komatsubara, and H. Aoki, "Evolution of quasiparticle properties in UGe(2) with hydrostatic pressure studied via the de Haas-van Alphen effect.," *Physical review letters*, vol. 87, no. 16, p. 166401, 2001.

[124] C. Miclea, C. Tnsoiu, L. Amarande, C. Miclea, C. Plviu, M. Cioangher, L. Trupina, C. Miclea, and C. David, "Effect of temperature on the main piezoelectric parameters of a soft PZT ceramic," *Romanian Journal of Information Science and Technology*, vol. 10, no. 3, pp. 243–250, 2007.

[125] M. Yoshizawa, B. Lüthi, and K. D. Schotte, "Grüneisen parameter coupling in heavy fermion systems," *Zeitschrift für Physik B Condensed Matter*, vol. 64, no. 2, pp. 169–174, 1986.

[126] G. Varughese and S. Kumar, "Measurement of Elastic Parameters of Lithium Hydroxylammonium Sulphate Single Crystal , by Ultrasonic Pulse Echo Overlap Technique," *Open Journal of Acoustics*, no. September, pp. 138–144, 2014.

[127] A. V. Alex, *Ultrasonic Measurements of the Elastic Constants of Selected Nonlinear Optical/Semiorganic Crystals with Orthorhombic Symmetry.* PhD thesis, Cochin University of Sceince and Technology, 2001.

Publications

M W Kepa, D A Sokolov, M Böhm and A D Huxley. Magnetic excitations in the ferromagnetic superconductor UGe_2 under pressure. In ***Phys.: Conf. Ser.*** **568**, 042016 (2014)

D Venkateshvaran, M Nikolka, A Sadhanala, V Lemaur, M Zelazny, M Kepa, M Hurhangee, A J Kronemeijer, V Pecunia, I Nasrallah, I Romanov, K Broch, I McCulloch, D Emin, Y Olivier, J Cornil, D Beljonne and H Sirringhaus. Approaching disorder-free transport in high-mobility conjugated polymers. In ***Nature***, **515**, 384−388 (2014)

Comment: The work from second publication was not used in the project and only the abstract of the paper is attached.

Journal of Physics: Conference Series **568** (2014) 042016 doi:10.1088/1742-6596/568/4/042016

Magnetic excitations in the ferromagnetic superconductor UGe_2 under pressure.

M W Kepa[1], D A Sokolov[1], M Böhm[2] and A D Huxley[1]

[1]SUPA, School of Physics and Astronomy, Centre for Science at Extreme Conditions, The University of Edinburgh, Mayfield Road, Edinburgh EH9 3JZ, UK
[2]Institut Laue-Langevin, BP 156, F-38042 Grenoble Cedex 9, France

E-mail: M.Kepa@sms.ed.ac.uk

Abstract. Ferromagnetism and superconductivity coexist in UGe_2 under pressures in the range of 10-16 kbar. Here, equal spin electrons are paired to give a spin triplet state but the pairing mechanism is still not verified experimentally. The work presented here attempts to verify whether the longitudinal magnetic fluctuations associated with a magnetic transition within the ferromagnetic state might be responsible for the electron pairing. We show that the energy scale of these fluctuations must be smaller than those associated with the second order phase transition at the Curie temperature. Furthermore, there is no significant change of the energy scale of the fluctuations at the Curie temperature as a function of pressure.

1. Introduction

UGe_2 is one of the most extensively studied ferromagnetic superconductors [1-7]. The magnetic properties of UGe_2 are due to the uranium $5f$ electrons. The crystal structure of the material is orthorhombic with the space group *Cmmm* [2]. The *a*-axis is the easy axis with an ordered magnetic moment $M_0 \approx 1.4\,\mu_B$ at zero temperature. The Curie temperature ($T_c = 53\,\mathrm{K}$ at ambient pressure) decreases with increasing pressure and is completely supressed at the critical pressure of $p_c = 16\,\mathrm{kbar}$ as shown on Fig. 1 [7]. This paramagnetic to ferromagnetic (PM-FM) transition is 2^{nd} order in nature at lower pressures but at the tricritical point (TCP) at $p_{TCP} = 14.1\,\mathrm{kbar}$, it changes to 1^{st} order [6]. Within the ferromagnetic region, there are two distinct ferromagnetic phases, the high temperature high pressure FM1 phase and the low temperature low pressure FM2 phase. At low pressures, there is a cross-over region between the two phases but at the critical end point (CEP), very close to 12 kbar, a 1^{st} order FM1-FM2 transition emerges where the ordered magnetic moment jumps from $M_0 \approx 0.9\,\mu_B$ (FM1 phase) to $M_0 \approx 1.4\,\mu_B$ (FM2 phase) [6]. Superconductivity appears only within the ferromagnetic state and the superconducting critical temperature is maximised at pressure of $p_x = 12\,\mathrm{kbar}$ with $T_{SC} \approx 0.8\,\mathrm{K}$ [2].

The superconducting pairing mechanism in UGe_2 is not yet fully understood. Theory suggested that magnetic fluctuations in the vicinity of a ferromagnetic phase transitions could induce the Cooper pairing with odd-parity resulting in spin triplet superconductivity [8]. It was also shown experimentally with the NMR spectroscopy in another uranium based ferromagnetic superconductor, UCoGe, that longitudinal spin fluctuations might be responsible for spin triplet superconductivity [9]. The work we present here attempts to verify using inelastic neutron

scattering (as a direct probe) whether the longitudinal magnetic fluctuations in UGe_2 are responsible for unconventional superconductivity.

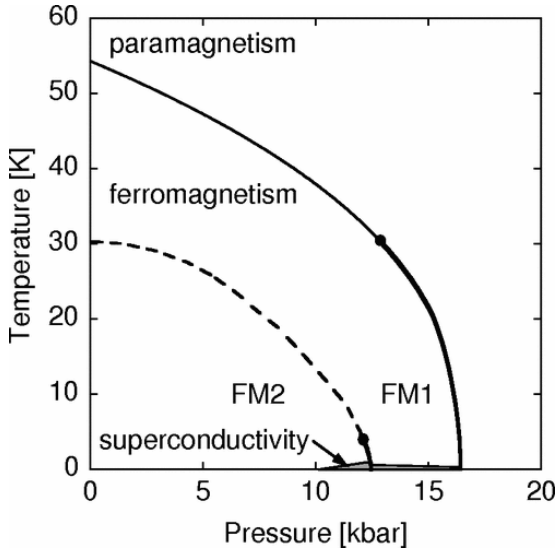

Fig. 1: The schematic space phase diagram of UGe_2 [7]. The paramagnetic to ferromagnetic phase line is second order at low pressures (thin line) and first order at higher pressures (thick line). The dashed line indicates the crossover region between FM1 and FM2 phases. Solid thick line between FM1 and FM2 is first order. The shaded region is the region of superconductivity with the maximal critical temperature of $T_{SC} \approx 0.8\,\mathrm{K}$. Dots indciate the critical points.

2. Experiment

The sample used in the experiment was a single crystal grown by the Czochralski technique. The sample was spark cut to the dimensions of $6.1{\times}3.4{\times}4.0\,\mathrm{mm}$. The electrical resistivity was measured at ambient pressure using the four-point method with a lock-in amplifier and is presented on Fig. 2(a). The clear drop of resistivity indicates the PM-FM transition at $T_c = 53\,\mathrm{K}$. The value of the residual resistivity ratio (RRR) was 62.

The pressure cell used in the experiment was the large volume two-layered piston-cylinder pressure cell described in [10]. The cell combines a large sample volume with a safe operating pressure limit of 18 kbar and was optimised for inelastic neutron scattering experiments [10]. Pressure inside the cell at low temperature was determineted to be 11.8 kbar using the established phase diagram of UGe_2, Fig. 1. The measured crystal parameters at that pressure were: $b = 14.968\,\text{Å}$ and $c = 4.100\,\text{Å}$. The rocking curve, Fig. 2(b), taken through $Q = 2\pi(0, 0, 1)/c$ at the same pressure gave the mosaic of 1.3°. This value of Q was chosen since this Bragg peak is almost entirely magnetic due to very small nuclear contribution.

To obtain elastic and inelastic neutron scattering data we used the triple axis spectrometer IN14 at the Institut Laue-Langevin (ILL). For measurements at low temperatures, the cell was loaded in the ILL orange cryostat with a base temperature of 1.5 K. The inelastic data points were taken on $Q = 2\pi(0, 0, 1.04)/c$ at different temperatures at two energy transfers of 0.15 meV and 0.25 meV. A cool beryllium filter was placed on the incident momentum side. We used a neutron beam with fixed final momentum $k_f = 1.3\,\text{Å}^{-1}$. The energy resolution was determined from the incoherent scattering with $Q = 2\pi(0, 0.4, 1.04)/c$ and had a full width at half maximum (FWHM) of 0.10 meV. We used W-configuration as a setup geometry and a PG (002) analyser with horizontal and vertical focusing. The temperature was measured using a Cernox thermometer which was mounted at the end of the probe very close to the

pressure cell. The neutron scattering intensity of the elastic scan taken on $Q = 2\pi(0,0,1)/c$ is proportional to the square of magnetisation and clearly showed the two transitions: first, PM-FM with $T_C = 33.5 \pm 0.5\,\mathrm{K}$; and second, FM1-FM2 with $T_x = 8.5 \pm 0.5\,\mathrm{K}$, Fig. 3. An increase of inelastic scattering intensity is observed at $T_C = 33.5 \pm 0.5\,\mathrm{K}$ at energy transfer of 0.15 meV. This increase is due fluctuations associated with the second order PM-FM transition. The intensity of inelastic scattering (relative to background) decreases at higher energy transfer, Fig. 3. The data do not show any significant increase of scattering intensity at $T_x = 8.5 \pm 0.5\,\mathrm{K}$.

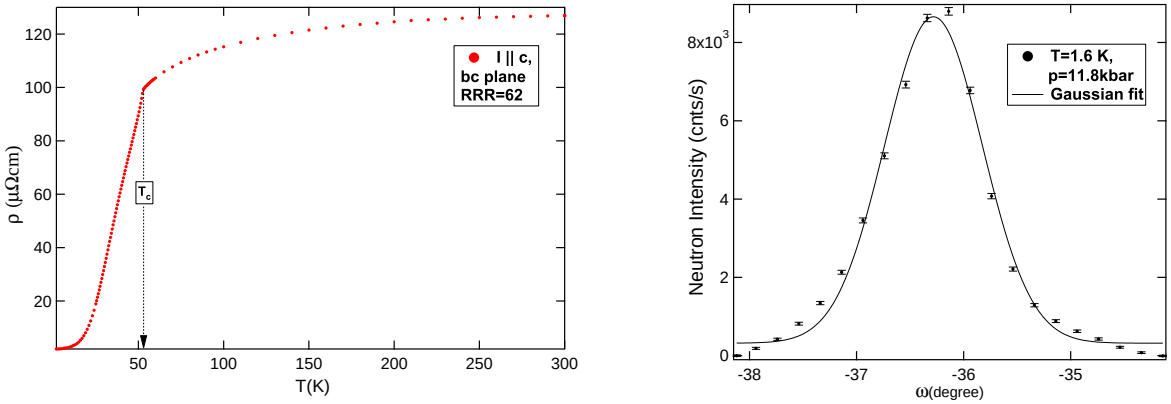

(a) **(b)**

Fig. 2: **(a)** Resistivity of UGe_2 at ambient pressure with current along c-axis within bc-plane. The PM-FM transition is observed at $T_c = 53\,\mathrm{K}$. **(b)** The rocking curve taken at $p = 11.8\,\mathrm{kbar}$ on $Q = 2\pi(0,0,1)/c$ at $T = 1.6\,\mathrm{K}$ (background subtracted). Solid line is the Gaussian fit to the data. The measured mosaic was 1.3° at FWHM.

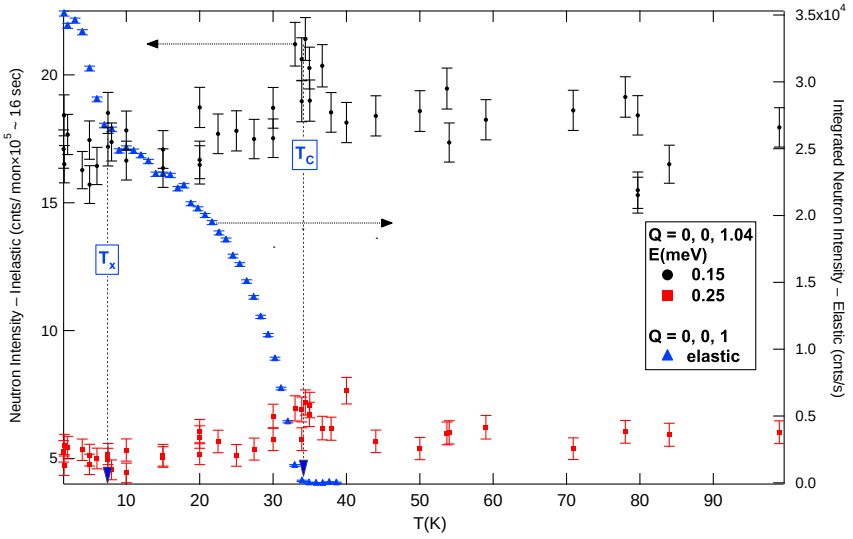

Fig. 3: Right axis shows elastic scattering points (▲) taken at $Q = 2\pi(0,0,1)/c$ and at $p = 11.8\,\mathrm{kbar}$. Two phase are clearly seen: PM-FM with $T_C = 33.5 \pm 0.5\,\mathrm{K}$; and FM1-FM2 with $T_x = 8.5 \pm 0.5\,\mathrm{K}$. Left axis shows inelastic scattering points at $Q = 2\pi(0,0,1.04)/c$ and at $p = 11.8\,\mathrm{kbar}$ with two different energy transfers of 0.15 meV (●) and 0.25 meV (■).

3. Conclusion and future outlooks

The work presented here does not reveal ferromagnetic spin fluctuations at T_x associated with the FM1-FM2 transition. Instead, we observed fluctuations at T_C associated with the PM-FM transition. Furthermore, the energy scale of the fluctuations at T_C at high pressure is similar to the energy scale at ambient pressure where there is no superconductivity [7]. This might suggest that the fluctuations at T_C are unlikely to play a significant role in inducing superconductivity. On the other hand, the previous results [7, 11-12] show that the $5f$ electron still contribute to most of the differential susceptibility and are responsible for most of bulk magnetic properties at the temperature and pressure conditions similar to those presented in our work. However, it was also suggested by the muon spin spectroscopy measurements [12] that the FM1-FM2 transition might be due to conduction electrons which would not be detected in our experiment. The inelastic scattering from the conduction electrons is strongly suppressed by the magnetic form factor and cannot be measured in the standard three-axis geometry. More work is required to fully study the magnetisation fluctuations from components due to other orbitals and to understand their role in forming superconductivity.

4. Acknowledgments

We would like to acknowledge EPSRC for financial support (Grant Number EP/E063985/1).

[1] Saxena S S *et al.* 2000 *Nature* **406** 587–592
[2] Huxley A D *et al.* 2001 *Phys. Rev.* B **63** 144519
[3] Hardy F, Meingast C, Taufour V, Flouquet J, v. Lohneysen H, Fisher R A, Phillips N E, Huxley A D and Lashley J C 2009 *Phys. Rev.* B **80** 174521
[4] Guritanu V, Armitage N P, Tediosi R, Saxena S S, Huxley A D and van der Marel D 2008 *Phys. Rev.* B **78** 172406
[5] Sokolov D A, Ritz R, Pfleiderer C, Keller T and Huxley A D 2011 *J. Phys.: Conf. Ser.* **273** 012085
[6] Taufour V, Aoki D, Knebel G and Flouquet J 2010 *Phys. Rev. Lett.* **105** 217201
[7] Huxley A D, Raymond S and Ressouche E 2003 *Phys. Rev. Lett.* **91** 207201
[8] Fay D and Appel J 1980 *Phys. Rev. Lett.* B **22** 3173
[9] Hattori T *et al.* 2012 *Phys. Rev. Lett.* **108** 066403
[10] Wang W, Sokolov D A, Huxley A D and Kamenev K V 2011 *Rev. Sci. Instrum.* **82** 073903
[11] Pfleiderer C and Huxley A D 2002 *Phys. Rev. Lett.* **89** 147005
[12] Sakarya S *et al.* 2010 *Phys. Rev.* B **81** 024429

NATURE | **LETTER**

日本語要約

Approaching disorder-free transport in high-mobility conjugated polymers

Deepak Venkateshvaran, Mark Nikolka, Aditya Sadhanala, Vincent Lemaur, Mateusz Zelazny, Michal Kepa, Michael Hurhangee, Auke Jisk Kronemeijer, Vincenzo Pecunia, Iyad Nasrallah, Igor Romanov, Katharina Broch, Iain McCulloch, David Emin, Yoann Olivier, Jerome Cornil, David Beljonne & Henning Sirringhaus

Nature **515**, 384–388 (20 November 2014) doi:10.1038/nature13854
Received 25 July 2014 Accepted 08 September 2014 Published online 05 November 2014

Print

Conjugated polymers enable the production of flexible semiconductor devices that can be processed from solution at low temperatures. Over the past 25 years, device performance has improved greatly as a wide variety of molecular structures have been studied[1]. However, one major limitation has not been overcome; transport properties in polymer films are still limited by pervasive conformational and energetic disorder[2, 3, 4, 5]. This not only limits the rational design of materials with higher performance, but also prevents the study of physical phenomena associated with an extended π-electron delocalization along the polymer backbone. Here we report a comparative transport study of several high-mobility conjugated polymers by field-effect-modulated Seebeck, transistor and sub-bandgap optical absorption measurements. We show that in several of these polymers, most notably in a recently reported, indacenodithiophene-based donor–acceptor copolymer with a near-amorphous microstructure[6], the charge transport properties approach intrinsic disorder-free limits at which all molecular sites are thermally accessible. Molecular dynamics simulations identify the origin of this long sought-after regime as a planar, torsion-free backbone conformation that is surprisingly resilient to side-chain disorder. Our results provide molecular-design guidelines for 'disorder-free' conjugated polymers.

View full text

Subject terms: Molecular electronics Electronic devices Conjugated polymers Electronic and spintronic devices

References

1. Bruetting, W. *Physics of Organic Semiconductors* (Wiley-VCH, 2005)
2. Bässler, H. Localized states and electronic transport in single component organic solids with diagonal disorder. *Phys. Stat. Solidi B* **107**, 9–54 (1981)
3. Sirringhaus, H. Device physics of solution-processed organic field-effect transistors. *Adv. Mater.* **17**, 2411–2425 (2005)
4. Rivnay, J. *et al.* Structural origin of gap states in semicrystalline polymers and the implications for charge transport. *Phys. Rev. B* **83**, 121306 (2011)
5. Noriega, R. *et al.* A general relationship between disorder, aggregation and charge transport in conjugated polymers. *Nature Mater.* **12**, 1038–1044 (2013)
6. Zhang, W. M. *et al.* Indacenodithiophene semiconducting polymers for high performance air-stable transistors. *J. Am. Chem. Soc.* **132**, 11437–11439 (2010)
7. Nielsen, C. B., Turbiez, M. & McCulloch, I. Recent advances in the development of semiconducting DPP-containing polymers for transistor applications. *Adv. Mater.* **25**, 1859–1880 (2013)
8. Kim, N.-K. *et al.* Solution-processed barium salts as charge injection layers for high performance N-channel organic field-effect transistors. *ACS Appl. Mater. Interfaces* **6**, 9614–9621 (2014)
9. Kim, G. *et al.* A thienoisoindigo-naphthalene polymer with ultrahigh mobility of 14.4 cm^2/V s that substantially exceeds benchmark values for amorphous silicon semiconductors. *J. Am. Chem. Soc.* **136**, 9477–9483 (2014)
10. Tseng, H.-R. *et al.* High-mobility field-effect transistors fabricated with macroscopic aligned semiconducting polymers. *Adv. Mater.* **26**, 2993–2998 (2014)
11. Callen, H. B. *Thermodynamics* Ch. 17 (Wiley, 1960)
12. Emin, D. Seebeck effect. In *Wiley Encyclopedia of Electrical and Electronics Engineering Online* (ed. Webster, J. G.) (Wiley, 2013)
13. Emin, D. Enhanced Seebeck coefficient from carrier-induced vibrational softening. *Phys. Rev. B* **59**, 6205–6210 (1999)
14. Emin, D. *Polarons* (Cambridge Univ. Press, 2013)
15. Pernstich, K. P., Roessner, B. & Batlogg, B. Field-effect-modulated Seebeck coefficient in organic semiconductors. *Nature Mater.* **7**, 321–325

(2008)

16. Kronemeijer, A. J. *et al.* A selenophene-based low-bandgap donor–acceptor polymer leading to fast ambipolar logic. *Adv. Mater.* **24**, 1558–1565 (2012)
17. Kronemeijer, A. J. *et al.* Two-dimensional carrier distribution in top-gate polymer field-effect transistors: correlation between width of density of localized states and Urbach energy. *Adv. Mater.* **26**, 728–733 (2014)
18. Chen, Z. *et al.* High performance ambipolar diketopyrrolopyrrole-thieno[3,2-b]thiophene copolymer field-effect transistors with balanced electron and hole mobilities. *Adv. Mater.* **24**, 647–652 (2012)
19. Li, J. *et al.* A stable solution-processed polymer semiconductor with record high mobility for printed transistors. *Sci. Rep.* **2**, 754 (2012)
20. Zhang, X. *et al.* Molecular origin of high field-effect mobility in an indacenodithiophene–benzothiadiazole copolymer. *Nature Commun.* **4**, 2238 (2013)
21. Sirringhaus, H. Organic field-effect transistors — the path beyond amorphous silicon. *Adv. Mater.* **26**, 1319–1335 (2014)
22. Brondijk, J. J. *et al.* Two-dimensional charge transport in disordered organic semiconductors. *Phys. Rev. Lett.* **109**, 056601 (2012)
23. Venkateshvaran, D., Kronemeijer, A. J., Moriarty, J., Emin, D. & Sirringhaus, H. Field-effect modulated Seebeck coefficient measurements in an organic polymer using a microfabricated on-chip architecture. *APL Mater.* **2**, 032102 (2014)
24. Germs, W. C., Guo, K., Janssen, R. A. J. & Kemerink, M. Unusual thermoelectric behavior indicating hopping to bandlike transition in pentacene. *Phys. Rev. Lett.* **109**, 016601 (2012)
25. Overhof, H. & Beyer, W. A model for the electronic transport in hydrogenated amorphous silicon. *Philos. Mag. B* **43**, 433–450 (1981)
26. DeLongchamp, D. M. *et al.* High carrier mobility polythiophene thin films: structure determination by experiment and theory. *Adv. Mater.* **19**, 833–837 (2007)
27. von Mühlenen, A., Errien, N., Schaer, M., Bussac, M.-N. & Zuppiroli, L. Thermopower measurements on pentacene transistors. *Phys. Rev. B* **75**, 115338 (2007)
28. Aselage, T. L., Emin, D., McCready, S. S. & Duncan, R. V. Large enhancement of boron carbides' Seebeck coefficients through vibrational softening. *Phys. Rev. Lett.* **81**, 2316–2319 (1998)
29. Yan, H. *et al.* A high-mobility electron-transporting polymer for printed transistors. *Nature* **457**, 679–686 (2009)
30. Olivier, Y. *et al.* High-mobility hole and electron transport conjugated polymers: how structure defines function. *Adv. Mater.* **26**, 2119–2136 (2014)
31. Cho, E. *et al.* Three-dimensional packing structure and electronic properties of biaxially oriented poly(2,5-bis(3-alkylthiophene-2-yl)thieno[3,2-*b*]thiophene) films. *J. Am. Chem. Soc.* **134**, 6177–6190 (2012)
32. Schmidtke, J. P., Kim, J.-S., Gierschner, J., Silva, C. & Friend, R. H. Optical spectroscopy of a polyfluorene copolymer at high pressure: intra- and intermolecular interactions. *Phys. Rev. Lett.* **99**, 167401 (2007)
33. Jacobson, M. A., Konstantinov, O. V., Nelson, D. K., Romanovskii, S. O. & Hatzopoulos, Z. Absorption spectra of GaN: film characterization by Urbach spectral tail and the effect of electric field. *J. Cryst. Growth* **230**, 459–461 (2001)

Download references

Author information

These authors contributed equally to this work.
Deepak Venkateshvaran & Mark Nikolka

Affiliations

Optoelectronics Group, Cavendish Laboratory, University of Cambridge, JJ Thomson Avenue, Cambridge CB3 0HE, UK
Deepak Venkateshvaran, Mark Nikolka, Aditya Sadhanala, Mateusz Zelazny, Auke Jisk Kronemeijer, Vincenzo Pecunia, Iyad Nasrallah, Igor Romanov, Katharina Broch & Henning Sirringhaus

Laboratory for Chemistry of Novel Materials, Université de Mons, 20 Place du Parc, 7000 Mons, Belgium
Vincent Lemaur, Yoann Olivier, Jerome Cornil & David Beljonne

Centre for Science at Extreme Conditions, University of Edinburgh, Mayfield Road, Edinburgh EH9 3JZ, UK
Michal Kepa

Department of Chemistry and Centre for Plastic Electronics, Imperial College London, London SW7 2AZ, UK
Michael Hurhangee & Iain McCulloch

Department of Physics and Astronomy, University of New Mexico, 1919 Lomas Boulevard Northeast, Albuquerque, New Mexico 87131, USA

David Emin

Contributions

D.V. designed and fabricated the devices and performed field-effect modulated Seebeck measurements on them. M.N. and A.J.K. optimized the fabrication of IDTBT-based organic FETs and performed transistor measurements. A.S. and M.N. performed photothermal deflection spectroscopy measurements. V.P. optimized the patterning procedure for organic devices. V.L., M.Z., Y.O., J.C. and D.B. performed quantum chemical and molecular dynamic simulations. M.Z. and M.K. acquired the high-pressure induced Raman spectra. K.B. performed measurements on DPPTTT-based devices. I.N. and I.R. performed charge accumulation spectroscopy measurements (Supplementary Information). I.M. and M.H. synthesized IDTBT. D.E. explained the Seebeck measurements on the basis of a narrow-band model. H.S. directed and coordinated the research. D.V., M.N., V.L., Y.O., J.C., D.B., D.E. and H.S. wrote the manuscript.

Competing financial interests

The authors declare no competing financial interests.

Corresponding author

Correspondence to: Henning Sirringhaus

Supplementary information

PDF files

1. Supplementary Information (8.4 MB)
   This file contains Supplementary Text and Data, Supplementary Figures 1-20, Supplementary Tables 1-2 and Supplementary references.

Nature ISSN 0028-0836 EISSN 1476-4687